THÈSE

En vue de l'obtention du

DOCTORAT DE L'UNIVERSITÉ DE TOULOUSE

Délivré par : *l'Université Toulouse 3 Paul Sabatier (UT3 Paul Sabatier)*

Présentée et soutenue le *28/01/2014* **par :**

XI WANG

Décomposition volumique d'images pour l'étude de la microstructure de la neige

---

JURY

SYLVAIN COQUILLAT	Professeur, LA	Président du Jury
JEAN-MARC CHASSERY	Directeur de Recherche, GIPSA-lab	Rapporteur
MICHEL COUPRIE	Professeur, LIGM	Rapporteur
LUC SALVO	Professeur, SIMaP - GPM2	Rapporteur
FRÉDÉRIC FLIN	Chargé de Recherche, CEN	Directeur de Thèse
DAVID COEURJOLLY	Directeur de Recherche, LIRIS	Co-Directeur de Thèse

---

École doctorale et spécialité :
SDU2E : Océan, Atmosphère et Surfaces Continentales

Unité de Recherche :
Laboratoire d'InfoRmatique en Image et Systèmes d'information (UMR 5205)
Centre d'Etudes de la Neige / CNRM - GAME (UMR 3589)

Directeur(s) de Thèse :
Frédéric FLIN et *David COEURJOLLY*

Rapporteurs :
Jean-Marc CHASSERY, *Michel COUPRIE* et *Luc SALVO*

Acknowledgment

During the three years of my PhD, I have realized that even the hardest work can be achieved by discussions, collaborations and support. It is a great pleasure to thank those who have helped me.

First of all, I wish to express my gratitude to my supervisors. Frédéric Flin, was abundantly helpful and offered invaluable assistance, support and guidance. Moreover, his passion of work was, is and will be my long-lasted motivation for work. Our discussions about the research and the life will not be forgotten. To me, it was also very fortunate to have another supervisor, David Coeurjolly. His experience on the thesis subject and on the guidance of PhD students was a treasure to me. He guided me tightly through three years: from the analysis, the conception, the implementation, the experimentation up to the final stage.

I wish to thank Jean-Marc Chassery, Michel Couprie and Luc Salvo for their interest in my research work and for their willingness to be the reviewers of this thesis. I also want to thank Sylvain Coquillat who have agreed to participate in the jury board. I really appreciated their questions and remarks.

I would like to thank all the members of CEN who are so kind to me as a familly. A deeply thank to Anne Dufour and Bernard Lesaffre, the colleagues of group "Manteau Neigeux", who have helped me for correcting this thesis and have always given their confidence to me. Of course, I will not forget Neige Calonne and Carlo Carmagnola, who shared the same office with me in CEN and supported and advised me not only for the research works but also for the daily life in Grenoble during one and a half years. Their encouragements are an important part of the success of this thesis.

I also thank the members of LIRIS for both friendly and scientific discussions. In particular, a lot of thanks to my friends, Rada Deeb, Ricardo Uribe Lobello, Florent Wachtel, SangHyun SEO and so on for sharing the happiness and sadness of my life.

I owe my deepest gratitude to my parents, my family for their endless love, sup-

port, trust, and presence and to my little girl Chloé, who was very nice to me throughout the editing of this thesis.

Last but not least, I want to thank specially my husband Dong Chen for his support and love. It's so fortune to be loved by such kind and warmhearted man.

Thank you all!

Xi Wang

Abstract

Snow avalanches are complex natural phenomena whose occurrence is mainly due to the structure and properties of the snowpack. To better understand the evolution of these properties over time, it is important to characterize the microstructure of snow, especially in terms of grains and ice necks that connect them. In this context, the objective of this thesis is the decomposition of snow samples into individual grains from 3-D images of snow obtained by X-ray microtomography. We present two decomposition methods using algorithms of discrete geometry. Based on the results of these segmentations, some parameters such as the specific surface area and the specific contact area between grains are then estimated from samples of several snow types. These segmentation methods offer new outlooks for the characterization of the microstructure of snow, its properties, and its time evolution.

Keywords: Snow, Metamorphism, Microstructure, Shape decomposition, Digital geometry

Résumé

Les avalanches de neige sont des phénomènes naturels complexes dont l'occurrence s'explique principalement par la structure et les propriétés du manteau neigeux. Afin de mieux comprendre les évolutions de ces propriétés au cours du temps, il est important de pouvoir caractériser la microstructure de la neige, notamment en termes de grains et de ponts de glace les reliant. Dans ce contexte, l'objectif de cette thèse est la décomposition d'échantillons de neige en grains individuels à partir d'images 3-D de neige obtenues par microtomographie X. Nous présentons ici deux méthodes de décomposition utilisant des algorithmes de géométrie discrète. Sur la base des résultats de ces segmentations, certains paramètres, comme la surface spécifique et la surface spécifique de contact entre grains sont ensuite estimés sur des échantillons de neiges variées. Ces méthodes de segmentation ouvrent de nouvelles perspectives pour la caractérisation de la microstructure de la neige, de ses propriétés, ainsi que de leur évolution au cours du temps.

Mots-clefs:
Neige, Métamorphose, Microstructure, Décomposition de formes, Géométrie discrète

Contents

List of Figures

List of Tables

Introduction

Contexte général

La neige, qui est constituée d'air et d'eau sous ses différentes phases (glace, vapeur et parfois eau liquide), est un matériau poreux complexe. Depuis sa chute au sol jusqu'à sa fonte complète, elle ne cesse de se transformer sous l'effet des contraintes thermodynamiques (températures, humidité) et mécaniques imposées par son environnement (Fig. 1.1). Ce processus de transformation, appelé *métamorphose* affecte directement les propriétés de la neige à l'échelle macroscopique et c'est d'ailleurs pour cette raison que les métamorphoses du manteau neigeux sont une des principales causes d'avalanches (Fig. 1.2). En fait, les propriétés physiques et mécaniques d'un certain type de neige sont entièrement déterminées par sa microstructure. Il est donc nécessaire d'étudier l'évolution de la microstructure de la neige au cours des métamorphoses afin de mieux comprendre et modéliser le comportement macroscopique du manteau neigeux.

Pour analyser la microstructure de la neige de manière quantitative, le CEN a recours depuis une quinzaine d'année à la tomographie par rayons X, technique adaptée à l'étude des matériaux et permettant d'obtenir des images tridimensionnelles (3-D) à haute résolution (1 pixel = 5 à 10 microns) de petits volumes de neige (environ 1 cm^3). Une fois les images obtenues, il est ensuite nécessaire, à l'aide d'algorithmes adaptés, d'en extraire les paramètres géométriques et physiques pertinents. L'obtention d'images 3-D de la microstructure de la neige permet ainsi de proposer, puis de valider des modèles physiques capables de simuler le comportement de la neige et ses métamorphoses à micro-échelle, en fonction des conditions appliquées (température et humidité, notamment) [KP09, BGN12].

Dans ce contexte, la recherche sur la microstructure de la neige au CEN se décompose en deux parties principales :

— Une partie expérimentale, qui vise l'acquisition d'images 3-D de la microstructure de la neige par tomographie par rayons X pour l'initialisation et la validation de modèles.

— Une partie théorique et numérique, qui consiste à étudier les mécanismes physiques impliqués dans les métamorphoses. L'objectif est de préciser les équations nécessaires pour bien décrire les processus impliqués et qui seront mis en œu-

vre dans des modèles numériques 3-D.

La croissance et la décroissance de cristaux de glace dans l'air est un phénomène important qu'il est nécessaire de simuler finement dans les modèles. Néanmoins, en raison de sa complexité, il est encore mal compris, et certaines de ces variables (vitesse de croissance en fonction de la température et de l'orientation cristalline, notamment) restent difficiles à modéliser. En outre, il y a, au cours des métamorphoses, un fort couplage entre effets purement thermodynamiques et effets mécaniques (par exemple, réarrangement des grains de glace sous l'effet de la gravité, ou du poids des couches supérieures du manteau neigeux -voir Fig. 1.3). Pour résoudre ces problèmes, des outils d'analyse d'image sont indispensables. Un besoin particulièrement important consiste en la décomposition de la structure de la glace en grains individuels (voir Fig. 1.4) compatibles avec les besoins de la modélisation physique et/ou mécanique de la neige.

Dans ce travail de thèse, nous avons donc cherché à développer des algorithmes capables de segmenter des microstructures de neige en différents grains et d'étiqueter chaque grain à l'aide d'une couleur unique (voir Fig. 1.5). Pour cela, nous avons fait appel à des outils de géométrie discrète, domaine qui peut se définir comme un ensemble de théorèmes et outils algorithmiques traitant des propriétés géométriques et topologiques d'images numériques et qui vise à modéliser et analyser des objets continus, ou les phénomènes associés, à l'aide d'un nombre fini de données discrètes.

Organisation du manuscrit

Après la présentation des objectifs de notre thèse, nous introduisons, dans le chapitre 2, les principales notions nécessaires à la compréhension du travail réalisé. Nous commençons par les propriétés physiques et mécaniques de la neige, puis nous nous focalisons sur sa microstructure. Nous présentons notamment les différentes définitions possibles du grain de neige ainsi que les techniques expérimentales permettant d'obtenir des images de la microstructure de la neige. Nous introduisons ensuite des définitions de base de géométrie algorithmique ainsi que d'analyse géométrique adaptées à l'étude des images 3-D de neige.

Dans le chapitre 3, nous présentons une méthode de segmentation (CDGS) pilotée

par la courbure de l'interface air-glace. Nous évaluons ensuite la qualité des segmentations obtenues en les comparant, par exemple, à des mesures physiques (Diffraction Contrast Tomography, DCT), puis discutons de ses limites.

Dans le chapitre 4, nous proposons un autre algorithme de décomposition en grains (MADF), qui répond à certains des désavantages de CDGS, puis le comparons aux méthodes physiques et algorithmes existants (DCT, méthode de watershed classique et CDGS).

Le chapitre 5 traite des applications de ces méthodes de segmentation à de nombreuses microstructures de neige, et s'intéresse à l'estimation de paramètres quantitatifs décrivant la structure des ponts entre les grains (estimation de la surface spécifique de contact entre les grains, SGCA). Cette partie applicative permet en outre une validation des méthodes sur une grande diversité d'échantillons.

Enfin, nous concluons et présentons les perspectives de ce travail de thèse dans le chapitre 6.

Chapter 1

Introduction

Contents

1.1 General context

Snow, which is made of air and water (ice, vapor and sometimes liquid water), is a complex porous material. From its fall on the ground to its complete melting, snow transforms continuously under the effect of temperature, moisture, thermal and mechanical stresses. This process, called *metamorphism* (Fig. 1.1) affects directly the snow properties at macroscale. For this reason, the main causes of avalanches (see Fig. 1.2) are often related to metamorphic changes in the snowpack. Actually, the physical, mechanical and thermal behavior of a certain type of snow is entirely determined by its internal microstructure. It is therefore necessary to study the evolution of the microstructure during metamorphism to better understand and model the behavior of the snowpack.

In order to analyze the snow microstructure quantitatively, the CEN has used X-ray tomography. This technique, which is well-suited to the study of materials, provides high resolution three-dimensional (3-D) images (1 pixel = 5 to 10 microns) of small snow volumes (about 1 cm^3). Once the images have been obtained, it is then necessary to extract the relevant geometrical and physical parameters using specific algorithms. Among several advantages, 3-D images of snow microstructure make it possible to propose and then validate physical models to simulate the behavior of snow and its metamorphism at micro-scale, depending on the applied conditions (temperature, humidity, etc.) [KP09, BGN12].

In this context, research on the microstructure of snow at CEN is divided in two main parts:

— An experimental part, which aims at acquiring 3-D images of snow microstructure by X-ray tomography for initialization and validation of the models.

— A numerical and theoretical part, which consists in studying the physical mechanisms involved in snow metamorphism. The goal is to specify the physical equations necessary to well describe the involved processes and to implement them in 3D numerical models.

The growth and decay of ice crystals in air is an important phenomenon which needs to be finely simulated in the models. Nevertheless, because of its complexity, it is still poorly understood, and some of its variables (growth rate as a function of

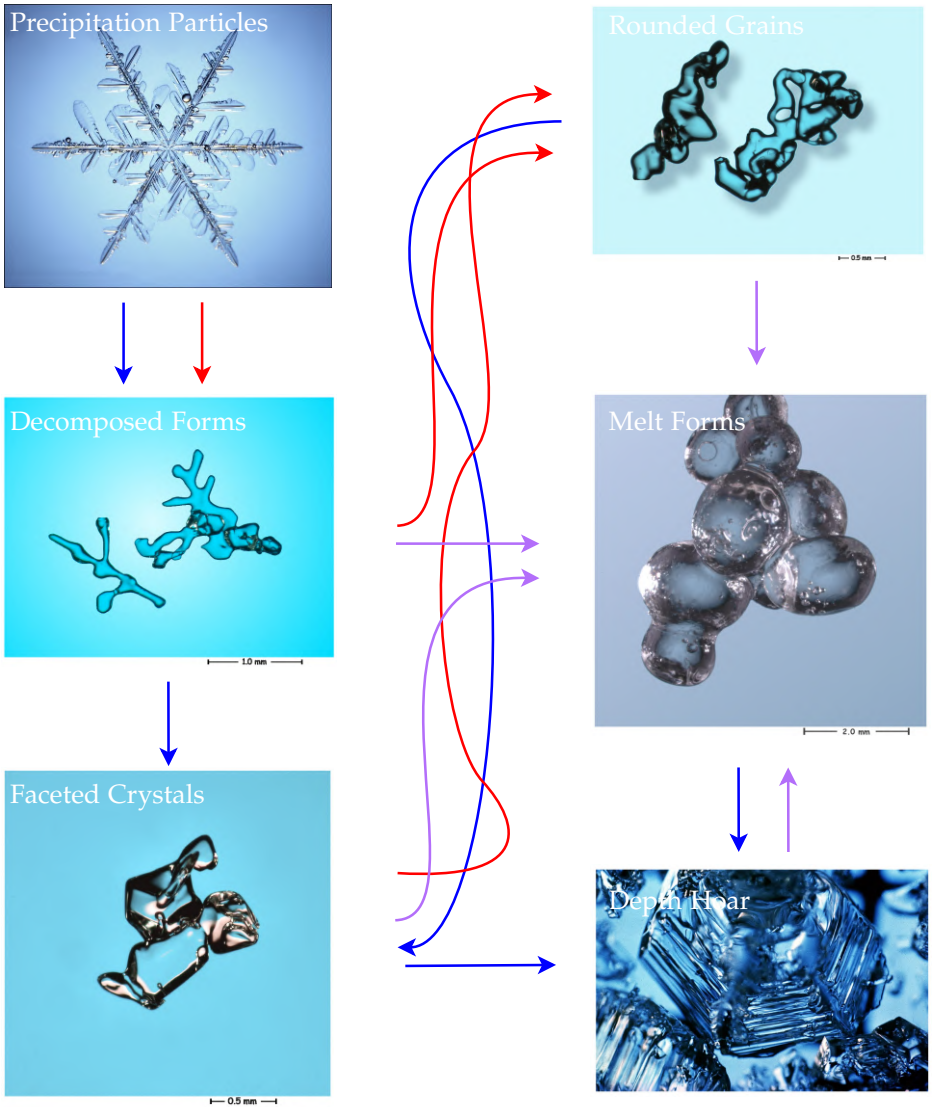

Figure 1.1 – Various types of snow metamorphism.

Figure 1.2 – A powder snow avalanche.

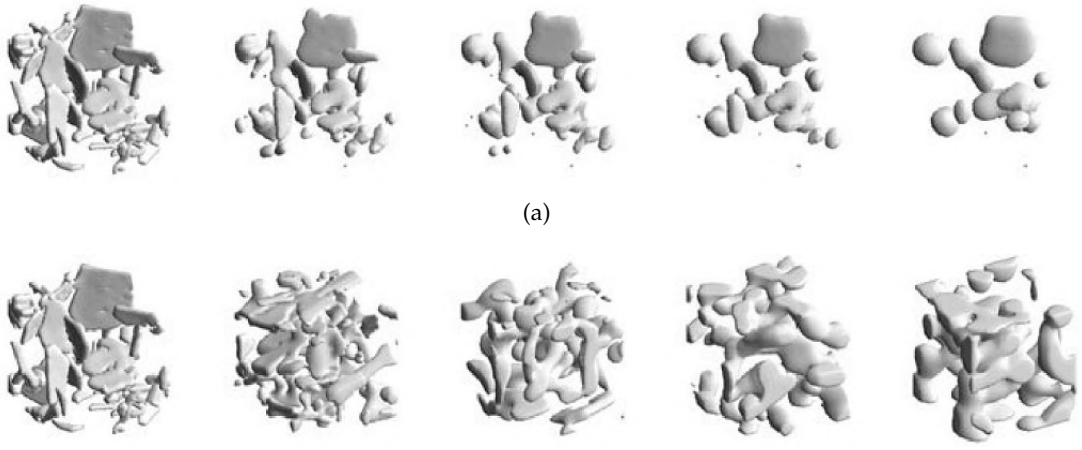

(a)

(b)

Figure 1.3 – Metamorphism on real data: time evolution of the microstructure obtained by applying a 3-D model that does not take mechanical effects into account (a); and from the experimental samples at the same resolution (b). [FBL+03]

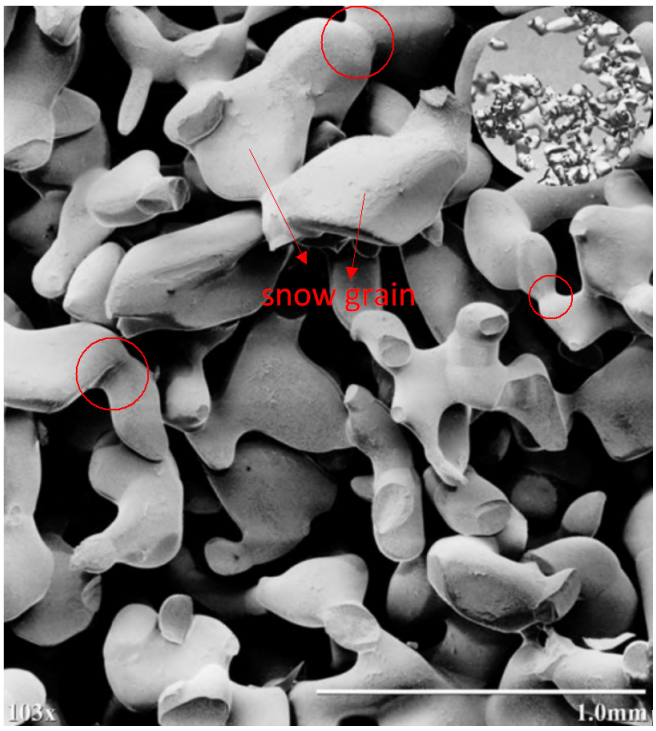

Figure 1.4 – Snow sample at the microscale. The red circles show the interface between two grains of snow.

temperature, crystalline orientation, etc.) remain difficult to model. Moreover, metamorphism is generally made of a strong coupling between purely thermodynamic effects and mechanical effects (e.g. rearrangement of grains of ice under the effect of gravity or the weight of the upper layers of the snowpack - see Fig. 1.3). To solve these problems, image analysis tools are mandatory. A really important need is the decomposition of the ice structure into individual grains whose definition is compatible with the physical and/or mechanical modeling requirements of snow (see Fig. 1.4).

In this thesis work, we developped algorithms to segment snow microstructures into different grains and to label each grain using a single color (see Fig. 1.5). For that purpose, we used concepts of *digital geometry*. This discipline, which can be simply characterised as a set of definitions, theorems and algorithmic tools dealing with the geometric and topological properties of subsets of digital pictures, aims at modeling and analysing continuous objects or phenomena with the help of a finite number of discrete data.

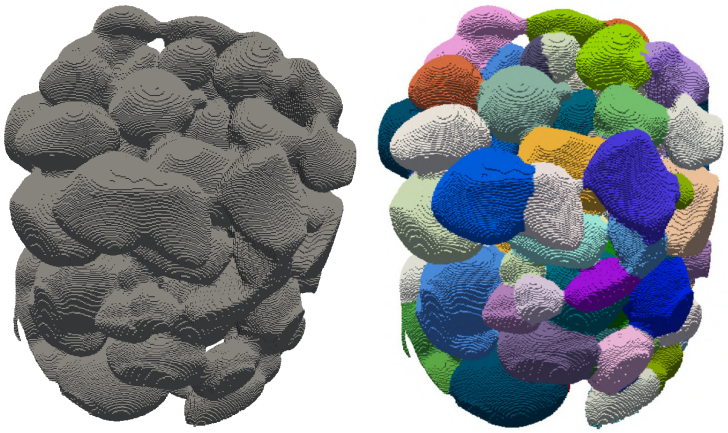

(a) (b)

Figure 1.5 – Snow grain decomposition: (a) an original snow image, (b) grain decomposition using the MADF algorithm (see Chapter 4).

1.2 Organization of the manuscript

After the presentation of the objectives of the thesis, we introduce, in Chapter 2, the basic concepts that were used to address the work. We begin with the physical and mechanical properties of snow and focus then on its microstructure. In particular, we present the different possible definitions of a snow grain, as well as the experimental techniques used to obtain images of snow microstructure. We then introduce some basic definitions of algorithmic geometry and of geometric analysis adapted to the study of 3-D snow images.

In Chapter 3, we present a segmentation method (CDGS) based on the curvature of the ice-pore interface. We then evaluate the quality of the resulting segmentations by comparison to physical measurements (Diffraction Contrast Tomography, DCT), and discuss its limitations.

In Chapter 4, we propose another algorithm for grain decomposition (MADF), which addresses some of the disadvantages of CDGS. We then compare it to existing physical methods and numerical algorithms (DCT, standard watershed method and CDGS).

Chapter 5 deals with the application of these segmentation methods to many snow

microstructures. It focuses on the estimation of quantitative parameters describing the structure of necks between grains (estimation of specific grain contact area, SGCA). It also deals with the evaluation of the methods on a large set of various snow samples.

Finally, we conclude and present the perspectives of this thesis in Chapter 6.

Chapter 2

Imaging of snow microstructure and introduction to digital geometry

Contents

2.1 Snow and snow microstructure

Snow is a porous material which is constituted of air, water vapor, ice and sometimes liquid water. The microstructure of snow is complex since the size, the shape, and the number of stuctural elements vary widely in natural snowpacks. This complex microstructure of material evolves continuously with time, which is called snow metamorphism (Fig. 1.1). Although the general effects of various types of metamorphism are roughly well-known, the physical mechanisms that lead to these transformations are not perfectly well understood. Since the snow microstructure directly influences several properties of snow at the macroscale, modelling the behaviour of snow microstructure is necessary for avalanche-risk forecasting, mainly as a means to provide parameterizations of grain-scale physics into existing or future models at the field scale.

Currently, no standard method or parameter exists to characterize snow microstructure. Many of the quantities discussed are volumetric averages and therefore cannot represent the complex geometric configuration of the air and ice matrix. Recently, more and more material scientists start to analyse and characterize microstructures in 3D materials using mathematical geometry [OM00].

2.1.1 Physical and mechanical properties of snow

2.1.1.1 Some physical properties of snow

Temperature (T_s) : Because snow contains air (almost 90% of its weight in the case of fresh snow), it is a good insulator, i.e. a poor conductor of heat. Even at the external temperature of $-15°C$ or $-20°C$, the temperature near the soil layer remains around $0°C$, whereas on the snow surface (the boundary layer with the atmosphere), the temperature can vary widely (generally, from $-10°C$ to $0°C$).

Density (ρ_s) : This quantity, expressed in mass per unit volume (kg/m^3) is usually determined by weighing snow of a known volume. Since snow is a mixture of ice crystals and air, it can have a range of different densities, depending on how compacted the snow is. Table. 2.1 gives a few characteristic densities, along with that of water and solid ice for comparison.

Table 2.1 – Characteristic densities of various snow types

Snow types	**Density** $[kg/m^3]$
Precipitation Particles	10 - 150
Decomposed Forms	80 - 200
Faceted Crystals	200 - 350
Rounded Grains	200 - 500
Melt Forms	200 - 600
Depth Hoar	200 - 450
Ice	800 - 900
Water	1000

Porosity (ϕ) : is a fundamental parameter of any porous medium. It is defined as the volume of the pore space divided by the total volume. The porosity ϕ of a snowpack is easily calculated from the snow density:

$$\phi = \frac{\rho_{ice} - \rho_{snow}}{\rho_{ice}} \tag{2.1}$$

where ρ_{ice} is the density of ice induding snow and pore space. ρ_{snow} is the density of snow.

Liquid water content (θ_w) : is a parameter to estimate the amount of water in liquid phase within the snow. Liquid water in snow originates from either melt, rain, or a combination of both. Measurements of this parameter are expressed as either a volume ($\theta_{w,V}$) or mass ($\theta_{w,m}$) fraction. Both can be presented as a percentage (%). Table. 2.2 gives an overview of the characteristic values of moisture contents depending on the snow types.

Table 2.2 – Snow liquid water contents and their associated characteristics

Type	**Average water content** %	Characteristics
dry	0	
moist	<3	tend to hold together, cohesive
wet	3 - 8	10× expansion - water in pores visible
very wet	8 - 15	water content increases, air content decreases
slush	>15	snow is flushed with water, very small air content

2.1.1.2 Snow mechanics

Snow mechanics strictly deals with the kinematics, dynamics and energetics of snow in all of its various forms. Kinematics is a branch of classical mechanics that describes the motion of objects (or materials in this case) without considering the circumstances leading to that motion, whereas dynamics makes up the other branch which studies the relationship between the motion of objects and the causes thereof. Energetics deals with energy flows and storages under transformation.

In terms of rheology (i.e. the study of the flow/deformation behaviour of a substance), standardized rheological models are generally used to describe the mechanical behaviour of snow. These models consist of various combinations, either in series, in parallel, or both of spring and dashpot systems. They are more useful as a qualitative description of the deformation of snow, but they have limited qualitative value since the elasticity and viscosity of snow are strongly nonlinear with respect to temperature and density.

The single most troublesome property of snow is probably its high compressibility, which causes it to behave very differently from most solids and granular materials [MRU74]. For example, for bulk stresses below a certain critical value, snow can be treated as a low compressibility solid, but once this critical value is exceeded, the snow density increases irreversibly, causing it to have greatly different mechanical properties [AG75]. Snow Young Modulus, which is a mathematical description of its tendency to deform elastically (i.e. non-permanently) when a force is applied to it, varies by at least three orders of magnitude within the range of densities that snow commonly has [SRUotCoE97]. Another complicating factor is that it is not enough to characterize the mechanical behaviour of snow only in terms of its original physical state (density, temperature, etc.) and that of the stress applied to it; it is also necessary to account for the stress or strain history. In theory, such contingency applies to nearly all materials, and formal procedures have been developed in rational mechanics to account for stress or strain histories. These are in practice very difficult, but in the case of snow are made even worse by the time-dependent structural changes (snow metamorphism) that occurs independently of stress, like sintering or grain growth.

Finally, another great challenge in snow mechanics is illustrated by the fact that

all of the great complexities of the rheology of snow, a very limited few aspects of which have been briefly mentioned above, and which have more comprehensively been summarized by [MRU74], have come largely out of the investigation in laboratory testing or in situ observation of dry, coherent snow; whereas no data exist for fluidized snow (snow whose intergranular bond structure is destroyed, thereby losing its ability to resist shear). Mechanics is the branch of physics concerned with the behaviour of physical bodies when subjected to forces or displacements, and the subsequent effect of the bodies on their environment.

Stress : is a measure of the average amount of force exerted per unit area. Where:

$$\sigma = \frac{F}{A} \tag{2.2}$$

σ is the average stress, also called engineering or nominal stress, and F is the force acting over the area A.

Strain : is the geometrical measure of deformation representing the relative displacement between particles in the material body, i.e. a measure of how much a given displacement differs locally from a rigid-body displacement.

Young modulus (E) : describes tensile elasticity, or the tendency of an object to deform along an axis when opposing forces are applied along that axis; it is defined as the ratio of tensile stress to tensile strain.

Viscosity : is a measure of the resistance of a fluid which is being deformed by either shear stress or extention stress. In general terms it is the resistance of a liquid to flow, or its "thickness". Viscosity describes a fluid's internal resistance to flow and may be thought of as a measure of fluid friction.

Snow Young modulus varies greatly over the range of densities commonly found for snow. In general, it increases with increasing density. However, due to the complexities of snow as a substance, the relationship is not uniform, but rather linear for the lower range of densities, with the linearity breaking down at the higher density ranges. Also, the linearity of such functions depend on a host of snow conditions, and also on different testing methods.

In simple terms, this wide ranging Young's modulus means that for stresses below

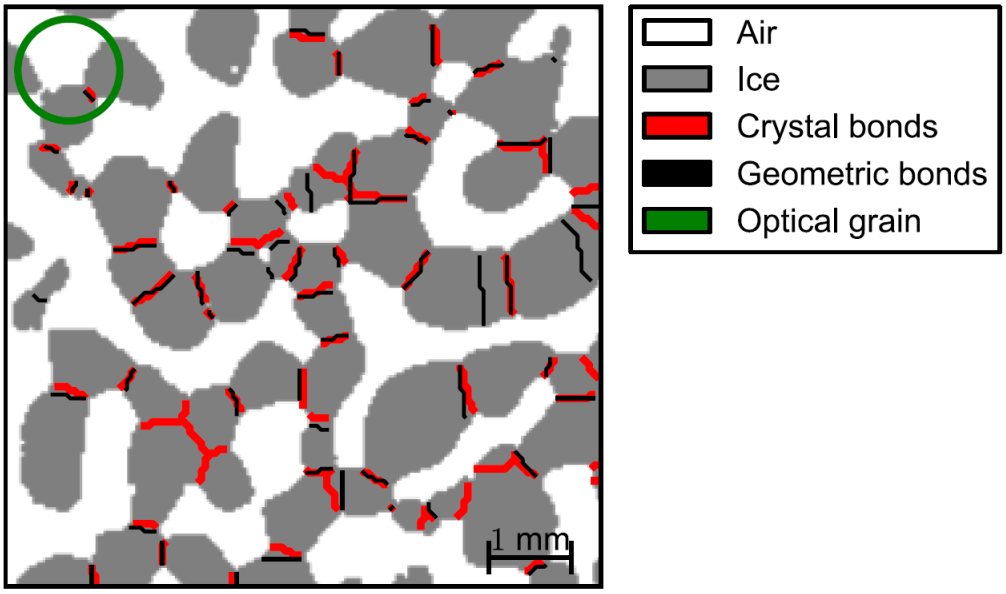

Figure 2.1 – Segmentation with different definitions of snow grain (constructed by Pascal Hagenmuller in technical report "Grain segmentation of snow microtomographic data", 17 May, 2013).

a certain critical value, a snow pack can be modeled as behaving like certain low-compressable solids, but as soon as this critical stress value is exceeded, snow deforms non-elastically and an entirely different modelling approach is necessary.

2.1.2 Snow grains at microscale

The studies of snow microstructure are necessary since the physical and mechanical properties of snow are strongly depending on its microstructure. Further modeling and computing of snow mechanical simulations requires a precise 3-D description of snow microstructures in terms of individual grains and bond's characteristics.

Currently, no standard definition of snow grain exists. In most cases, the concept of snow grain is related to the properties of interest and can be defined as the smallest elementary particle which is consistent with snow physics and mechanics at micro-scale. Therefore, several definitions of snow grain can be found in the literature, associated to the crystalline, optical and mechanical properties, respectively. These different concepts of snow grains are illustrated in Fig. 2.1.

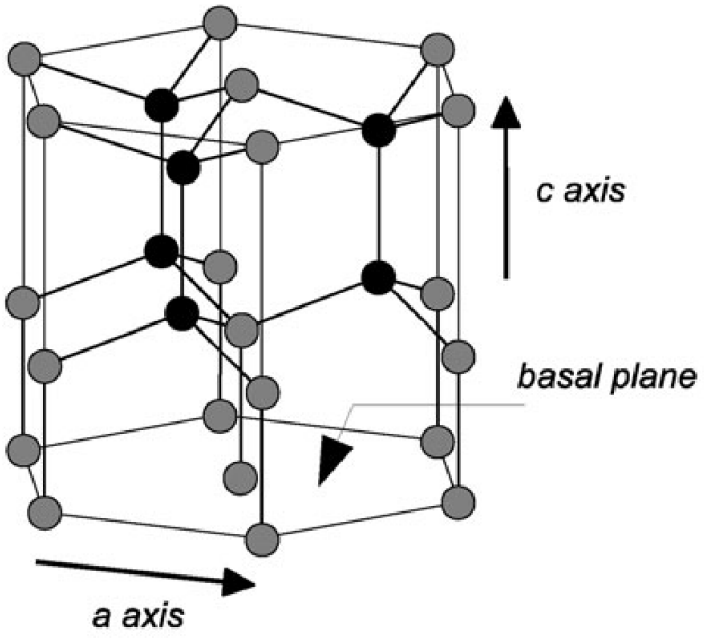

Figure 2.2 – Crystallographic structure of hexagonal ice and viscoplastic anisotropy of the ice crystal [RKP+11].

2.1.2.1 Crystalline grains

Small rounded grains (RG) are typically monocrystalline [RBRS+12]: it means that the snow particles are equivalent to single ice crystals (see Fig. 2.2), i.e., connected ice zones of almost constant c-axis orientation. Generally, if no aggregation phenomena occurs, a snowflake is also made of a single crystal [Nelo1]. The crystalline orientation is especially important for plastic deformation of snow or kinetic growth processes. The c-axis orientation can be measured in 2-D with the Automatic Ice Texture Analyzer [WRHS03] or in 3-D with diffraction contrast tomography (DCT) [LRK+09]. Crystal boundaries can also be identified with serial sectioning of cast snow samples because grain boundaries tend to sublimate faster than the rest of the ice matrix [AGBD98].

2.1.2.2 Optical grains

In order to model the electromagnetic properties of snow (e.g. albedo), "equivalent spheres" with same volume-to-surface ratio are commonly used in snow microstruc-

ture. In [War82], a grain is a sphere of radius $r_{opt} = 3V/S$ where V is the volume of ice and S is the surface area of ice. The optical grains can be determined indirectly through optical measurements [GDZP09, APC+11] or directly by calculating the specific surface area from X-ray micro-tomography pictures [FBL+04].

2.1.2.3 Mechanical grains

The most popular definition of a snow grain is that of an an individual particle that can be easily detached from the snow sample. It corresponds to a mechanical definition of a snow grain because the ice structure is disaggregated via a mechanical load. Mechanical grains are sometimes called "classical" grains [FAD+09]. The geometrical characteristics of the individual grains can be estimated manually with a plate that has a millimeter grid or via automatic analysis of macro-photo images [LPM98]. However, these analysis intrinsically miss the information around grain bonds that are interconnected. The bond characteristics of grains are considered as important for studying the microstructure of snow. [Kry75] first tried to detect manually bonds between grains from the ice surface in snow. Then, the method of 2D sections was improved to detect bonds automatically [EB95]. The microstructural variables derived from such a grain segmentation have been used to develop and fit snow metamorphism models, which are still in use today to forecast avalanches [BFSS01].

2.2 Experimental techniques for snow microstructure imaging

Physical and mechanical properties of snow are essentially determined by its microstructure, which continuously evolves with time. Several means can be used to observe snow at microscale. Main techniques to obtain 3-D numerical images of snow microstructure are introduced below.

2.2.1 Principle of X-ray absorption microtomography

The direct observation of snow at the microscale is difficult. Tomography is an imaging technique which refers to the description of a section of material within a 3-D solid material and allows viewing, nondestructively, the structure of this mate-

rial. For this, different types of physical excitation can be used (ultrasonic, electric or magnetic field (NMR), X-ray and γ-ray...), with different acquisition modes (transmission through a material). The method of transmission electron microscopy, which has been used so successfully to examine dislocations in other crystalline materials, has led to little success with ice. It is difficult to prepare the suitable thin samples for examination. Moreover, once prepared, they sublime quickly within the vacuum of the microscope. Another method, etch pitting, which has usually been used for other materials has been also applied on ice. However, the problem of this method is that it suffers from a questionable relationship between surface pits and bulk dislocations [JG73, Bako3]. The technique is also sensitive to surface preparation [Sin78, LBD95].

In this study, we use X-ray absorption tomography: when a sample is exposed to a beam of photons, one part of incident photons is absorbed by the sample, and the other part is transmitted to the detector, which is opposite to the X-ray source. The ratio of the incoming intensity on the transmitted intensity depends on the integral, along the X-ray beam, of absorption coefficients of the crossed phases (in our case, air, ice or 1-chloronaphtalene). Thus, from measurements of transmitted intensity, the reconstruction of the spatial distribution of the phases of the object can be performed. For a more comprehensive approach, one may consult [PGM96]. Note that obtaining tomographic images is characterized by handling large numbers of data and requires powerful computer resources in terms of memory and computing time. This largely explains the relatively recent (late 1990's) development of this technique for snow.

In practice, the source emitting X-rays, the sample, and the detector measuring the transmitted X-rays, are aligned. A measurement of the transmitted intensity, visualized in greyscale, is called a radiography (see Fig. 2.8 - (a)). During one tomographic acquisition, the sample rotates for obtaining a set of radiographies. Reconstruction algorithms then help, by combining all radiographies, to determine the surface distribution of the absorption coefficient and provide horizontal cross-section of the analyzed sample that represent this distribution in grayscale (see Fig. 2.8 - (b)). The various phases composing the object are identifiable, if their absorption coefficients are sufficiently distinct. A 3D image can then be built from a stack of 2D images.

2.2.1.1 Interaction of X-rays and material

The X-radiation is a high-energy electromagnetic wave which extends fractions of a few keV to MeV that can traverse most of materials.

When passing through a given material, the X-ray beam undergoes both an attenuation and phase shift with respect to its propagation in vacuum. The dependent attenuations and phase shifts undergone by the complex refractive index of n material:

$$n = 1 - \delta + i\beta \tag{2.3}$$

where the β determines the attenuation of the wave and the δ, the phase shift suffered by the wave. Consider a plane monochromatic wave of λ emitted wavelength in the x direction, and passing through a heterogeneous material whose refractive index is $n(x, y)$. Transmission function T gives, at point (x_1, y_1), the form of the transmitted wave:

$$T(x_1, y_1) = A(x_1, y_1) \exp[i\phi(x_1, y_1)] \tag{2.4}$$

where $A(x_1, y_1)$ is the amplitude of the transmission function, the ratio between the amplitude of the transmitted wave and that of the incident wave,

$$A(x_1, y_1) = \exp[-\frac{2\pi}{\lambda} \int_{x_0}^{x_1} \beta(x_1, y_1)\, dx] \tag{2.5}$$

and $\phi(x_1, y_1)$ is phase modulation:

$$\phi(x_1, y_1) = \phi_0 - \frac{2\pi}{\lambda} \int_{x_0}^{x_1} \delta(x_1, y_1)\, dx \tag{2.6}$$

ϕ_0, represents the phase modulation being caused to the wavelength in the absence of the object.

If the wave attenuation is measured, we refer to absorption tomography. If, we are interested in its phase, it is called phase tomography. Later, we will focus on the absorption tomography, by far the most classic and the most used. For a first approach of phase tomography, we can see for example the thesis of Coindreau.

2.2.1.2 Absorption Tomography

Tomography absorption consists in measuring the attenuation of X-rays passing through a given sample. It is based on the use of the Beer-Lambert or attenuation law.

Beer-Lambert Law When a sample is subjected to a photon beam, part of the incident photons is absorbed by the sample, and the other comes to the detector. The transmittance T_r, equal to the ratio between the number of photons N transmitted and the number N_0 of incident photons is equal to the square of the amplitudes, which gives, with the notation of equation 2.7:

$$T_r = \frac{N}{N_0} = \left(\frac{A(x_1, y_1)}{A(x_0, y_1)}\right)^2 = \exp\left[-\frac{4\pi}{\lambda}\int_{x_0}^{x_1} \beta(x, y_1)\, dx\right] \tag{2.7}$$

The absorbance, denoted A_r, is given by the following formula:

$$A_r = -\ln T_r = \frac{4\pi}{\lambda}\int_{x_0}^{x_1} \beta(x, y_1)\, dx \tag{2.8}$$

This law, which connects the absorbance path length and properties of the material covered is called the Beer-Lambert and can be written as:

$$A_r = \int_{x_0}^{x_1} \mu(x, y_1)\, dx \tag{2.9}$$

where μ, the linear attenuation coefficient is a material property. It is expressed in (m^{-1}) and is:

$$\mu = \frac{4\pi}{\lambda}\beta \tag{2.10}$$

Linear attenuation coefficient : Four main physical phenomena are at the origin of the X-ray attenuation in the material [AR68, Bla97]:

— **The photoelectric effect:** an incident photon is absorbed by an atom. This atom excited then emits an electron.

— **Thomson or elastic scattering reaction:** an incident photon is deflected after a collision with elastic electron.

— **Inelastic scattering or Compton effect:** an incident photon is deflected after inelastic collision with an electron. Then changes the photon energy.

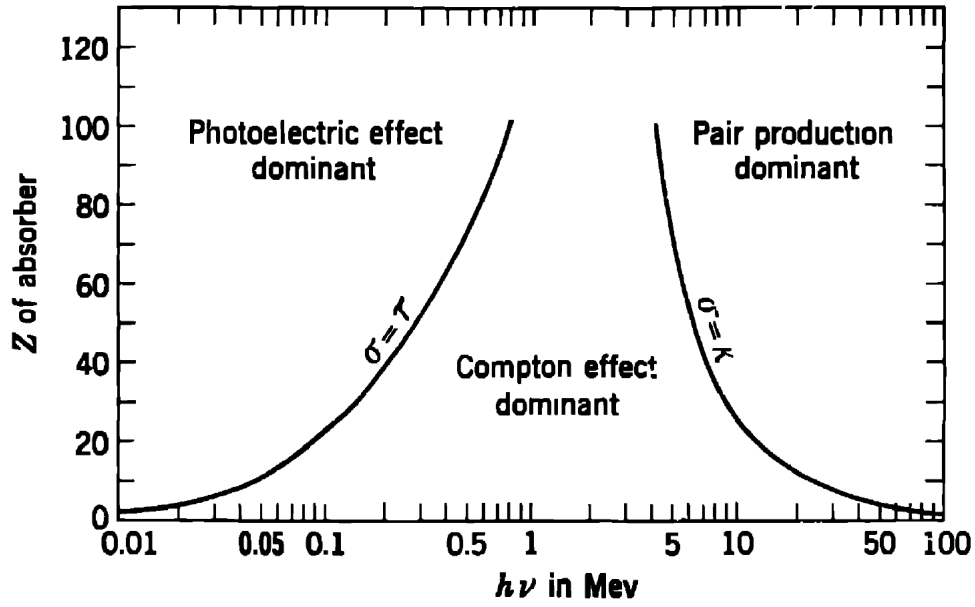

Figure 2.3 – Relative importance of the major interactions between 10 keV and 100 MeV. The lines show the values of Z and $h\nu$ for which the two neighboring effects are just equal [Eva55].

— **Creating pairs:** when the incident photon has an energy greater than about 1 MeV, it may, under the effect of the electrostatic field of an atomic nucleus, convert into a electron-positron pair. Other productions of pairs are possible at higher energies.

The intensity of these effects depends on the atomic number Z of the material and the energy E of the radiation (see Fig. 2.3).

For the energy less than a few tens of keV (in the case of energy used for imaging of snow), the photoelectric effect is predominant and μ depends on both the density ρ of the material, Z and E [AR68]:

$$\mu = K\rho\frac{Z^4}{E^3} \tag{2.11}$$

where K is a constant. Note that at a given energy, μ is proportional to the both ρ and Z^4. This feature of the photoelectric effect makes problematic quantitative measurements of the chemical composition of materials: a change in Z can

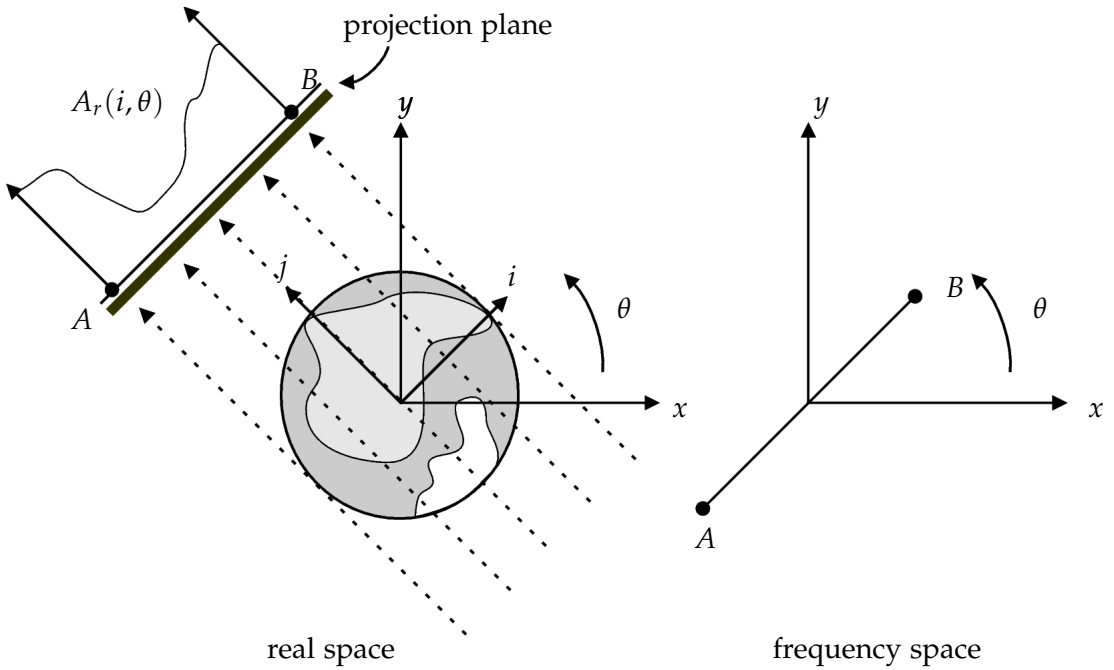

Figure 2.4 – The principle of tomographic acquisition and the theory of cut projection (by Fédéric Flin in [Flio4]).

mask a change in ρ, and vice versa. This ambiguity on Z and μ can be lifted by making images with two different energies.

Principle of data acquisition : The principle of tomographic acquisition comprises rotating the sample itself and to measure each angle of incidence θ of the beam, the absorbance $A_r(i,\theta)$ (Fig. 2.4).

Once the acquisition is completed, it therefore has a series of integrals of the form:

$$A_r(i,\theta) = \int_{j_0}^{j_1} \mu(i,j)\, dx \tag{2.12}$$

where (i,j) are the coordinates in the rotating frame $(\vec{i},\vec{j})$, j_0 and j_1 respective abscissas of the points of input and output of the beam in the sample.

Principle of reconstruction : Tomographic reconstruction is a process which, from the integrals $A_r(i,\theta)$ reconstructs the spatial distribution of the absorption coefficient μ in the whole sample. There are two main types of methods [BBM+oo, KSo1]:

— **The analytical methods**, for which we seek an expression of μ by reversing the equation 2.12 by Fourier transforms. This expression is then discretized to fit the data sampling (Discrete Fourier Transform). They are based on the theorem backprojection [KS01]:

Definition 2.1 (Fourier Transform)**.** *1-D Fourier transform of a parallel projection $A_r(i,\theta)$ following $\vec{j}$ on the direction $\vec{i}$, denoted by $\widehat{A_r}(I,\theta)$, is equal to the cutting, in the same direction $\vec{i}$ of the 2-D Fourier transform $\hat{\mu}(X,Y)$ of original function $\mu(x,y)$:*

$$\hat{\mu}(I\cos\theta, I\sin\theta) = \widehat{A_r}(I,\theta) \tag{2.13}$$

By calculating the 1-D Fourier transforms of projections $A_r(i,\theta)$ for different values θ, it is possible to obtain the profiles of $\hat{\mu}$ in different lines of the Plan $(\vec{X},\vec{Y})$ (see Fig. 2.4). $\mu(x,y)$ is then accessed by inverse Fourier transform. In practice, we generally utilise a filtered backprojection method, which firstly consists of filtering the projections $A_r(i,\theta)$ in the frequency domain and determine $\mu(x,y)$ at any point in the plane by averaging the filtered projections obtained on all orientations.

Methods based on this principle are widely used because of their rapidity, but require a complete set of evenly spaced data: acquisition of projections at an angle of 180°, check the Nyquist criterion for data sampling.

— **Algebric methods**, which consist in discretizing the section dealing with N pixels and then reconstruct the image by resolution of the following linear system:

$$\vec{u} = \mathbf{M}\cdot\vec{v} \tag{2.14}$$

where $\vec{u}$ is the vector containing $A_r(i,\theta)$, a vector $\vec{v}$ represents the N pixels of the section, and $\mathbf{M}$ is the projection matrix.

These methods are numerically longer than the analytical methods but have the advantage of being more flexible in consideration of the acquisition geometry (it is possible to include the information which is known a priori, or obtain results for incomplete data sets).

2.2.1.3 Microtomography and synchrotron radiation

There are two kinds of X-ray sources:

— source laboratory: electrons are accelerated between a cathode and a metal anode. The bombardment of the anode by the incident electrons then causes the emission of photons X.

— source synchrotron: X-rays are produced by accelerated charged particles in a ring to relativistic velocities [Dukoo]

The advantage of sources laboratory is that it is more convenient to use for building 3-D images of snow. A laboratorial tomography can easily be placed in a cold room (For example the Swiss Federal Institute for Snow and -avalanche Research SLF, Davos) and allows to make acquisitions "in vivo" metamorphism of snow. In our study, snychrotron has been chosen because of the high resolution. Considering the image quality, synchrotron provide a resolution in a few microns for material tomography. It is currently the best possible source of X-ray and is particularly suitable for microtomography.

2.2.2 Sampling and sample preparation

The preparation of snow sample for X-ray tomography is processed in cold room. Ice and air provide a good contrast, but the snow is a fragile material, which needs to be consolidated before handling. The snow sample needs to be soaked with a substance whose melting point is slightly negative.

2.2.2.1 Sampling

The solvent 1-chloronaphthalene ($C_{10}H_7Cl$, density 1.194, melting point $-20°C$ when pure) is selected for impregnation. The impregnation (Fig. 2.5-(a)) leads to fill the open porosity of the snow. The sample is frozen (Fig. 2.5-(b)) in an iso-octane bath cooled by dry ice ($-80°C$) for solidifying the 1-chloronaphtalene, and then stored at $-22°C$ until machining. These operations allows to: (1) consolidate the snow sample; (2) preserve snow from interactions with air (e.g. sublimation), thereby stoping the metamorphism; (3) insure a correct contrast between air, ice and solvent for the X-ray tomographic acquisition.

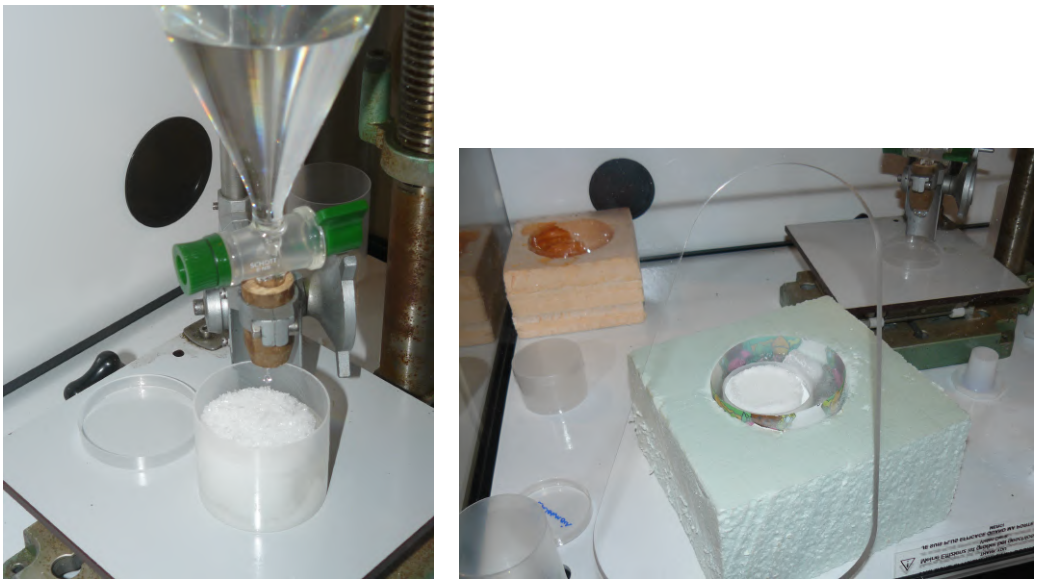

(a) Impregnation (b) Freezing

Figure 2.5 – Different steps in the consolidation of the snow sample.

2.2.2.2 Machining

The sample, after impregnating and consolidating, is strong enough to be machined. This machining process (Fig. 2.6), takes place in the cold room of CEN at a temperature around $-30°C$. Different drills provide the snow cores with different diameters according to the requirements.

The sample is then welded to the top of a copper sample holder using a drop of chloronaphthalene. It is then covered with a Plexiglas cap, avoiding ice sublimation. Each sample was stored at $-22°C$ until X-ray tomography.

2.2.3 Tomographic acquisition

2.2.3.1 Experimental device

Tomography were launched with X-Act, a software from RX solution [RXs] which is used at 3S-R laboratory in Grenoble. The X-Act beam line, designed for high-resolution images allows to obtain 3-D images of an isotropic spatial resolution of a few microns. During an acquisition (taking on average 2 hours), 1200 radiographies

(a) (b)

Figure 2.6 – Machining process and the obtained snow sample.

were obtained (in Fig. 2.8). Radiographies have a constant size of 1200 by 1200 pixels and an adjustable resolution ranging from about 5 to 9 μm, depending on the experimental set-up and the snow type.

A cryogenic cell was developped in CEN to preserve the sample during the acquisitions and also to control the temperature of the snow evolution. The base and top of the snow sample remained at well defined temperature, with the production of cold-regulated by two Peltier cells located at the outside (Fig. 2.9-$(2a + 2b)$). Peltier cells are cooled by cold water circulation (Fig. 2.9-(3)). The cold conduction between the Peltier cell and the sample is provided by a heat exchanger (Fig. 2.9-(4)) and a copper cylinder. A temperature measurement in the two heat exchangers by a probe is continuously recorded. In the center, the sample consists of a snow cylinder of 1 cm in diameter and height (Fig. 2.9-(1)). It is confined in a cylindrical sample holder in aluminum (Fig. 2.9-(6)), to ensure good conduction of the temperature at the sides of the sample. Aluminum conducts a little worse than copper (200 against 380 Wm 1.K 1) but absorbs much less X-rays, thus providing sufficient transmission necessary for

obtaining tomographic images. During the tomographic acquisition, the cryogenic cell is fixed on a rotating plateau (Fig. 2.9-(2)) and operates at temperature surrounding. To limit the influence of the outside air temperature on snow, and so avoid temperatures distortion imposed by the Peltier cell, the sample is isolated by a thickness of air at very low pressure (Fig. 2.9-(7)) between the sample holder and a plexiglass cylinder (Fig. 2.9-(8)). For this, the volume of air is pumped continuously through a diaphragm pump and a turbo-molecular pump connected in series (Fig. 2.9-(9)). This device allows us to achieve a vacuum of 0.1 Pa in the enclosure. At constant temperature, the thermal conductivity of the air decreases with pressure as shown in Fig. 2.10. Thus, this vacuum of 0.1 Pa achieves a conductivity of 0.001 $Wm^{-1}\ K^{-1}$ at ambient pressure (conduction divided by 28). The pressure value is measured by a Pirani gauge (Fig. 2.9-(10)) and recorded every minute during the period of use of the cell. At this stage of cell development, we hypothesized that other phenomena of heat transfer (like radiation) that could affect our snow sample are negligible compared to conduction.

2.2.3.2 Reconstruction and analysis

2-D image in grey scale reconstructions are performed from radiographies in Laboratory 3S-R with a software DigiCT [Dig]. The characteristics of synchrotron radiation produce the reconstructed images in very good quality, although some persist artifacts (including "ring artifacts" caused by problems of sensitivity of the detectors). Despite the process of impregnation, it still remains some air bubbles in the medium. These images obtained after reconstruction have three phases (ice, chloronaphthalene and air) and some artifacts. The range of gray levels of the different phases are divided as follows:

— Air: from 0 to 110 average 60

— Ice: from 60 to 160 average 100

— Chloronaphthalene: from 80 to 250 average 180

A simple thresholding is not effective for ranges of gray levels with a large common area, especially for ice and air. They represent huge amount of data.

For the images shown in the following chapters, we are therefore limited to vol-

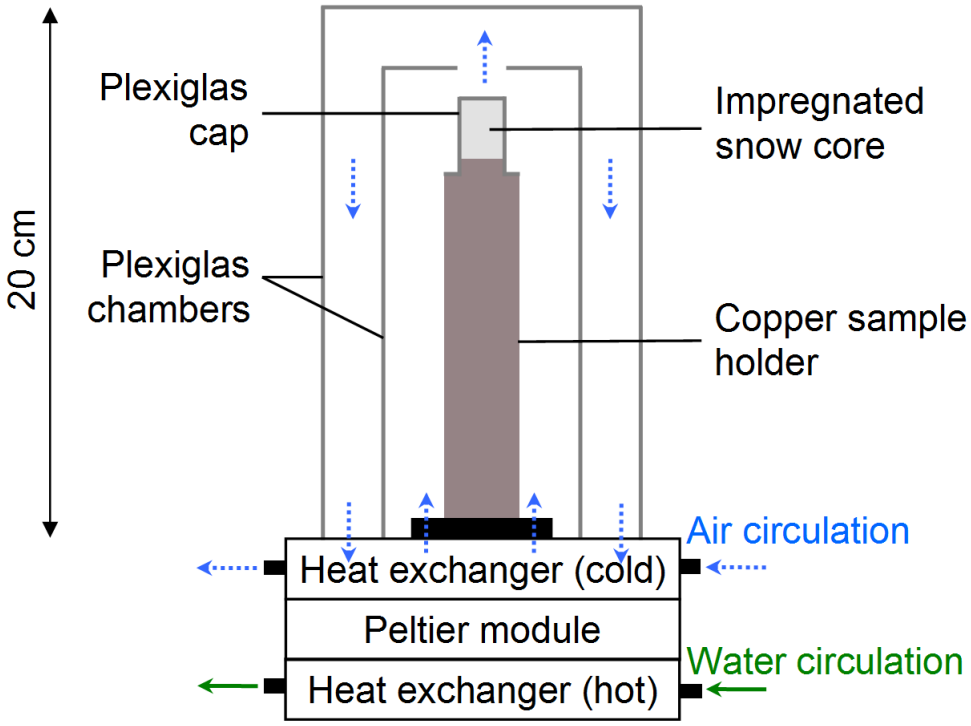

Figure 2.7 – Illustration of one of the cryogenic cell used during tomographic acquisitions ([CFG+14]).

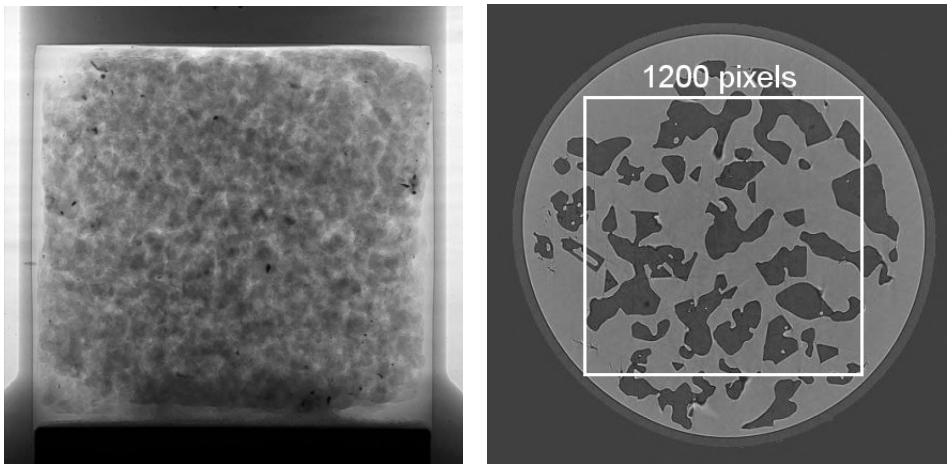

(a) (b)

Figure 2.8 – Snow image obtained by absorption microtomography: (a) is one of the 1200 radiographies, (b) is one of the horizontal reconstructed slice.

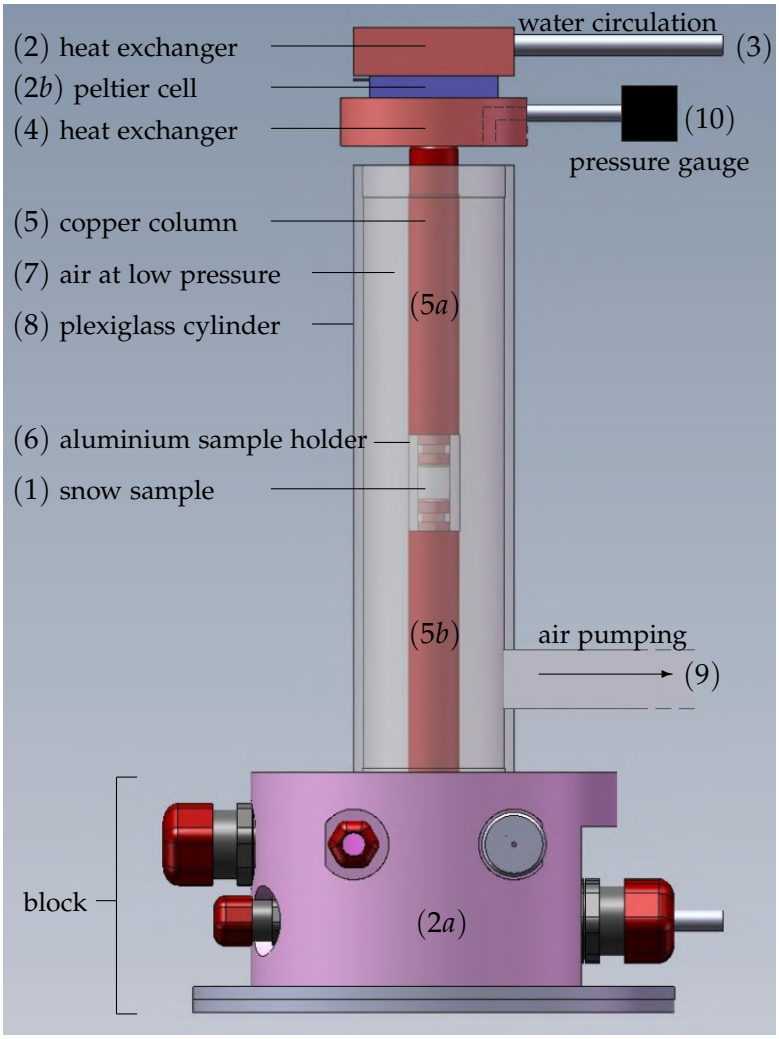

Figure 2.9 – The new cryogenic cell scheme.

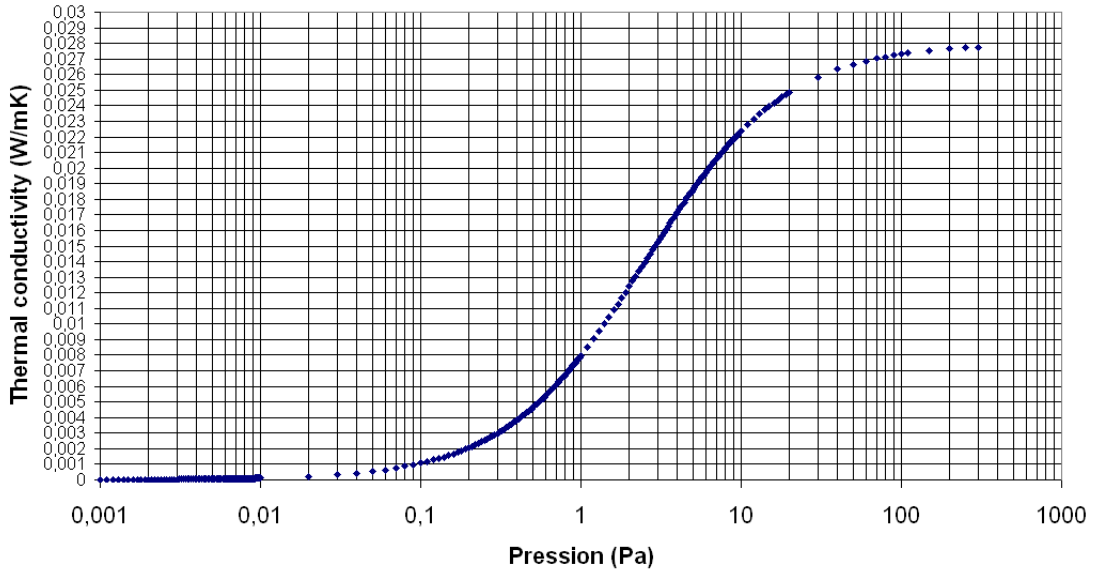

Figure 2.10 – Thermal conductivity of air depending on the pressure, when $T = 25°C$.

umes of 256^3 voxels included in the cylinder of snow. Moreover, the data format, initially in real (16 bits), has been converted into unsigned integers (8 bit). Values are between 0 and 255. It is 1.7 GB for each sample.

A method proposed in [LBC+03] is used for transforming a set of 2-D image in gray scale into a binary 3-D image consisting of gray level where the voxels of ice to 1, the others to 0.

The first step consists of a noise reduction by a mean filter 3×3 (Fig. 2.11). The details of main steps are presented in the following sections.

Air bubbles detection : At the begining, the areas of air bubbles are detected on each plane and the average gray level of the pores (chloronaphthalene) should be assigned. The consequences of the phase shift of x-rays through the sample are used to mark these air zones. Normally, there is an obvious contrast between air and chloronaphthalene, an area of high gradient (see Fig. 2.12). The thresholds "black", "white", "strong gradient", as well as the average value in chloronaphthalene are determined by examining the histograms on a smoothed image and the gradient magnitudes obtained with Prewitt filter.

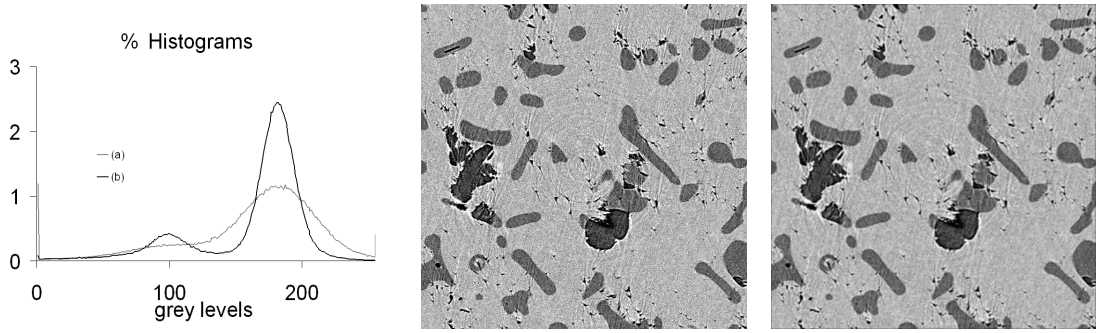

(a) (b) (c)

Figure 2.11 – Smooth the image with a mean filter: (a) histogram of image initial (parabola - (b)) and image smoothed (parabola - (a)), (b) initial image, (c) smoothed image.

An automatic procedure creates the three binary images from three thresholds described above. The logical union of these three images mark the bubbles. Then a morphological operator closure is utilised for filling allowed holes, in most cases, the surface of the air zones.

Thresholding : The binary mask obtained above, affected the average gray level value of chloronaphthalene, is then inserted into the original image. The "speckled" noise are eliminated by applying a median morphological filter. This filter, based on a combination of openings and closures, operates as follows on each plane:

$$g = \max[\min(f, COC(f)), OCO(f)] \tag{2.15}$$

where f and g indicate respectively the initial image and smoothed image, C and O are morphological operators of opening and closure.

A 3-D mean filtering ($5 \times 5 \times 5$) is then applied. The image is now ready for automatic thresholding by method of factorization. This algorithm finds the threshold value by minimizing the sum of variances of gray levels in the two regions defined by the threshold. An mean 3-D filter ($3 \times 3 \times 3$) is then applied on the binary images. The process is shown in Fig.2.13 .

Verification and corrections manually : The similarity of the binary image over-

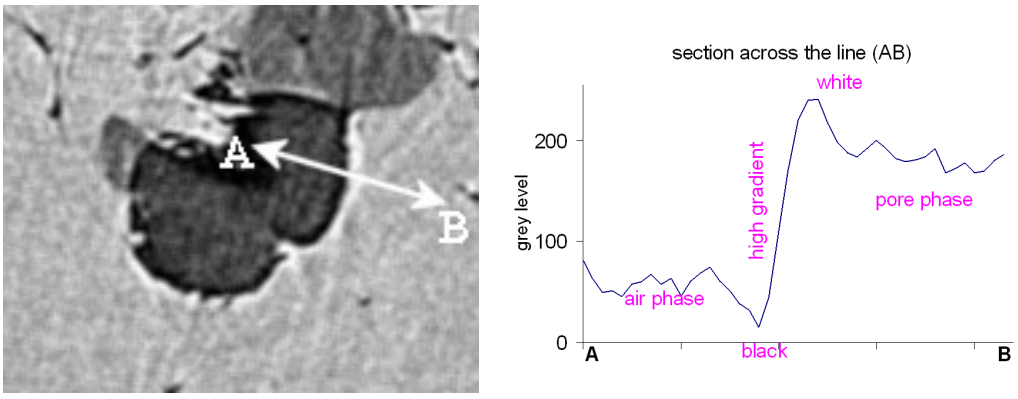

(a) (b)

Figure 2.12 – High gradient of gray level around air bubble: (a) air bubble is in black, ice is in dark region and the chloronaphthalene is in light area, (b) the gradient of gray level between the segment AB.

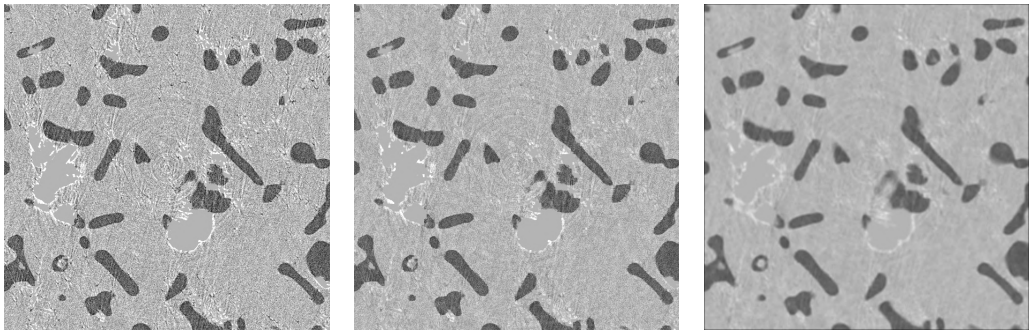

(a) (b) (c)

Figure 2.13 – Remove the air bubbles using the binary mask: (a) insert a binary mask in initial image, (b) remove "specks", (c) smoothed image.

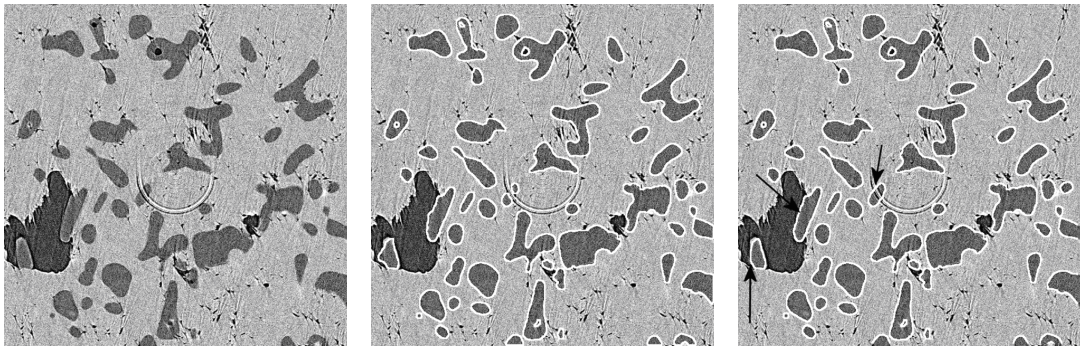

(a) (b) (c)

Figure 2.14 – Problems after automatic image analysis: (a) initinal image, (b) result after image processing, (c) manual correction.

laid with the original image to grayscale is inspected visually for each plane. This examination showed that the image results were corrected about $80-85\%$ of the planes. Two types of problems still present on the 20% of the remaining planes:

— Artifacts: a part of the information is lost when they through an area of ice.

— Air zones contiguous with ice: a part of the air area is merged with the ice because of the absence of very high gradient between the two phases.

In both cases, A manual corrections is adopted. Fig. 2.14 shows a plane which is present both types of problems (a), the result of automatic processing (b) and corrected with corrections marked by arrows (c) picture.

2.2.4 Diffraction Contrast Tomography

In addition to classical absorption tomography, X-ray Diffraction Contrast Tomography (DCT) [LRK$^+$09, RKP$^+$11] was used for understanding how snow deforms at the grain scale in a non-destructive way. By combining X-ray diffraction analyses and absorption tomography, it provides simultaneously: the 3-D geometry of the ice-air interface; the 3-D mapping of individual grains; and their crystalline orientation.

DCT is a methodology that allows the simultaneous reconstruction of 3-D grain shapes and orientations. Its experimental apparatus and set-up process are similiar to those which are used for synchrotron X-ray microtomography. In both cases, a

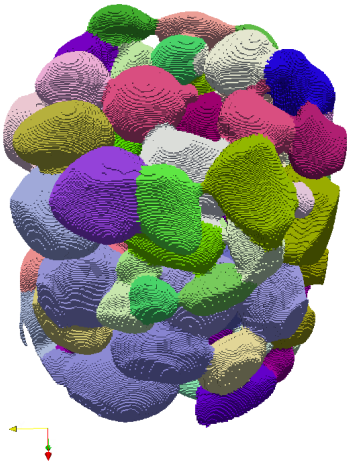

Figure 2.15 – The 3-D snow sample obtained by DCT with size 270^3 (MF sample).

series of radiographs are formed after placing the sample on a rotate platform and irradiating by a parallel and monochromatic synchrotron X-ray beam. Each grain will pass through Bragg diffraction which is first proposed by William Lawrence Bragg and William Henry Bragg in 1913 [Bra13] alignments multiple times during rotating to produce diffracted beams. Beams diffracted at small angles will be captured on the detector that covers an area substantially bigger than sample. Therefore, the size of X-ray beam cross-section is adjusted to the sample size (using horizontal and vertical slits) to allow the remainning detector area being used for collecting diffraction spots. In the absence of orientation and stain gradients inside the grains, the diffracted beam form 2-D spots that can be treated as paralle projections of the diffracting grain [Klu11]. Then analysis of Friedel pairs [Fri13] of these diffracion spots allows one to determine the crystallographic orientation and 3-D shape of grains in the sample.

For some particular snow structures (e.g. MF) presented in Fig. 2.15, each geometric grain exhibits a particular crystalline orientation so that the DCT can actually provide a physically-based shape decomposition of the granular structure.

However, the DCT method may fail in some cases so that interfaces between grains are sometimes inaccurately located. To improve the image quality, the raw experimental images have been slightly modified by using the following process:

— For each grain, which is identified by a specific label, the connectivity is first checked. If the grain is constituted of separated volumes, the label of the largest volume of the grain is conserved, while the remaining parts are set to the label of the grain that shares the most of the contact surface with this volume.
— The shape of each grain is then tested in order to insure its relative convexity: all voxels located far from the grains center of mass and whose neighborhood contains too few voxels of the same label are labeled as belonging to undefined regions.
— Such undefined regions are then labeled by a region growing algorithm propagating from the grains that have been previously identified.

2.3 Introduction to digital geometry

Digital geometry deals with the geometric properties of subsets of digital pictures and with the approximation of geometric properties of objects by making use of the properties of the digital picture subsets that present the objects [KR04, CMC07]. In this section, we will present some basic concepts and algorithms of digital geometry which will be used to define the decomposition algorithms later.

2.3.1 Voxels and neighborhood

In digital geometry, an object in 3-D is presented by a set of cubes called voxels. These voxels centered on the grid $\mathbb{Z}^3$, are equivalent to pixels in 2-D. On the discrete space, the notion "neighborhood" is used to detect whether two voxels are adjacent or not. In 3-D, 6-, 18-, or 26-neighborhood are introduced considering adjacencies by faces, edges and vertices (see table 2.3 and Fig. 2.16).

Table 2.3 – Characterization of 3-D adjacences of $A(x_A, y_A, z_A)$ and $B(x_B, y_B, z_B)$

adjacences	**characterization**
6	$\lvert x_A - x_B\rvert + \lvert y_A - y_B\rvert + \lvert z_A - z_B\rvert = 1$
18	A and B are 26-neighbors and $\lvert x_A - x_B\rvert + \lvert y_A - y_B\rvert + \lvert z_A - z_B\rvert \leq 2$
23	$\max(\lvert x_A - x_B\rvert, \lvert y_A - y_B\rvert, \lvert z_A - z_B\rvert) = 1$

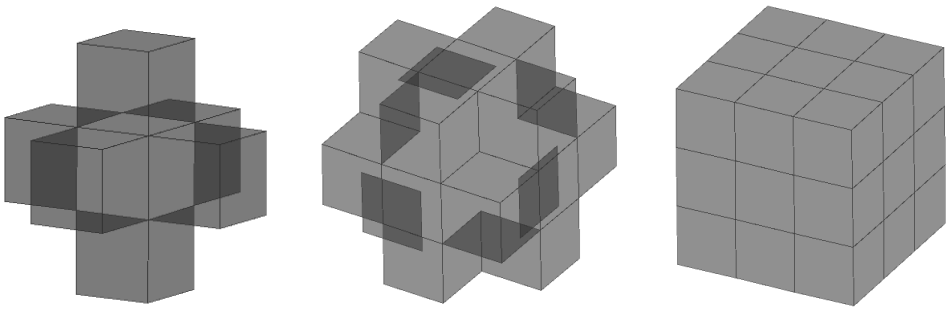

(a) 6-neighborhood (b) 18-neighborhood (c) 26-neighborhood

Figure 2.16 – different neighborhoods of the central cube in 3-D.

2.3.2 Euclidean distance transform

In binary images, the Distance Transform (DT) is a classic tool for shape analysis. It is a derived representation of a digital image. The distance transformation consists in labeling each point of object X with the distance to the nearest voxel in complement of X (denoted $\overline{X}$).

Usually the transform is qualified with the chosen metric: chamfer masks [RP68, FM05], the vector displacement-based Euclidean distance [Dan80, CM99] and so on. The chamfer distance transformation is easy to compute, but it is not a good approximations of Euclidean distance. From a computational point of view, several methods lead to time optimal algorithms to compute the error-free Euclidean distance transform for d-dimentional binary images [BGKW95, GM98, MQR03]. In dimension 2, such approaches lead to efficient two-pass squared Euclidean distance transformation (SDT for short). The process in 2-D is illustrated in Fig.2.17.

In 2-D case, a binary image P in size $n \times n$. Its complementary is denoted by $\overline{P}$, i.e., the set of background pixels. For each point (i, j) of P, the squared Euclidean distance transformation is given by:

$$h(i,j) = min(i-x)^2 + (j-y)^2; 0 \leq x, y < n, (x,y) \in \overline{P} \tag{2.16}$$

In first step, a one-dimensional eucliean distance map G is obtained according to

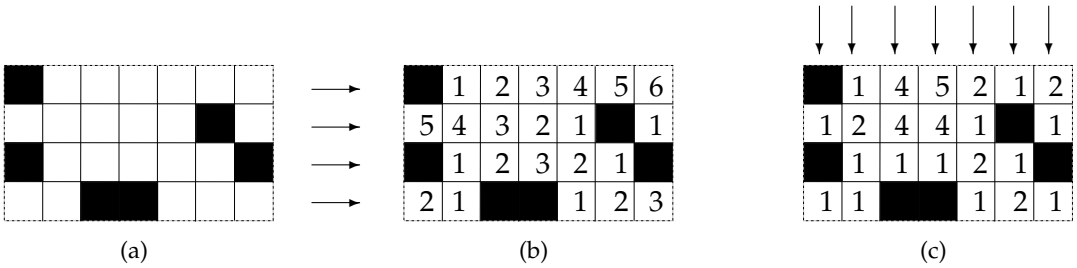

Figure 2.17 – Process of SDT algorithm: (a) the binary image P, (b) the map G obtained in first step, (c) the finial SDT map H after the last process along the y-axis.

x-axis:

$$G = \{g(i,j)\} = \{\min_x\{\mid i - x \mid; 0 \leq x < n, (x,j) \in \overline{P}\}\} \tag{2.17}$$

In second step, finial distance transform is constructed with a y-axis:

$$H = \{h(i,j)\} = \{\min_y\{g(i,y)^2 + (j-y)^2; 0 \leq y < n\}\} \tag{2.18}$$

SDT gives a better approximation of real valued Euclidean distance between voxel centers. The representation of digital image with Euclidean distance transformation using SDT is illustrated in Fig. 2.18.

2.3.3 Voronoi diagram and Delaunay triangulation

In mathematics, diagrams are defined in metric spaces for countable sets S of "simple" geometric objects such as points, line segments, polygons, polyhedra, and so on. One type of diagram divides the metric space into cells such that each element of S is contained in exactly one cell [BCKO08].

Let $S = \{p_1, ..., p_n\}$ be a set of points in the plane $\mathbb{R}^2$. The Voronoi cell of $p_i \in S (i = 1, ..., n)$ is the closure of its zone influence, which is the set of all points in $\mathbb{R}^2$ that are closer to p_i than to any other point of S (see Fig. 2.19-(a)). The definition of Vornoi cell is:

$$V_e(p_i) = \{q : q \in \mathbb{R}^2 \wedge d_e(q, p_i) \leq d_e(q, p_j), j = 1, ..., n\} \tag{2.19}$$

Euclidean distance was used in this definition, but Voronoi cells can be defined in any

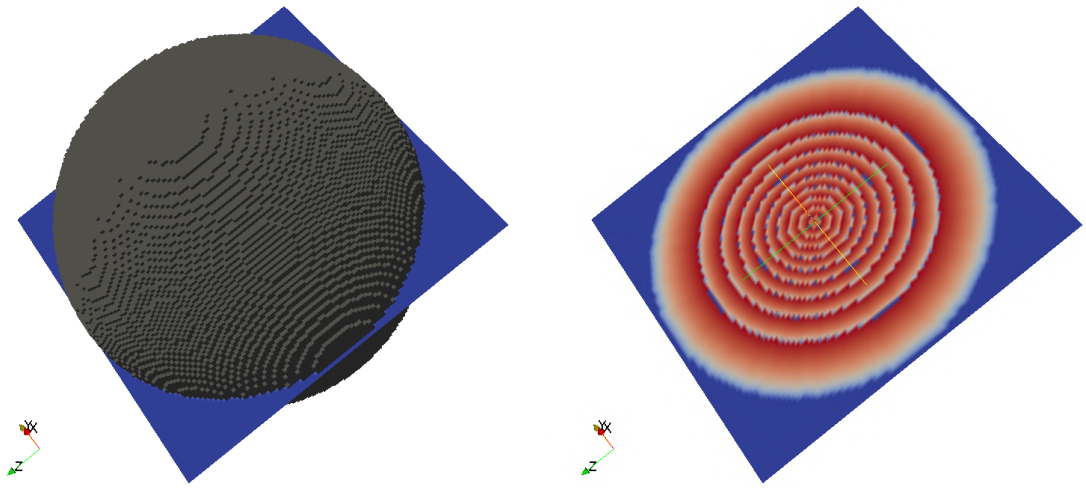

(a) (b)

Figure 2.18 – Sphere and a slice of its distance transformation.

other metric space. The sets $V(p_i)$ are convex polyhedra with null measure since the set of points that have the same distance from two points in S forms a hyperplane. Voronoi cells are $(d-k+1)$ - dimensional Voronoi facets if closed facets shared by k, $2 \leq k \leq d$ and Voronoi vertices if the points shared by $d+1$ or more. Voronoi objects denotes either a Voronoi cell, facet or vertex. The Voronoi diagram is the collection of all Voronoi objects.

Definition 2.2 (Voronoi diagram)**.** *The Voronoi diagram of S is the union of the frontiers of the Voronoi cells* $V_e(p_i)$ $(i = 1, ..., n)$.

If we consider the dual graph of Voronoi diagram, that is the graph such that the nodes are sites and the edges of the adjacences between cells of the diagram, then we obtain a triangulation of sites which is called Delaunay triangulation (see Fig. 2.19-(b)).

In the digital geometry, we have similar definition of Voronoi diagram and Delaunay triangulation.

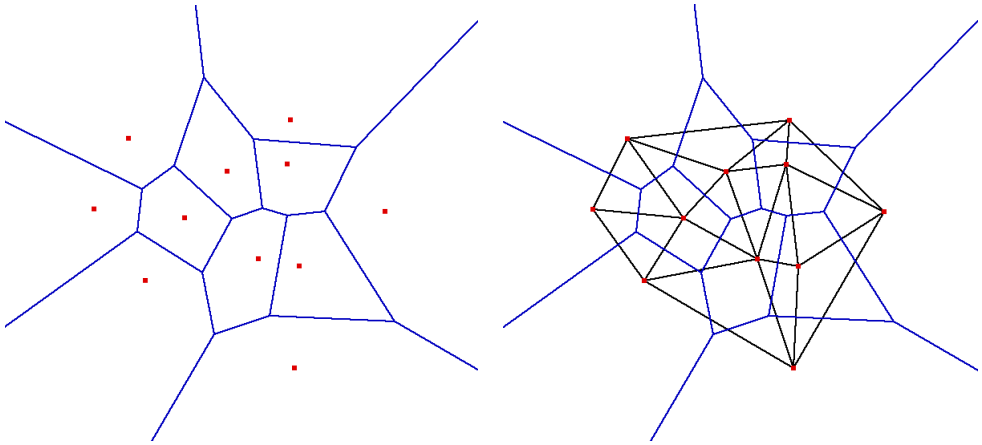

(a) (b)

Figure 2.19 – Voronoi diagram in $\mathbb{R}^2$ (a), and its Delaunay triangulation (b).

Definition 2.3 (Digital Voronoi diagram). *$P = \{p_i\}$ is a set of sites in the digital space, the digital Voronoi diagram is a decomposition of the space into subsets $\{c_i\}$, such that each point c_i is closer to p_i than each p_j $(j \neq i)$.*

Definition 2.4 (Digital Delaunay triangulation). *the digital Delaunay triangulation, is the dual structure of the digital Voronoi diagram of points $\{p_i\}$.*

An optimized Reversed Euclidean Distance Transformation (REDT) is proposed in [CM07]. Based on such algorithm, we can compute a digital Voronoi diagram which is time optimal.

2.3.4 Power diagram

With the wide applications of Voronoi diagram, researchers are aware that many practical situations are better described by some modification than by the original diagram [Aur87]. A concept of weighting the given points is provided. For a finite set $M \subsetneq \mathbb{R}^d$, each point $p \in M$ has assigned an individual real number $w(p)$, the wight of p, and the distance of a point $x \in \mathbb{R}^d$ is measured as a function of $d(x,p)$ and $w(p)$. Power diagram is concerned with the distance function $d(x,p)^2 - w(p)$.

Definition 2.5 (Power diagram). *Let S denote a finite set of spheres in $\mathbb{R}^d$. For $s \in S$, the set $cell(s) = \{x \in \mathbb{R}^d | pow(x,s) < pow(x,t), \forall t \in S - \{s\}\}$ is the power cell of s. The*

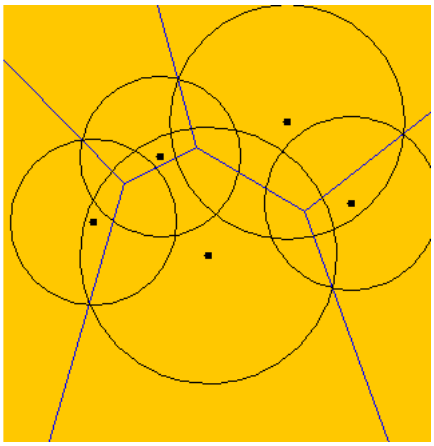

Figure 2.20 – Power diagram on a set of spheres in 2-D.

collection of all cell is the power diagram of S.

The power of a point x with respect to a sphere $s \subsetneq \mathbb{R}^d$ with center z and radius r is defined as $pow(x,s) = d(x,z)^2 - r^2$. Thus $pow(x,s) < 0$ if x lies in the ball s, $pow(x,s) = 0$ if x on the boundary of s, and $pow(x,s) > 0$ otherwise. Fig. 2.20 illustrate the power diagram on a set of spheres in 2-D.

2.3.5 Surface curvature estimation

In mathematics, curvature refers to any of a number of loosely related concepts in different areas of geometry. Intuitively, curvature is the amount by which a geometric object deviates from being flat, or straight. Two kinds of curvature exist on 2-D surfaces embedded in $\mathbb{R}^3$: Gaussian curvature and mean curvature. Normally, mean curvature can be defined by principal curvatures (see Fig. 2.21).

$$C = \frac{k_1 + k_2}{2} \tag{2.20}$$

The Gaussian curvature G is often defined as:

$$G = K_1 K_2 \tag{2.21}$$

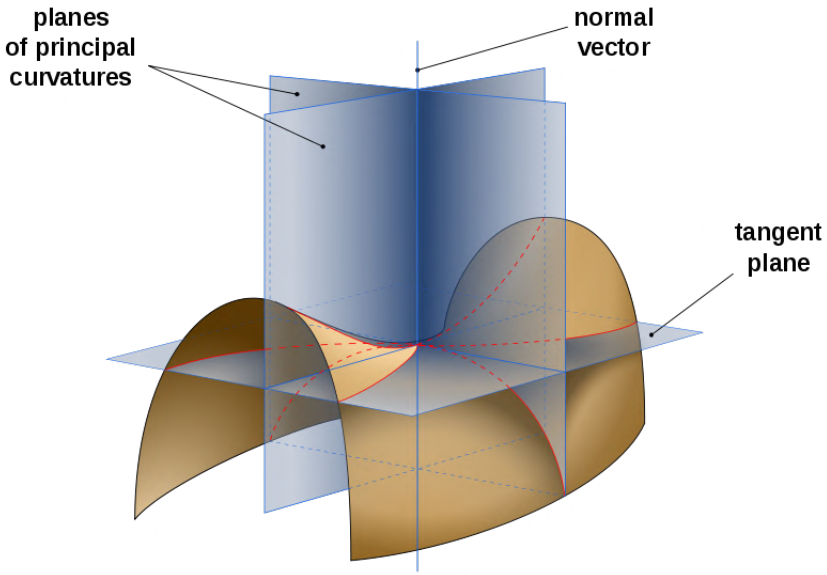

Figure 2.21 – Principle curvature.

$k_1 = 1/r_1, k_2 = 1/r_2$, where r_1 and r_2 are the principal radii of curvature of the surface $\sum$ at point p.

However, these definitions are less suited to express C and G when describing in numerical surface. There are many methods for computing the mean [BGCF95, Len99] and Gaussian [BFO07, BGCF95, Boi95] curvature in digital domain. In our work, we are interested in different curvatures on discrete 3-D surfaces. On a theoretical level, these measures are important elements of a discrete surface. From a practical point of view, these measures also have applications in snow physics.

Mean curvature

In our method, mean curvature is computed from the largest relevant neighborhood [WGFC12]. It is defined as the divergence of the normal vector map:

$$C(p) = \frac{div\,\overrightarrow{n}(p)}{2} \tag{2.22}$$

where point p is on the surface, normal vector field $\overrightarrow{n}(p)$ is estimated using method [FBL+01].

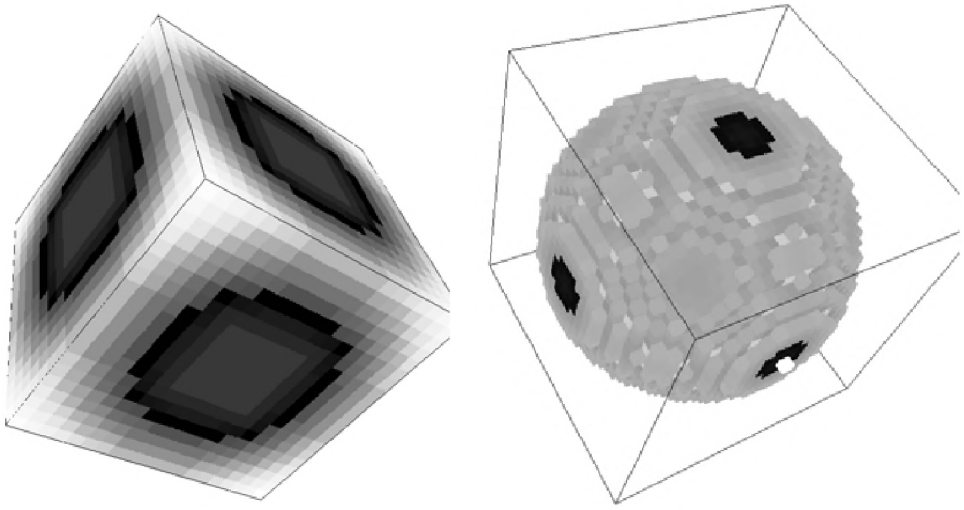

(a) (b)

Figure 2.22 – Examples of mean curvature map (by Coeurjolly [Coe02]).

Gaussian curvature

The Gaussian curvature G used in segmentation method is defined as:

$$\begin{aligned} G(p) = \frac{\begin{aligned} &\phi_x^2(\phi_{yy}\phi_{zz} - \phi_{yz}^2) + \phi_y^2(\phi_{xx}\phi_{zz} - \phi_{xz}^2) \\ &+\phi_z^2(\phi_{yy}\phi_{xx} - \phi_{xy}^2) \\ &+2\phi_x\phi_y(\phi_{xz}\phi_{yz} - \phi_{xy}\phi_{zz}) \\ &+2\phi_y\phi_z(\phi_{xy}\phi_{xz} - \phi_{yz}\phi_{xx}) \\ &+2\phi_x\phi_z(\phi_{xy}\phi_{yz} - \phi_{xz}\phi_{yy}) \end{aligned}}{(\phi_x^2 + \phi_y^2 + \phi_z^2)^2} \end{aligned} \tag{2.23}$$

with ϕ being the signed distance map DT^* at point p and the subscripts x, y, z denoting the partial derivatives along the x, y, z coordinates, respectively. Note that since we are using an exact Euclidean metric for DT^*, ϕ and its derivatives are stable to rotations.

2.4 Geometric grain analysis in 3-D

The model that simulates the evolution of snow metamorphism is essential for avalanche risk forecasting. Existing models are usually obtained using grain silhouettes of isolated grains [LPM98] or 2-D thin section analysis [EB91, Goo87, BES94]. In this section, the numerical tools to characterize the microstructure of snow in order to help for metamorphism modeling. Theoretically, porous materials such as snow can be described by their porosity, specific surface area, and curvature.

Porosity (P) : is a ratio of the pore volume to the total volume of snow sample. The evolution of this ratio link to the packing of snow during metamorphism. It can be caculated by the equation 2.24 or from the density of snow (see equation 2.1).

$$P = \frac{\sum^{p \in D} f(p)}{N_D} \tag{2.24}$$

where p indicates the number of voxels belonging to the pore in object D; N_D is the total voxels of object; and $f(p) = 1$ for p in the pore, 0 otherwise.

Specific surface area : is a property of solids which is the total surface area of a material per unit of mass, solid or bulk volume, or cross-sectional area. In snow, it is defined by the total surface area of the air/ice interface per mass unity of the considered sample. SSA is an important physical property of snow that contributes to snow metamorphism. It can be caculated by the equation 2.25

$$SSA = \frac{S_D}{\rho N_D l_0} \tag{2.25}$$

where S_D is surface area of snow sample. S_D is obtained by summing all the contributions $g(p)$ in D. Parameter $g(p)$ is a weight for each surface of voxel p that is computed by equation 2.26. ρ is the ice density and l_0 is the size of one voxel.

$$g(p) = \frac{1}{\max(\mid n_x(p) \mid, \mid n_y(p) \mid, \mid n_z(p) \mid)} \tag{2.26}$$

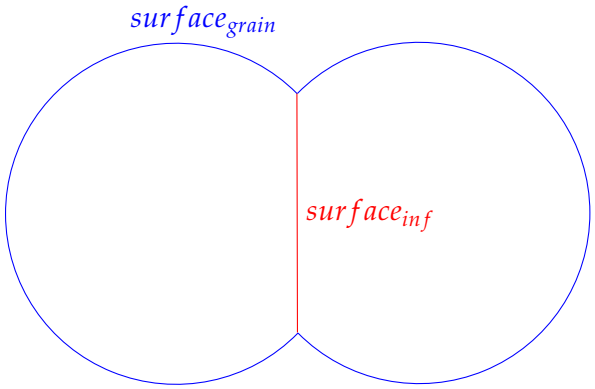

Figure 2.23 – A model to study the properties of snow microstructure.

where $n_x(p)$, $n_y(p)$, $n_z(p)$ are the projections of $\vec{n}(p)$ along the three coordinates of the voxel grid. Vector $\vec{n}(p)$ is caculated on each surface of voxel p by the method in [FBL+01, CFTT03].

Specific grain contact area : is an importantal parameter for characterizing in snow research. It is defined as the total interface area between each two grains per unit mass of snow sample.

$$SGCA = \frac{surface_{inf}}{mass_{tot}} \tag{2.27}$$

From Fig.2.23, we can notice that the relationship among SSA, SSA_{tot} and $SGCA$. Generally, $SSA = \frac{surface_{grain}}{mass_{tot}}$ and $SSA_{tot} = \frac{surface_{tot}}{mass_{tot}}$. $surface_{tot} = surface_{grain} + surface_{inf}$. So SGCA can be calculated from:

$$SGCA = (SSA_{tot} - SSA)/2 \tag{2.28}$$

Mean and Gaussian curvature : are defined in section 2.3.5. Both are useful in describing the microstructure of snow. The mean curvature plays a significant role in interfacial thermodynamics, while Gaussian curvature can be used to characterize the mechanical properties.

2.5 3-D Shape Segmentation on snow application

Currently, there are serveral approaches for shape segmentation problem. Consider the various types of snow sample, we can categorize them into 3: grains rouned and spherical; grains convexes and grains with sharp interfaces or complex structures (see Fig.2.24). For the grains which are rouned or spherical, we can use the morphology tools such as watershed transform. Watershed method describes a grey-level image as a topographic relief, where the grey level of a pixel is interpreted as its altitude in the relief. A drop of water falling on a topographic relief flows along a path to finally reach a local minimum. Intuitively, the watershed of a relief correspond to the limits of the adjacent catchment basins of the drops of water (Fig.2.25, [BF93]). For the convexes grains, the informations of curvatures on the surface are usually used. However, when applying to snow application, the results are not accurate enough to meet our requirements because of the structure or size of snow grain. And for the third category: grains with sharp interfaces or complex structures, there are not a satisfactory solution. It is necessary to develop a new method which is less sensible to the structure or size of snow grains.

2.6 Conclusion

Snow transforms with time, depending on the parameters of environment, called metamorphism. The study of this process is very important in the snow reserch. To improve the current knowledge of snow metamorphism, realistic simulations of snow morphological changes with time and comparisons to quantitative measurements of snow microstructure are mandatory. Furthermore, physical and mechanical properties of snow are strongly depending on its microstructure. A parameterization of physics and mechanics of snow in micro-scale is introduced in section 2.1.1.

X-ray tomography as one of imaging technique is chosen for obtaining numerical 3-D snow microstructure images. It is powerful, non-destructive and can allow to build a high resolution image for our study. Some principle of X-ray microtomography is introduced in section 2.2.1. Besides the X-ray tomography, DCT is another method we used for analysis the microstructure of snow. It provides the crystalline orientation

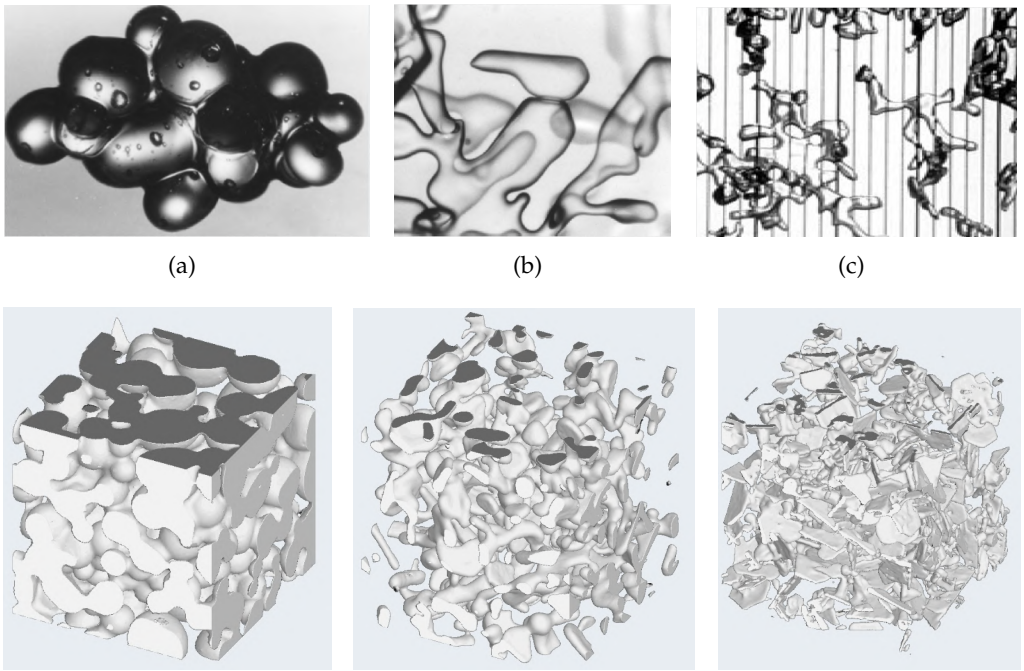

(a) (b) (c)

(d) (e) (f)

Figure 2.24 – Examples of 3 categories of snow sample in 2-D and 3-D. $(a)(d)$ are grains rouned and spherical; $(b)(e)$ are convex grains; $(c)(f)$ are grains with sharp interface or complex structure.

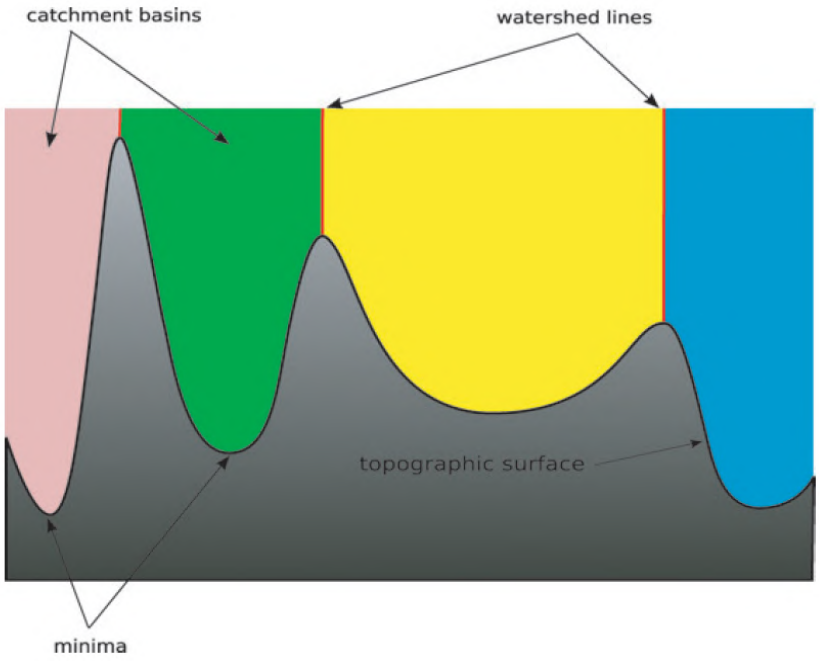

Figure 2.25 – Watershed transform.

of each grain. So a physically-based decomposition of snow grain is obtained by DCT. However, DCT can not work as well as all types of snow structures. In the next chapter, a novel method is developped for extract the grains in snow microstructure. Some basic geometric algorithms help to solve the grain segmentation problem. We describe the definitions in section 2.3. Section 2.4 presents the numerical algorithms we used to obtaine the geometrical information describing the snow 3-D numerical images.

Chapter 3

Article: Curvature-Driven Volumetric Segmentation of Binary Shapes: an Application to Snow Microstructure Analysis

Contents

3.1 Context

In this section, we detail the context and practical reasons that led to develop a first algorithm for grain segmentation of snow microstructure.

As we discussed in chapter 2, the study of microstructure of snow is the fundation of simulation of snow metamorphism. The snow grains, as the smallest elements that are consistent with snow physics and mechanics, play a very important role in the microstructure of snow. Diffraction contrast tomography (in section 2.2.4), which can exhibit a particular crystalline orientation of each grain allows to segment the snow sample into individual grains. However, it is only available for some particular types of snow structures. There are 9 main classes of snow shapes: Precipitation Particles (PP), Machine Made snow (MM), Decomposing and Fragmented precipitation particles (DF), Rounded Grains (RG), Faceted Crystals (FC), Depth Hoar (DH), Surface Hoar (SH), Melt Forms (MF) and Ice Formations (IF) [FAD+09]. Fig. 3.1 presents 6 types of snow samples we used in our study. They are described with the information of mean curvatures of surfaces. Each has different physical characteristics and geometries. In Fig. 3.2-(a), we can notice that the mean curvatures on the surface are not enough to indicate the grains and necks. Development of an efficient numerical tool to segment the grains from various types of snow shapes is a challenge. In Fig.3.2-(b), the snow sample is described with the information of Gaussian curvature. We can notice that the surface of the snow sample can be easily identified into: convex (red) and concave (green) shapes, which correspond to grain and neck regions, respectively. In the following, a segmentation method based on this concept is proposed.

This chapter corresponds to an article published in IEEE Computer Society, International Conference on Pattern Recognition, 2012.

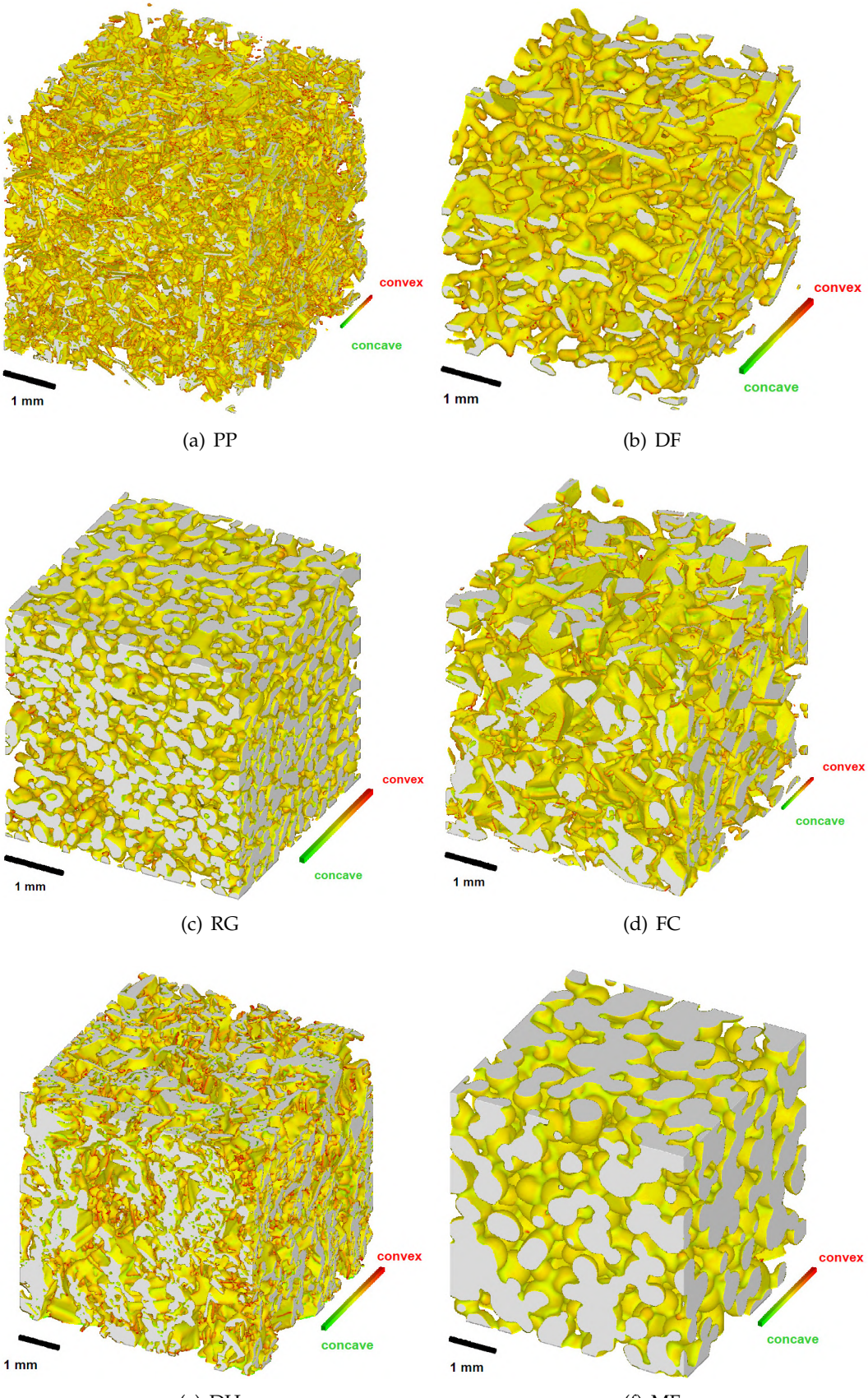

(a) PP (b) DF

(c) RG (d) FC

(e) DH (f) MF

Figure 3.1 – 3D visualization of the microtomographic images in different classes of grain shapes where colors represent the mean curvature of surfaces, such as surface convex, flat or concave are shown in red, yellow and green, respectively ([CFM+11], auxiliary materials).

3.2 Article: Curvature based grain segmentation method

Curvature-Driven Volumetric Segmentation of Binary Shapes: an Application to Snow Microstructure Analysis

X. Wang L. Gillibert F. Flin
CEN / CNRM - GAME URA 1357 / Météo-France - CNRS, 38400 Saint Martin d'Hères, France
xi.wang@liris.cnrs.fr, luc.gillibert@meteo.fr, frederic.flin@meteo.fr

D. Coeurjolly
CNRS - LIRIS UMR 5205, Université de Lyon, 69622 Villeurbanne, France
david.ceurjolly@liris.cnrs.fr

Abstract

Many three-dimensional (3-D) image-based studies concerning granular and sintered materials require a description of the observed microstructures in terms of individual grains. We propose a robust segmentation algorithm which identify groove regions on the object's surface in order to locate possible grain boundaries in the object's volume. The algorithm relies on the volumetric propagation via Voronoi labeling of curvature information from the surface into the object[1].

1. Introduction

The study of well-sintered granular materials like ceramics, metallic alloys [6] or even deposited snow on the ground [2] requires a precise description of their 3-D microstructure in terms of individual grains and bond's characteristics. Such a description is a key-point to diverse studies like mechanical simulations or analysis of sintering mechanisms [1]. Commonly used 3-D imaging methods such as *Computed Tomography* (CT) or *Magnetic Resonance Imaging* (MRI) provide precise information about the geometry of the interface between the considered phases (e.g. the matrix of a pure material and its associated pore space). However, they do not provide any direct information about the internal structure of phases, which may consist of several *grains*. The purpose of this paper is to propose a grain segmentation algorithm that can deal with images of highly sintered grains and to demonstrate its validity by using appropriate experimental techniques. In our context, we aim at decomposing a binary volumetric object into snow grains defined by specific crystalline orientations. However, as discussed above, such information cannot be retrieved from the CT image and we geometrically characterize grains as smooth structures connected to others by grooves and necks. In computer vision or shape modeling, two main classes of approaches exist to decompose a shape into smaller parts: On the one hand, we can consider shape decomposition algorithms based on the determination of the medial axis. From the large bibliography on that subject, we can mention solutions either from computational geometry [4], or digital geometry [13]. On the other hand, we can use mathematical morphology operators to segment the input 3-D volume into grains (see [12] for a survey). In the considered problem where well-sintered grains are characterized by slight surface variations, surface differential descriptors such as curvatures are particularly suited to guide the volumetric segmentation. However, none of the two frameworks mentioned above provides precise surface measurements to guide the volumetric segmentation. Another option could be to consider Zhang et al.'s technique [14], which involves the Gaussian curvature G as a means of separating "parts" from a triangulated object for CAD purposes. However, this method presents two major drawbacks for its direct application to snow images. First, the method seems difficult to adapt to large voxel data sets known presently to "resist" triangulation for reasons of CPU time, memory and topology. Second, the Zhang et al.'s method separates typical shapes from a surface, but does not really provide a volumetric segmentation into individual grains.

In the present paper, we propose a robust curvature-

[1]The authors thank the ESRF ID19 beamline where the experimental data have been acquired. This work has been mainly funded by the SNOW-WHITE ANR-06-BLAN-0396 and DIGITALSNOW ANR-11-BS02-009 research grants.

based grain segmentation algorithm that solves the previous drawbacks and can deal with usual 3-D images obtained by X-ray absorption tomography to provide an appropriate mapping of the grains. After recalling some basic definitions, we will present the Curvature-Driven Grain Segmentation (CDGS) algorithm in details.

2. Preliminaries

In the following, we consider a binary object $\mathcal{O}$ as grid points with value 1 of a mapping from $\mathbb{Z}^3$ to $\{0,1\}$. According to our application, grid points with value 1 are associated with ice material and we aim at decomposing $\mathcal{O}$ into grains. Let us first define the distance transformation of $\mathcal{O}$ and its Voronoi labeling that will be used for the volumetric propagation.

Definition 1 *For each point $p \in \mathcal{O}$, the* distance transform *value $DT_{\mathcal{O}}(p)$ at a point $p \in \mathcal{O}$ is defined as follows:*

$$\forall q \notin \mathcal{O}, DT_{\mathcal{O}}(p) = \min[d(p,q)] \quad (1)$$

where $d(x,y)$ denote the Euclidean distance between p and q. The Voronoi labeling $V(p)$ at p corresponds to the point q minimising the distance transformation. I.e.:

$$\forall q \notin \mathcal{O}, V_{\mathcal{O}}(p) = \text{argmin}_q[d(p,q)] \quad (2)$$

In computer imagery, both the distance transform and the Voronoi labeling have been widely investigated since decades [7, 3]. From a computational point of view, if $\mathcal{O} \subset [0,n]^3$ both transforms can be obtained in $O(n^3)$ for the Euclidean metric without error. Without changing the overall complexity, a *signed distance* $DT^*(p)$ can be obtained as follows $DT^*(p) = DT_{\mathcal{O}}(p)$ if $p \in \mathcal{O}$ and $DT^*(p) = -DT_{\bar{\mathcal{O}}}(p)$ otherwise.

3. The CDGS Algorithm

The practical aim of this work is to segment a 3-D numerical image into physically relevant "grains" by using the sign of the lowest principal curvature k_{min} as a criterion. The method can be divided in three main steps: Separating the voxels of $\mathcal{S}$ into two categories, the groove, neck and crater regions, denoted $\mathcal{S}_n$, where $k_{min} \leq 0$ and the granular regions, denoted $\mathcal{S}_p$, where $k_{min} \geq 0$. The second step propagates the created regions on $\mathcal{S}$ deep inside the object by using the Voronoi labeling discussed above to obtain two regions $\mathcal{O}_n$ and $\mathcal{O}_p$ (resp. from seeds $\mathcal{S}_n$ and $\mathcal{S}_p$), with $\mathcal{O} = \mathcal{O}_n \cup \mathcal{O}_p$. The last step consists in labeling the connected spaces belonging to $\mathcal{O}_p$.

Many techniques have been proposed to estimate curvatures on either triangular or digital surfaces [9, 14, 8]. Digital data usually implies specific accuracy issues since estimators are particularly sensitive to noise and digitization effects. This is mainly due to the fact that curvatures are second order estimates obtained on a discrete grid. In our approach, both the mean (C) and Gaussian (G) curvatures are first computed from the largest relevant neighborhood, limiting thus their digitization noise. In our process we distinguish the tools used for the mean and the Gaussian curvature. Indeed, as discussed below, we need a precise mean curvature estimation while only the sign of the Gaussian curvature will be used. In the following, we use a variational approach to define C and G [11]. For short, C can be defined as the divergence of the normal vector map:

$$C(p) = \frac{\text{div}\,\vec{n}(p)}{2}, \quad (3)$$

and the Gaussian curvature as the following PDE:

$$G(p) = \frac{\begin{array}{r}\phi_x^2(\phi_{yy}\phi_{zz} - \phi_{yz}^2) + \phi_y^2(\phi_{xx}\phi_{zz} - \phi_{xz}^2) \\ +\phi_z^2(\phi_{yy}\phi_{xx} - \phi_{xy}^2) \\ +2\phi_x\phi_y(\phi_{xz}\phi_{yz} - \phi_{xy}\phi_{zz}) \\ +2\phi_y\phi_z(\phi_{xy}\phi_{xz} - \phi_{yz}\phi_{xx}) \\ +2\phi_x\phi_z(\phi_{xy}\phi_{yz} - \phi_{xz}\phi_{yy})\end{array}}{(\phi_x^2 + \phi_y^2 + \phi_z^2)^2} \quad (4)$$

with ϕ being the signed distance map DT^* at p and the subscripts x, y, z denoting the partial derivatives along the x, y, z coordinates, respectively. Note that since we are using an exact Euclidean metric for DT^*, ϕ and its derivatives are stable to rotations. Normal vector field $\vec{n}(p)$ could also have been expressed as partial derivative expression on ϕ. However, we use a specific normal vector estimation as proposed in [5]. Such approach is based on an adaptive computation of the normal vector field using volumetric information obtained from DT^*. This gives us a precise estimation of C while decreasing the sensitivity of this formula to digitization effects. For G, we simply use Eq. (4) where derivatives are computed on local neighborhood whose size is obtained by

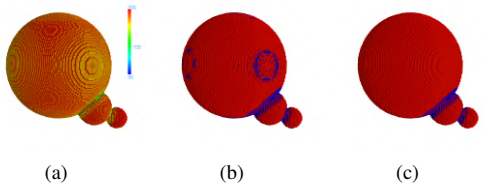

(a) (b) (c)

Figure 1. Initial SLPCM map (a), 0-thresholded SLPCM before (b) and after (c) noise reduction.

the adaptive analysis computed for C. In our segmentation process, we only consider the absolute value of the mean curvature with the sign of the lowest principal curvature, named *Sign of Lowest Principal Curvature Map* (SLPCM) (Fig. 1(a)).

To perform our segmentation, we first threshold the curvature information to identify $\mathcal{S}_n$ and $\mathcal{S}_p$ sets: all curvature values above 0 are considered positive while all values under 0 or equal to 0 are considered negative. A simple interval thresholding is possible to reduce noise in the SLPCM computation (Fig. 1(b)-2(b)). Once the surface segmentation is performed, we need to extrapolate this information to the object's volume. The positive and negative ($\mathcal{S}_p$ and $\mathcal{S}_n$) regions are used as two seeds for the Voronoi labeling algorithm. At the end of this step, $\mathcal{O}$ is segmented in two distinct regions $\mathcal{O}_p$ and $\mathcal{O}_n$ (Fig. 2(c)). After separating the object's volume in two regions, we can remove the voxels of $\mathcal{O}_n$ as in Fig. 2(d). However, this may cause an over-segmentation of the object. To solve this problem, we add balls of positive values at local distance maxima in $DT_{\mathcal{O}}$. The idea of these balls is to insure the connectivity between regions that are related to the same local maxima. The ball's radius R should be large enough to insure reconnection inside a same grain and small enough to prevent reconnection from neighboring grains. In practice, setting R as proportional to the value m (in voxel units) of the local distance maxima $\mathcal{M}$ such that $R = m \times 40\%$ gives pertinent results. Basically, the segmentation results are slightly dependent on this parameter: other values between 30 and 60% are also suitable. Once the image is properly segmented, each connected component can be labeled (Fig. 2(f)). These labels are used as seeds for a new Voronoi labeling. They are thus extrapolated to the whole image and the boundaries of the grains are finally determined (Fig. 2(g)).

4. Validation

In order to validate the CDGS algorithm, the method was applied to two kinds of 3-D images: randomly generated spheres and snow tomographic images (see Fig 3). For the first class of volumes, we have generated five sets of N random discrete spheres, whose radii are uniformly distributed between R_1 and R_2 with centers in $[0, 300]^3$ using a rejection sampling algorithm (acceptance-rejection method): The centers of two spheres can't be separated by an Euclidean distance inferior to the radius of the biggest sphere, and each sphere must be included in the given cubic volume. In Table 1, the exact centers of the randomly-generated spheres are compared to the barycenter of the segmented grains found by the CDGS algorithm. If a sphere is present in the original image but not in the CDGS segmentation, the sphere is considered as an incorrectly segmented grain. If a sphere is segmented in two or more grains, all the concerned grains are considered as incorrectly segmented. For the correctly segmented grains, the average Euclidean distance between the original center of the sphere and the barycenter of the segmented grain is computed. The CDGS algorithm was tested on granular-shaped snow images by using classical tomography, and also DCT. Thanks to a specific acquisition setup, this latter method allows to retrieve the crystalline orientations from diffraction properties of the material (see [10] for a precise description of this experimental method). Such acquisition is technically complex but corresponds to a ground-truth for the proposed segmentation algorithm, which is only based on the material geometry (see Fig 3(d) and 3(e) and Table 1). Both experimental evaluations validate the choices made to set up the segmentation pipeline.

Table 1. Quantitative results for random spheres (a) and snow grains (b).

spheres N	R_1	R_2	# spheres	# grains	# wrong grains	average distance in voxels
100	20	30	500	500	0	1.59
80	25	35	400	400	0	2.23
60	30	40	200	196	8	4.21
40	35	45	100	98	5	4.12
50	20	80	250	248	4	3.42

(a)

# DCT grains	# grains	# wrong grains	average distance in voxels
93	97	4	2.71

(b)

5. Conclusion

We proposed an algorithm that relies on curvature information to detect the grain and boundary regions on the object's surface. This information is propagated to the object's volume by computing discrete Voronoi diagrams, leading, after relabeling, to a realistically-segmented object. This method, which was checked on both simulated and real 3-D data, gives pertinent results and provides new opportunities for the analysis of 3-D structures of well-sintered granular materials. In our context, the Euclidean distance field was used both

(a) (b) (c) (d) (e) (f) (g)

Figure 2. Summary of the segmentation process in 2-D: Initial object (a), thresholded SLPCM (b) with $\mathcal{S}_n$ and $\mathcal{S}_p$ (light and dark blue, respectively), volume extrapolation ($\mathcal{O}_n$ and $\mathcal{O}_p$) after applying the Voronoi algorithm (c), suppression of $\mathcal{O}_n$ (d), adding balls to $\mathcal{O}_p$ at local maxima (e), labeling of each connected component (f), final segmentation (g).

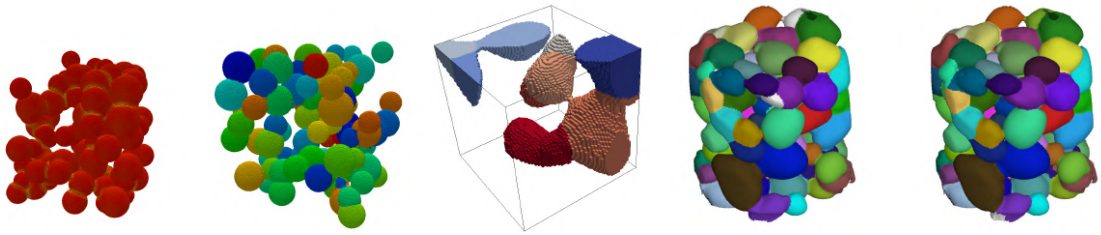

(a) (b) (c) (d) (e)

Figure 3. The CDGS method on sets of random spheres (SLPCM (a) and final result (b)), and on a typical snow image (c). Comparison with ground-truth: DCT (d) and CDGS (e) segmentations.

to efficiently compute surface features (neck detection based on negative curvature) and to propagate these information inside the volume. Such pipeline would make sense in many other applicative area where a volumetric segmentation is required.

References

[1] D. Bernard, D. Gendron, J.-M. Heintz, S. Bordre, and J. Etourneau. First direct 3d visualisation of microstructural evolutions during sintering through x-ray computed microtomography. *Acta Materialia*, 53(1):121 – 128, 2005.

[2] S. C. Colbeck. A review of sintering in seasonal snow. Technical Report 97-10, CRREL, 1997.

[3] M. Couprie, D. Coeurjolly, and R. Zrour. Discrete bisector function and euclidean skeleton in 2D and 3D. *Image and Vision Computing*, 10:1519–1698, 2007.

[4] T. Dey, J. Giesen, and S. Goswami. Shape segmentation and matching with flow discretization. In *Algorithms and Data Structures*, pages 25–36. Springer LNCS, 2003.

[5] F. Flin, J.-B. Brzoska, D. Coeurjolly, R. A. Pieritz, B. Lesaffre, C. Coléou, P. Lamboley, O. Teytaud, G. L. Vignoles, and J.-F. Delesse. Adaptive estimation of normals and surface area for discrete 3-D objects: application to snow binary data from X-ray tomography. *IEEE Trans. Image Process.*, 14(5):585–596, May 2005.

[6] R. M. German. *Sintering theory and practice*. J. Wiley and sons, New York, 1996.

[7] T. Hirata. A unified linear-time algorithm for computing distance maps. *Information Processing Letters*, 58(3):129–133, May 1996.

[8] H. Pottmann, J. Wallner, Q.-X. Huang, and Y.-L. Yang. Integral invariants for robust geometry processing. *Computer Aided Geometric Design*, 26(1):37–60, 2009.

[9] B. Rieger, F. J. Timmermans, and L. J. van Vliet. Estimation of curvature on surfaces in 3d grey-value images. In *Proc ASCI 2002, 8th annual conf. of the advanced school for computing and imaging*, pages 170–177, 2002.

[10] S. Rolland du Roscoat, A. King, A. Philip, P. Reischig, W. Ludwig, F. Flin, and J. Meyssonnier. Analysis of snow microstructure by means of X-ray diffraction contrast tomography. *Adv. Eng. Mater.*, 13(3):128–135, 2011.

[11] J. A. Sethian. *Level set methods and fast marching methods*. Cambridge University Press, Cambridge, 1999.

[12] P. Soille. *Morphological Image Analysis*. Springer-Verlag, Berlin, Heidelberg, New York, Etats-unis, 1999.

[13] S. Svensson and G. S. di Baja. Using distance transforms to decompose 3d discrete objects. *Image Vision Comput.*, 20(8):529–540, 2002.

[14] Y. Zhang, J. Paik, A. Koschan, and M. Abidi. A simple and efficient algorithm for part decomposition of 3-D triangulated models based on curvature analysis. In K. M. Morton and M. J. Baines, editors, *Proc. Int. Conf. Im. Processing, vol III*, pages 273–276, 2002. Rochester, NY, September 2002.

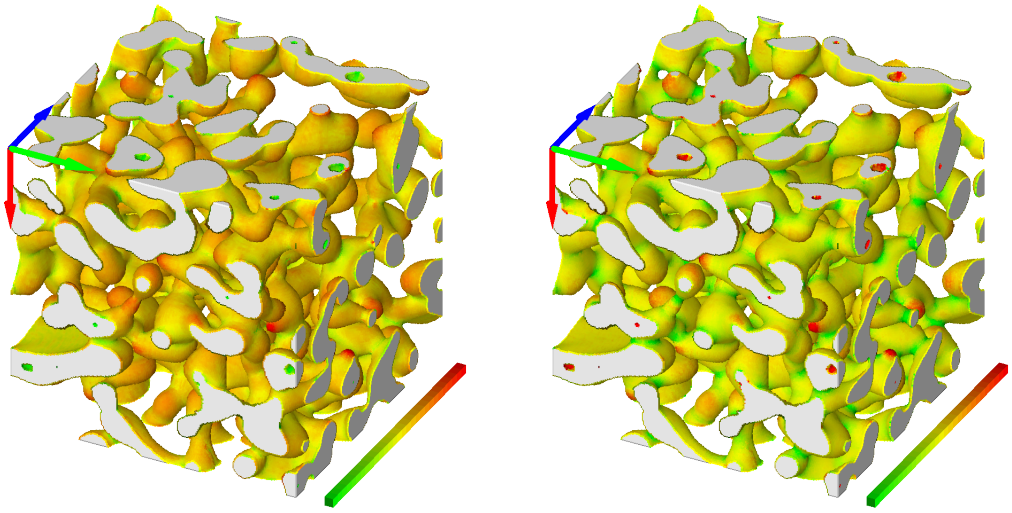

(a) (b)

Figure 3.2 – 3D visualization of a microtomographic image where colors represent the mean curvature in (a) and the Gaussian curvature in (b). Convex, flat or concave surfaces are shown in red, yellow and green, respectively. Images have a size of $2.5 \times 2.5 \times 2.5$ mm^3.

3.3 Conclusion of chapter

In this chapter, we presented a segmentation method using the curvature map of the surface to decompose the sample into grains. This method consists in the main following steps (see Fig. 2 of the paper):

— A signed lowest principal curvature map (SLPCM) is calculated on the object's surface;

— A threshold is used to determine the positive (no concavities) and negative regions (presence of concavities along a particular direction) according to the different types of snow shapes;

— The Voronoi algorithm helps to extrapolate this information into the whole volume. The object is thus classified into "convex" and "concave" volumic regions. Then, only "convex" regions are considered for further processing;

— Balls are added at the local maxima to avoid artificial over-segmentations;

— Each connected component is labeled and propagated to the entire object to

obtain the final segmentation.

Pertinent results are provided by this method. It can be used for most types of snow samples and is particularly appropriate to recognize boundaries between crystalline grains (fine detection of the contact angle). However, this method is highly sensitive to the surface shape of the object: the noise or the irregular parts on the surface may influence the segmentation result. The ball addition at local maxima may also produce some artefacts on the segmentation (under or over-segmentation at the rough interface between grains). In the following, we present a method which is based on a volumetric approach and is less sensitive to surface and propagation artefacts.

Chapter 4

Article: Digital Flow for Shape Decomposition: Application to 3-D Microtomographic Images of Snow

Contents

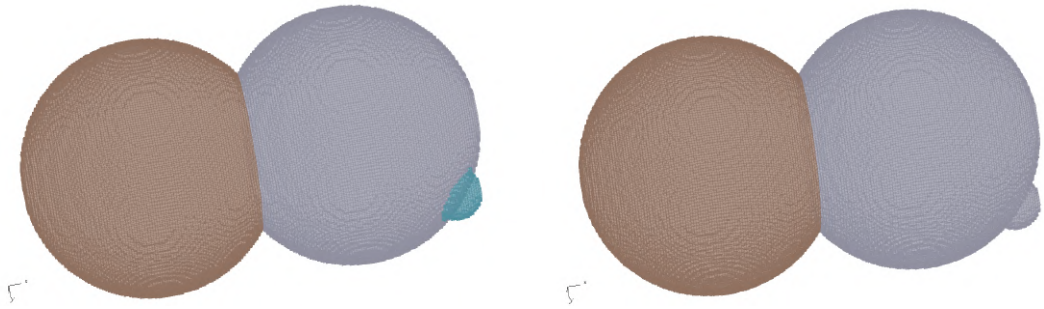

(a) (b)

Figure 4.1 – Shape decomposition in presence of surface noise with method CDGS (a) and MADF (b).

4.1 Context

A more stable and robust approach for separating the snow grains is required. It could be challenging for the method which uses curvature estimators because the computation of curvature values closely depends on the information of object surface. The noise on the surface or irregular interface on the object's surface usually result in an over-segmentation (see Fig. 4.1-(a) and Fig. 4.2-(a)).

In order to reduce the influence of initial noise on segmentation, a mathematical tool, which is based on medial axis of object from a continuous flow, is proposed. It works considering the whole object and not only the surface. This global concept is less sensitive to the noise and irregular cases on the surface (see Fig. 4.1-(b) and Fig. 4.2-(b)). We apply this tool from continuous to digital domain to decompose the shape into meaningful components, i.e. "grain" for snow application.

This chapter corresponds to an article submitted to Pattern Recognition Letters.

4.2 Article: shape decomposition for snow grains

Pattern Recognition Letters
journal homepage: www.elsevier.com

Digital Flow for Shape Decomposition: Application to 3-D Microtomographic Images of Snow

Xi Wang[a,b,c,3,**], David Coeurjolly[a], Frédéric Flin[b]

[a]*CNRS - LIRIS, UMR5205, F-69622, France*
[b]*Météo-France - CNRS, CNRM - GAME, UMR 3589, CEN, F-38400, France*
[c]*Université Paul Sabatier, Toulouse, F-31062, France*

ARTICLE INFO

Article history:

Medial Axis, Digital Flow, Shape decomposition, Snow Microstructure

ABSTRACT

We propose a fast shape decomposition method for granular microstructures using a 3-D approach based on medial axis. We define a two-step algorithm: the first step relies on a notion of digital flow to obtain a preliminary over-decomposition from medial balls. During a second step, we use geometric criteria to obtain a relevant and precise volumetric decomposition. We apply our algorithm to 3-D objects of materials and, more precisely, to microtomographic images of snow microstructures.

1. Introduction

Shape decomposition is one of the fundamental techniques in computer graphics and is widely used in shape processing. The goal of decomposition, sometimes called *segmentation*, is to simplify and/or change the representation of an object in order to make it more meaningful and easy to analyze (Shapiro and Stockman, 2001). The principal contribution of this paper focuses on a fast and efficient shape decomposition method which is based on the digital flow. The concept of flow was introduced in Dey et al. (2003). With the proposition of a fast computation of critical points in digital domain, we obtain a framework of method which is optimal in time. Moreover, we provide two distinct geometrical criteria to control the quality of the decomposition.

In this paper, we first propose a digital version of the flow notion from computational geometry to yield a fast initial decomposition of 3-D granular materials into regions (Sect. 4). This approach provides a structure on the initial regions which allows us to define a simple filtering algorithm to correct over-decomposition effects (Sect. 5). We validate the quality of the decomposition on both synthetic data and images of granular snow samples (Sect. 6).

2. Related works

The main context of this paper is the analysis of granular materials from 3-D computed tomographic images. More precisely, we focus on a specific granular material, i.e. *deposited snow on the ground* (see Fig. 9), which is observed at the scale of its *microstructure* (1 voxel ~ 5-20 µm). In this context, micro-scale modelling requires a precise 3-D description of snow microstructures in terms of individual grains and bond's characteristics (Brzoska et al., 2007). Practically, there are various shape types of snow present in the snowpack, like *Precipitation Particles* (PP), *Rounded Grains* (RG), *Melt Forms* (MF) and so on (Fierz, 2009). Each class implies different geometry of grains from nearly spherical objects to facetted ones. So the challenge is to decompose the 3-D images of these different snow types into grains, which are usually sintered together and form complex shapes. Another specific aspect of our context is that physical analysis of snow micro-structures leads to further requirements on the grain-to-grain interfaces: the interface between two grains should be flat or with minimal curvature values. We do not use such an information directly in our

**Corresponding author.
e-mail: xi.wang@meteo.fr (Xi Wang),
david.coeurjolly@liris.cnrs.fr (David Coeurjolly),
frederic.flin@meteo.fr (Frédéric Flin)
[3]Permanent address: xiwang.it@gmail.com
[4]CNRM-GAME/CEN is part of Labex OSUG@2020 (ANR10 LABX56).

segmentation approach but we rely on it in our experimental evaluation.

From image processing, several approaches for shape decomposition problems consider mathematical morphology tools such as watershed transform (Digabel and Lantuejoul, 1978) or region growing operators (Serra, 1983). In our context where the input object is a binary volume, the main idea of these approaches is to start from a set of markers defined by local maxima in the distance transform of the input shape (see the works of Soille (1999), and Najman and Talbot (2010) for a survey). Then, a propagation process is used to enlarge catchment basins of each local minimum to define the overall decomposition into non-overlapping regions. Despite several improvements (Faessel and Jeulin, 2010), the main drawback is that such approaches have difficulties to capture the complex shape geometry of snow grains and bonds.

Surface based techniques can also be considered. The main idea is to perform a first decomposition on the 3-D object boundary and to propagate such decomposition to the object's interior to finally obtain the volumetric decomposition. If we suppose that grains are smooth with rounded shapes, differential estimators (mean and Gaussian curvatures) can be used to decompose the surface into components with almost constant curvature values (Zhang et al., 2002). In a previous work (Wang et al., 2012), we have developed such decomposition tools based on surface curvature information. This method identifies groove regions on the surface of object to locate the possible separating boundaries in volume. However, all these techniques are highly sensitive to the initial surface decomposition into groove regions from curvature map. Furthermore, they require stable and robust to noise differential curvature estimators, which could be challenging.

Another approach consists in decomposing the initial shape using volumetric information based on the distance map (Svensson and di Baja, 2002) or the medial axis representation of a shape (Dey et al., 2003). For the first mentioned approach, the idea is close to the watershed approach: we start from local maxima of the distance map and we perform a propagation process to construct the regions. A last step is required to overcome the over-decomposition induced by the first step and uses a heuristic based merging process between adjacent regions. Similarly to watershed, the method is highly sensitive to the initial local maxima computation and the region interface quality is poor. From computational geometry, Dey et al. (2003) proposed an interesting mathematical tool which constructs a continuous flow from the medial axis representation of a shape. In this approach, the object is represented by point sets on its boundary and the medial axis is defined as a subset of the Voronoi diagram of the input point set (de Berg et al., 2008). Another method which is based on curve skeletons was proposed by Reniers and Telea (2008a,b). The curve-skeleton junctions which signal the interpenetration of parts are detected based on the junction rule using a function based geodesic metric to quantify the relevance of a given curve-skeleton branch. These approaches provide very good results on 3-D models and CAD shapes. However, when applying them to large micro-tomographic images of snow microstructures (high resolution objects, high topology genus, noisy curve-skeleton with small shortest loops associated to surface), these approaches become time consuming and may lead to inconsistent decomposition.

We propose here a purely volumetric approach which does not require to back-project volumetric information (curve-skeleton or medial structures) to the object surface to compute geometrical information. Our proposal is thus based on simple digital volumetric data structures (digital power map and digital flow) which can be obtained by very fast algorithms.

3. Preliminaries

In this section, we outline the notion of *Flow* induced by a shape (Dey et al., 2003). The original *Flow* definition is described here in a more general setting by considering general shapes which are embedded in d-dimensional Euclidean space $\mathbb{R}^d$.

3.1. Flow in continuous space

In the following, $\mathcal{X}$ denotes a compact subset of d-dimensional Euclidean space $\mathbb{R}^d$, $\partial\mathcal{X}$ denotes its boundary. The definitions can be found in (Dey et al., 2003). Given $\mathcal{X} \subset \mathbb{R}^d$, the *distance transform* $h : \mathbb{R}^d \to \mathbb{R}$ is defined at each point $x \in \mathbb{R}^d$ such that

$$h(x) = inf_{y\in\partial\mathcal{X}} \parallel y - x \parallel^2 \tag{1}$$

Definition 1 (Anchor set). For all $x \in \mathbb{R}^d$, the anchor set $A(x)$ of x is given by

$$A(x) = argmin_{y\in\partial\mathcal{X}} \parallel y - x \parallel^2 \tag{2}$$

In other words, $A(x)$ is the set of the closest points to x in $\partial\mathcal{X}$. Let $conv(A(x))$ be the convex hull of $A(x)$. In Fig. 1, we illustrate, in dimension 2, several configurations where $conv(A(x))$ is a triangle or an edge.

Definition 2 (Critical and Regular points). A point $x \in \mathbb{R}^d$ is a *critical point* if $x \in conv(A(x))$. Otherwise, x is regular.

The flow is defined by using the direction of steepest ascent. First, we set $d(x)$ as driver of x, where $d(x) = argmin_{y\in conv(A(x))} \parallel y - x \parallel^2 \ \forall x \in \mathbb{R}^d$. We then define a vector $v : \mathbb{R}^d \to \mathbb{R}^d$, $v(x) = \frac{x-d(x)}{\|x-d(x)\|}$ if $x \neq d(x)$ and 0 otherwise.

Definition 3 (Induced Flow). The flow is a function $\phi : [0,\infty) \times \mathbb{R}^d \to \mathbb{R}^d$, the right derivative of which satisfies, at each point $x \in \mathbb{R}^d$

$$\lim_{t\downarrow t_0} \frac{\phi(t,x) - \phi(t_0,x)}{t - t_0} = v(\phi(t_0,x)) \tag{3}$$

Definition 4 (Stable manifold). The stable manifold $S(x)$ of a critical point x is the set of all the points which flow into x.

$$S(x) = \{y \in \mathbb{R}^d : \lim_{t\to\infty} \phi(t,y) = x\} \tag{4}$$

The stable manifolds of all critical points induce a decomposition of the object into disjoint regions (the word *stable* thus refers to locii where the flow gradient is null). It means, $\mathbb{R}^d = \bigcup_x S(x)$ for all critical points x. Furthermore, the decomposition is valid since for any two critical points x and y ($x \neq y$), we have $S(x) \cap S(y) = \emptyset$.

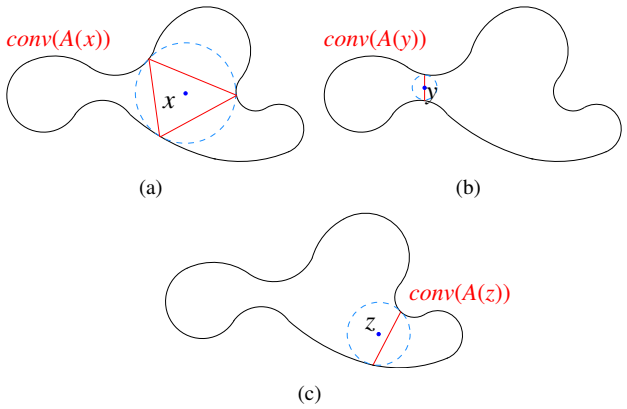

Fig. 1. Several configurations to illustrate critical points definition: In (a), x is such that $x \in conv(A(x))$ (triangle in red) and is thus a critical point. In (b), y lies in the segment $conv(A(y))$, y is a regular point too. In (c), $z \notin conv(A(z))$, so z is a regular point.

3.2. Medial Axis and Digital Medial Axis

The Medial Axis of a shape is a classic method for shape analysis. It was first proposed by Blum (1967) in the continuous plane and can be defined as the set of balls contained in $\mathcal{X}$ touching at least twice $\partial\mathcal{X}$. Following previous definitions, a ball with center $x \in \mathcal{X}$ and radius r belongs to the medial axis if and only if $|A(x)| \geq 2$ and $\|y - x\| = r$ for any point $y \in A(x)$.

When dealing with digital objects ($X \subset \mathbb{Z}^d$), an alternative definition has been proposed in the digital framework (Pfaltz and Rosenfeld, 1967) using a notion of maximal ball:

Definition 5 (Digital Medial Axis). The *Digital Medial Axis* (MA for short) is defined as the set of maximal balls of X: a ball $B \subset X$ is maximal in X if there is no ball $B' \subset X$ such that $B \subset B'$.

$B(c, r)$ denotes an Euclidean open ball with center $c \in X$ and radius r.

From these definitions, many algorithms have been proposed to extract such medial axis structure (Rosenfeld and Pfaltz, 1966; Borgefors, 1986; Remy and Thiel, 2002; Ragnemalm, 1993; Saito and Toriwaki, 1994; Remy and Thiel, 2005; Hesselink et al., 2005; Coeurjolly and Montanvert, 2007). In the following, we focus on the method of Coeurjolly and Montanvert (2007) which extracts the discrete medial axis of a shape $X \subset [1 \dots n]^3$ in $O(n^3)$ optimal time.

4. Digital Flow and Flow based decomposition

Dey et al. (2003) use the stable manifolds to decompose a shape represented by a point cloud sampling its surface. First, the authors construct the Delaunay triangulation of input points (de Berg et al., 2008). Delaunay triangulation is the dual structure of the Voronoi diagram. Both structures are cellular structures in the sense that they are defined as union of open $i-$facets with dimensions 0 to d. For instance, Delaunay triangulation in dimension 2 is made of triangles (2−facets), edges (1−facets) and vertices (0−facets). Voronoi diagram and its dual are meaningful in the flow context since the authors proved that:

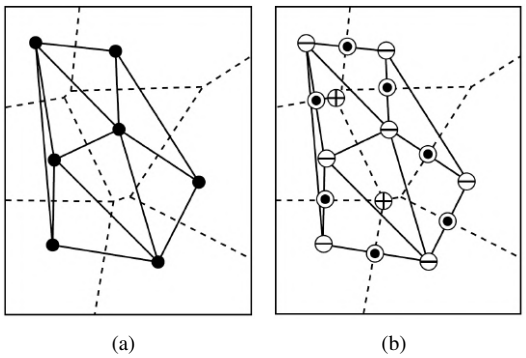

Fig. 2. Voronoi diagram (dashed lines) and Delaunay triangulation (solid lines) of the points in $\mathbb{R}^2$ (a). The critical points (maxima ⊕, saddle point ⊙, minima ⊖) of the distance function induced by these seven points (b). (presented in Dey et al. (2003)).

Lemma 1 (Dey et al. (2003)). *Given a set of points $\mathcal{P}$ in $\mathbb{R}^d$ sampling the boundary of a shape $\mathcal{X}$. Then, critical points for the flow induced by $\mathcal{P}$ are the Voronoi $i-$facets inside $\mathcal{X}$ intersecting their dual Delaunay $(d-i)$-facet.*

In other words, to decide if a Voronoi vertex x is a critical point, we have to check if x is inside the Delaunay triangle which is the dual of x (see Fig. 2). Using such result, Dey *et al* approximate stable manifolds as connected sets of Delaunay $i-$facets. Furthermore, they proposed an algorithm to decompose an object defined by points on its boundary into regions, each region being a stable manifold or a union of stable manifolds. Indeed, they define a simple process to decide if two adjacent stable manifolds can be merged: along the interface between the two stable manifolds, the maximal distance function value h_{max} is computed. Then, the two regions are merged if the ratio between h_{max} and the distance function of each manifold critical point is below a given threshold. We will discuss about this heuristic in Sect. 5.2.

When considering a digital object X in dimension 3 and if we suppose that p is defined on a $[1 \dots n]^3$ domain, we could directly use Lemma 1 and thus continuous Voronoi diagram and Delaunay triangulation to extract critical points and thus stable manifolds. However, the overall computational time would be high since the Delaunay triangulation in 3D has a quadratic number, $O(N^2)$, of tetrahedrons if N is the number of the input points. In our case, N can be in $O(n^3)$ since the specific surface area (ratio between the shape surface area and the volume) can be high. For instance, the shape in Fig. 9-(b) defined in volume with size 256^3 has 1144238 surface elements. Computing the complete Delaunay triangulation would be intractable for larger images.

We propose here a fast computation of critical points using tools working on the digital domain. More precisely, we describe an optimal in time $O(n^3)$ algorithm to extract digital critical points and digital stable manifolds. First of all, let us define an additional structure from computational geometry, the Power Diagram. Let us consider a set of N balls S defined by centers $\{c_i\}_{i=1\dots N}$ and radii $\{r_i\}_{i=1\dots N}$. The power distance $\pi_i(x)$ of a point $x \in \mathbb{R}^d$ to the ball (c_i, r_i) is defined by

$$\pi_i(x) = \|x - c_i\|^2 - r_i^2. \quad (5)$$

Hence, $\pi_i(x) < 0$ (resp. $\pi_i(x) > 0$) if x belongs (resp. is outside) to the ball (c_i, r_i). The power diagram is a decomposition of the space into cells $Pow(\{c_i\},\{r_i\}) = \{\sigma_i\}_{i=1\ldots N}$ such that $\sigma_i = \{x \in \mathbb{R}^d : \pi_i(x) \leq \pi_j(x), \forall j \neq i\}$. In other words, the Power Diagram is a Voronoi Diagram in which the Euclidean metric has been changed to a weighted additive one.

In digital geometry, algorithms exist to compute Voronoi (Couprie et al., 2007; Hesselink, 2007) and Power mappings (Coeurjolly and Montanvert, 2007). Such mappings differ from their respective diagram in the sense that the output is not a combinatorial structure but the intersection between the diagram and the grid. For instance, in addition to the discrete medial axis extraction, an algorithm proposed by Coeurjolly and Montanvert (2007) also computes the digital Power map $\Pi_X : X \to \{1,\ldots,N\}$ such that $\Pi_X = Pow(\{c_i\},\{r_i\}) \cap \mathbb{Z}^3 \cap X$ from medial balls $(\{c_i\},\{r_i\})$ in $O(n^3)$ optimal time. Hence, to each point $p \in X$, $\Pi_X(p)$ is the label of the power cell σ_i such that $p \in \sigma_i$ (if p belongs to power cell boundary, *i.e.* p is equidistant, for the power metric, to two balls, we only return one of the adjacent power cells).

The algorithm described by Coeurjolly and Montanvert (2007) is perfectly suited for processing large digital objects since it is based on simple 1D raster scans in the volume (each voxel is visited a constant number of times), which can be performed independently. Hence, such a technique allows us to design efficient multi-thread implementations to handle very large objects (an implementation is available in the `DGtal` library (Coeurjolly et al., 2009)).

To define digital critical points we use the following lemma which connects Power Diagram and Delaunay triangulation in computational geometry.

Lemma 2 (Amenta et al. (2001))**.** *Let $\mathcal{P}$ be a set of points in general position in $\mathbb{R}^3$. Let $\mathcal{B}$ be the set of balls defined on Voronoi vertices of $\mathcal{P}$. The power diagram of $\mathcal{B}$ is the Delaunay triangulation of $\mathcal{P}$.*

Hence, instead of checking if a given Voronoi vertex v belongs to its dual Delaunay triangle in Lemma 1, it is equivalent to check if v belongs to its power diagram cell. We can now give our definition of digital critical points.

Definition 6 (Digital Critical Point). Let $X \subset [1\ldots n]^3$ be a digital object and let $MA(X)$ be its digital medial axis and Π_X the digital power map of balls in $MA(X)$. Let c_i be a medial ball center, c_i is a *digital critical point* if $\Pi_X(c_i) = i$.

In other words, c_i is critical if $c_i \in \sigma_i$ in the digital domain (see Fig. 3).

In this digital setting, stable manifolds become union of power diagram cells. Let us first define the assignment of regular points to critical ones in a recursive way: let c_j be regular and let c_i be the medial ball center such that $\Pi_X(c_j) = i$, if c_i is critical, we set $l(c_i) = i$, we attach σ_j to σ_i using a label function $l(c_j) = i$. If c_i is not critical, we set $l(c_j) = l(c_i)$. Even if sequences of regular points may appear when attaching a regular point to a critical one, such recursive definition makes sense only if there is no cycle of regular points in the label assignment. We never observe such cycles in our objects but if detected, a simple heuristic can be used to break it: we compute the minimum power distance between each regular point in the cycle and all critical balls. Then, if the minimum distance is given by the regular point c_j and critical point c_i, we force the assignment $l(c_j) = \Pi_X(c_i)$, breaking the cycle.

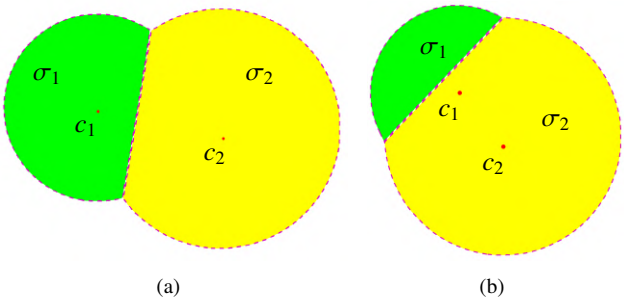

Fig. 3. The definition of digital critical points: c_1, c_2 are the center points of balls and σ_1, σ_2 are their respective power cells. In (a), $c_1 \in \sigma_1$ and $c_2 \in \sigma_2$, c_1 and c_2 are both critical points. In (b), $c_2 \in \sigma_2$, c_2 is a critical point; however $c_1 \in \sigma_2$ too, so c_1 is a regular point.

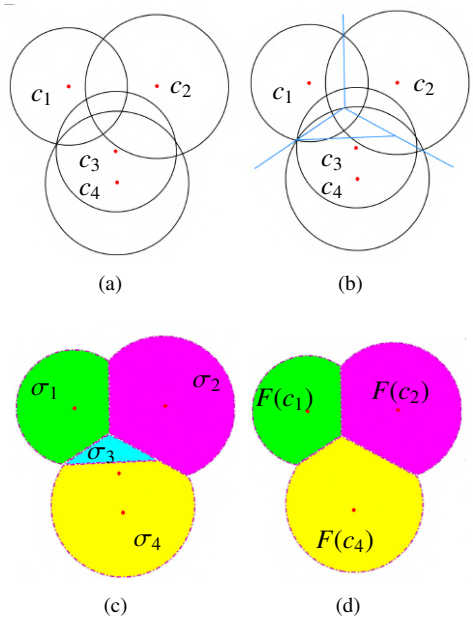

Fig. 4. Digital stable manifold construction: (a) input set of medial balls with centers c_1, c_2, c_3 and c_4, (b) and (c) depict the corresponding power diagram and their associated cells σ_1, σ_2, σ_3 and σ_4. $c_3 \notin \sigma_3$, being regular, we have $l(c_1) = 1$, $l(c_2) = 2$, $l(c_3) = 4$, and $l(c_4) = 4$. (d) illustrates the associated stable manifolds.

Definition 7 (Digital Stable Manifolds). Let c_i be a critical point, the *digital stable manifold* of c_i, denoted $F(c_i)$ is given by

$$F(c_i) = \{p \in X \,|\, \Pi_X(p) = j \text{ and } l(c_j) = i\} \tag{6}$$

The construction of the digital stable manifold is depicted in Fig. 4.

5. Main Algorithm

The overall algorithm can be described as follows: starting from a binary object X, we first compute its medial axis $MA(X)$ and power map Π_X using the method of Coeurjolly and Montanvert (2007) (see Fig. 5). Then we use Def. 6 to detect critical points in $MA(X)$. At this step, digital stable manifolds (Def. 7) give us a first decomposition of X which is consistent with the distance flow induced by X (see for example Fig. 7-(a)). At this point, the overall decomposition is consistent in the sense that it is volumetric, the union of all regions covers the input shape and all regions are disjoint.

However, an over-decomposition, i.e. a decomposition which segments a shape unnecessarily into very small features is generally obtained at this stage. It is thus important to merge all mergeable stable manifolds together. This step is ensured by filtering the medial axis (condition on the balls' size - Sect. 5.1) and by using a simple geometrical criterion based on ball intersection geometry (Sect. 5.2).

5.1. Pre-processing

When dealing with noisy data, the small perturbations change the medial axis of a shape and then lead to many small balls on the boundary or near sharp features (see Fig. 5-(b)) which are not desirable. In many cases, MA based algorithms have to filter the output to only keep relevant MA balls. A large literature with many approaches exist on this subject (Borgefors, 1986; Attali and Montanvert, 1997; Amenta et al., 2001; Chazal and Lieutier, 2005; Reniers and Telea, 2008a; Giesen et al., 2009).

In the following, we consider a filtering we proposed in Coeurjolly and Montanvert (2007). The main reason is that this filtering process is defined on the Power Map of the digital medial axis and is well suited to our process. More precisely, the filtering first computes the area of each power map cell. Such information is used to evaluate the relevance of a ball since power cell with small area means that either the ball is small, or the ball is locally surrounded by larger ones. In the following we can just filter the input medial axis using a threshold γ on the power cell area.

Beside its simplicity with respect to some other metrics on local scale relevance of medial balls, such approach leads to a very efficient pre-processing. In fact, this pre-processing is just used to remove some spurious balls in the medial axis induced by small noise on the object surface. The overall segmentation is driven by both critical balls and the merging process as described below, the impact of the ball filtering technique on the results being actually very limited.

5.2. Merging using geometric angle

When considering complex geometrical shapes, stable manifolds usually lead to an over-decomposition of the object (see Fig. 7-(a)). We describe here a simple geometric parameter to decide whether two adjacent stable manifolds should be merged.

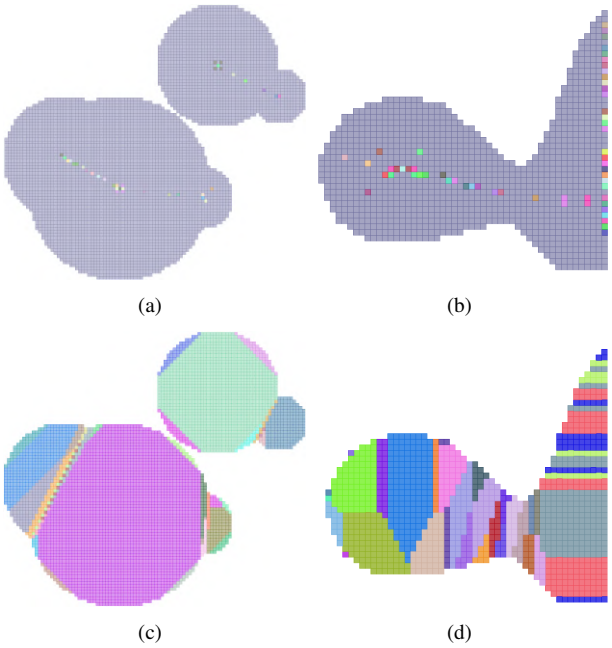

Fig. 5. Digital Medial Axis and Power Map in dimension 2: (a) **and** (b) **discrete medial axes given by the ball centers,** (c) **and** (d) **the corresponding power maps.**

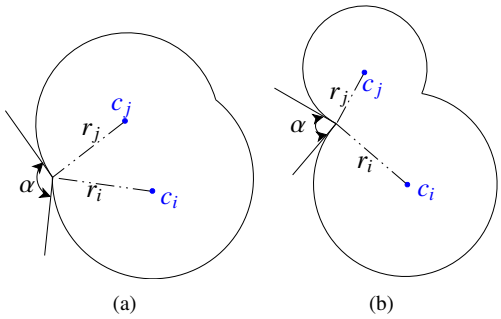

Fig. 6. α **angles for two given configurations of spheres.**

Let us consider two critical points c_i, c_j (with radii r_i and r_j) with adjacent power cells in Π_X (we use 6 neighborhood in applying to 3-D images). We consider the angle α such that

$$cos(\alpha) = \frac{\|c_i - c_j\|^2 - r_i^2 - r_j^2}{2 \cdot r_i \cdot r_j} \tag{7}$$

Fig. 6 illustrates angles α for two given circles in dimension 2. Similarly, in dimension 3, α corresponds to the angle between tangent vectors of each ball at the intersection between two balls. In the following, we use this quantity to design a simple local criterion: given a threshold $\theta \in [-1, 1]$, if $cos(\alpha) < \theta$ for any two adjacent critical balls, we reassign one of the critical point label. For instance, we set $l(c_i) = j$ (choice between c_i or c_j in the reassignment has no influence on the result). Using different values of θ, we can obtain different decomposition results as shown in Fig. 7. In practice, the choice of such a value depends on the requirements of applications. In our context, θ was normally chosen from -0.6 to -0.8, considering the structure of grains in different snow types.

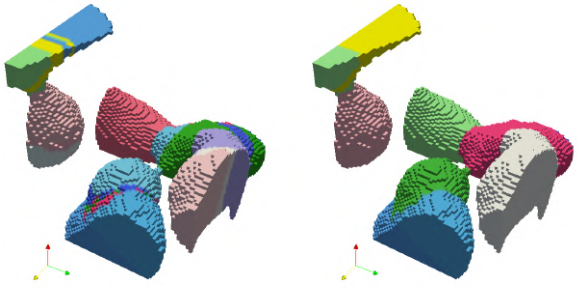

(a) Initial stable manifolds (b) $\theta = -0.9$

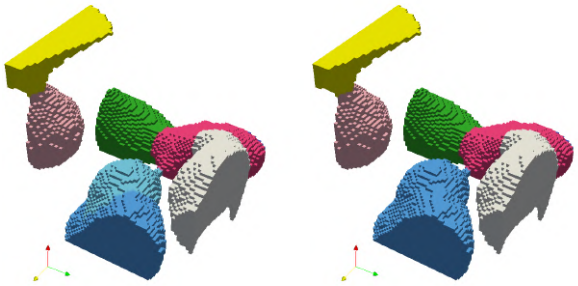

(c) $\theta = -0.8$ (d) $\theta = -0.7$

Fig. 7. Decomposition results after the merging step for different θ values: (a) initial digital stable manifolds, (b) - (d): several increasing θ values.

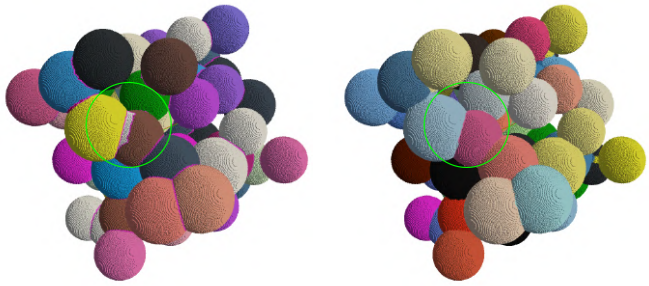

(a) Watershed with distance function (b) CDGS

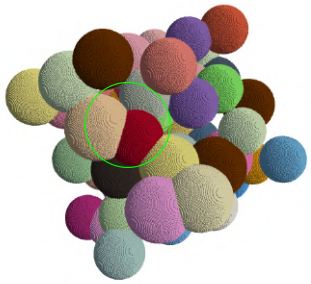

(c) MADF

Fig. 8. Comparison on random sphere sets by watershed with distance function, CDGS and MADF respectively: (a) an over-decomposition is produced by watershed, (b) and (c) illustrate that both CDGS and MADF (with $\gamma = 0, \theta = -1$) work well on sphere sets.

6. Application to 3-D snow images

The proposed algorithm has been implemented using tools available in DGtal library (Coeurjolly et al., 2009) such as linear in time volumetric algorithms (medial axis extraction, power map,..., Coeurjolly and Montanvert, 2007). As mentioned above, if the input 3-D object is defined in a $[1 \dots n]^3$ image, both digital medial axis extraction and power map constructions can be performed in $O(n^3)$ (Coeurjolly and Montanvert, 2007). The pre-processing (if needed) can be done using a linear scan of the power map. The merging step criterion is evaluated on each pair of critical points with adjacent power map cells. A rough upper bound for the computational cost of this step is given by the size of the power map. This upper bound is not tight since the number of critical points is usually much smaller than the size of the input object. For instance, for the MF sample (Fig. 9-(a)) with size 270^3, we have 155281 digital medial balls and 3601 critical points. Finally, the operations on the label function l can be implemented using a Disjoint-Set (or Union-Find) data-structure which allows us to have all these operations in amortized quasi-constant time. Hence, the overall computational cost of the segmentation algorithm is linear in the size of the input volume.

The proposed algorithm (MADF for short) has been experimented on 3-D images and compared to other decomposition approaches such as watershed with distance function and CDGS (Curvature-Driven Grain Segmentation, Wang et al., 2012) and, when available, to ground truth from physical experiments (DCT, Rolland du Roscoat et al., 2011, see Sect. 6.2). In all cases, the provided outputs are volumetric decomposed objects whose components are labelled by different colors. The methods have been applied on both synthetic data and snow microtomographic images.

6.1. Experimentation on synthetic data

We first consider series of synthetic 3-D images using randomly generated spheres sets in $[0, 300]^3$. The comparison results are presented in Table. 1. For spheres, radii are distributed between R_1 and R_2, N indicates the number of spheres. In order to quantify the difficulty of the decomposition problem, we define the ratio ρ as follows:

$$\rho = \frac{\sum_{i=1}^{n} |B_i| - |X|}{|X|} \tag{8}$$

where $|B_i|$ is the volume of an element in the random spheres set. Hence, high ρ indicates that many geometrical elements overlap and thus the recovering of each of them is more challenging.

For a better validation, we have created five sphere sets. For each test, we count the number of decomposed grains and quantify the percentage of misclassified voxels when a ground-truth decomposition is known (label "i" in the ground-truth image is associated to the label "j" in the test image if most voxels with label "i" are mapped to label "j" in test image). In these sphere tests, the ground-truth decomposition is given by the power map of input spheres. We use thresholds $\gamma = 0$ and $\theta = -1$

Table 1. Quantitative results for random spheres (*a*) and MF sample (*b*) compared among three decomposition approaches: watershed with distance function, CDGS and MADF

N	R_1	R_2	ρ	watershed		CDGS		MADF	
				# grains	% misclass.	# grains	% misclass.	# grains	% misclass.
100	20	30	0.08408	216	0.728596%	100	0.707515%	100	0.302259%
80	25	35	0.14911	252	1.2033%	80	0.765337%	80	0.565739%
60	30	40	0.19667	251	1.88912%	59	1.51798%	59	0.8645%
40	35	45	0.19068	251	1.8194%	39	1.51363%	40	0.775526%
50	20	80	0.24879	252	4.64338%	49	6.11259%	50	3.36936%

(a)

real #grains	watershed		CDGS		MADF	
DCT	# grains	% misclass.	# grains	% misclass.	# grains	% misclass
93	31	17.7403%	80	3.84519%	99	1.83415%

(b)

Table 2. Comparison of the interface geometry for RG and MF sample among three decomposition approaches: watershed with distance function, CDGS and MADF

		watershed		CDGS		MADF	
		average	standard dev.	average	standard dev.	average	standard dev.
MF	Absolute mean curvature	0.055	0.097	0.869	0.221	0.105	0.291
	Absolute Gaussian curvature	0.042	0.313	0.057	0.757	0.027	0.171
	flatness	2.861	6.023	2.094	4.452	0.608	1.815
RG	Absolute mean curvature	0.102	0.152	0.185	1.420	0.186	0.494
	Absolute Gaussian curvature	0.025	0.075	0.974	29.834	0.0845	0.584
	flatness	0.368	0.79	0.541	1.134	0.356	0.616

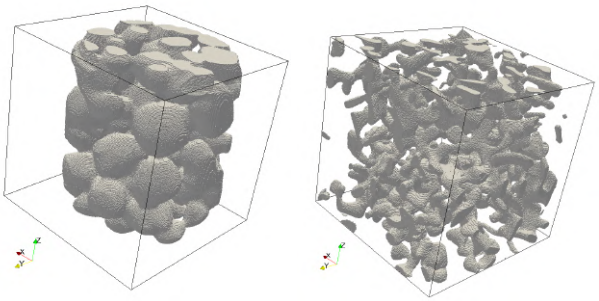

(a) (b)

Fig. 9. 3-D images of snow as obtained by Diffraction Contrast Tomography (*a*) with size 270^3 (MF sample - all labels of physically detected grains have been set to the same value. See Fig. 10-(*a*) for the original DCT image) and X-ray microtomography (*b*) with size 256^3 (RG sample).

for MADF, because these synthetic images are smooth and the critical point of a sphere is exactly its center. No parameter has been used for watershed and among the large set of parameters for CDGS (13 but 4 main parameters), we have performed a manual analysis to select the best ones for the objects. According to the results in Fig. 8 and Table. 1-(*a*), watershed method with distance function usually produces an over-decomposition around the interface between two adjacent spheres. It results in a large number of regions in Table. 1-(*a*). Such over-segmented regions are small or thin since the percentage of misclassified voxels is still low. CDGS and MADF both present good decomposition results on spheres sets in Fig. 8. Considering the number of decomposed grains and percentage of misclassified voxels, MADF has a more precise decomposition than CDGS.

6.2. Decomposition of snow images

We used 3-D images of real snow samples (see Fig. 9) to evaluate the quality of the shape decomposition provided by the proposed algorithm.

Snow images, such as the RG sample of Fig. 9-(*b*), are obtained by X-ray absorption microtomography using the following technique: the snow samples were first filled with liquid 1-chloronaphthalene around -2°C and frozen at -25°C before further machining. Small cores 9 mm in diameter were then extracted with a precision hole-saw, sealed inside sample holders, which were then placed into a specifically designed cryogenic cell for microtomographic acquisition. The obtained gray-level images were contoured using a semi-automatic procedure, leading to binary (air and ice) decomposed 3-D images. Complementary information can be found in previous works of Flin et al. (2003, 2004).

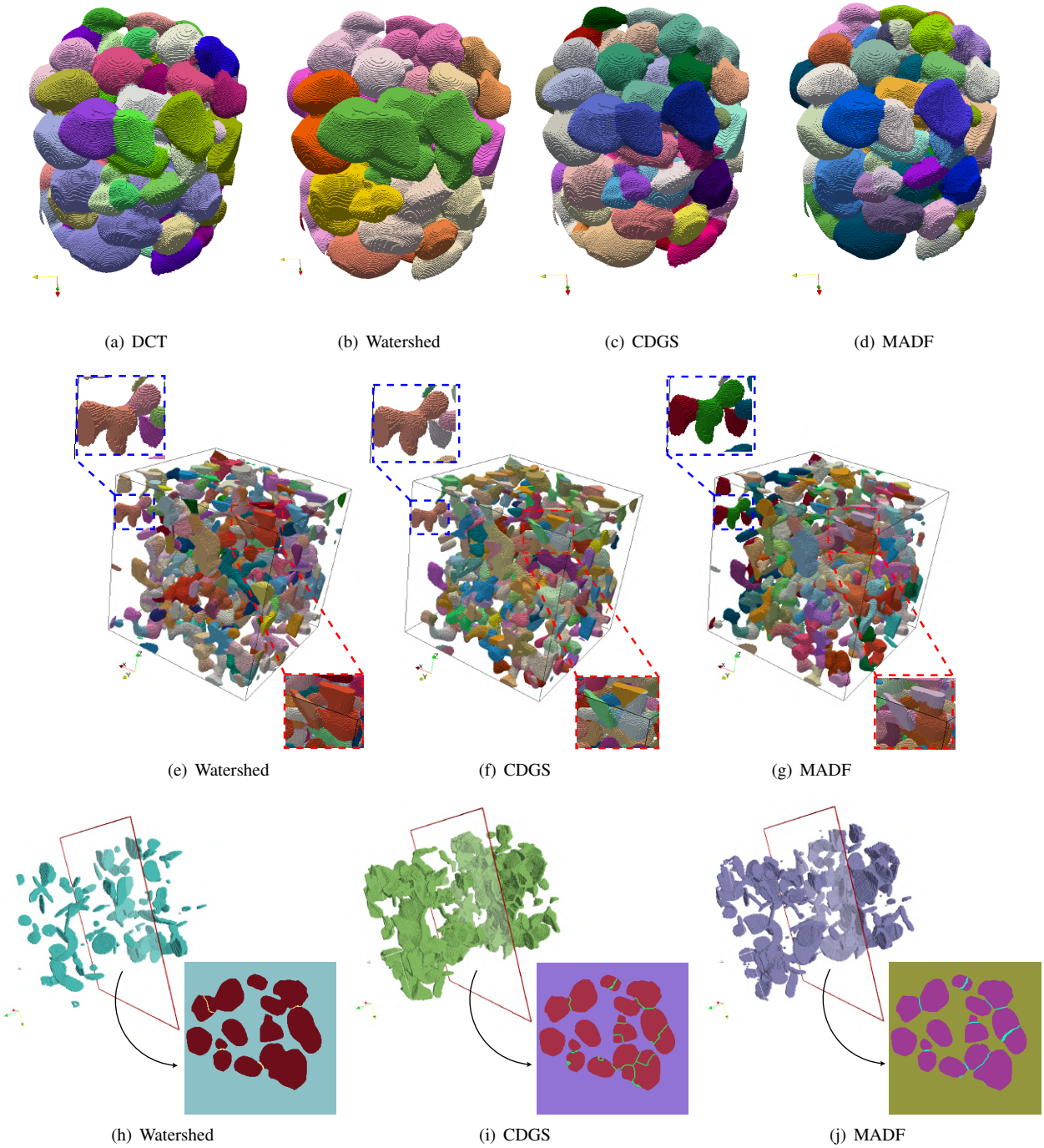

(a) DCT (b) Watershed (c) CDGS (d) MADF

(e) Watershed (f) CDGS (g) MADF

(h) Watershed (i) CDGS (j) MADF

Fig. 10. Comparisons between methods: decomposition of 3-D snow samples MF (*a*) **-** (*d*)**; decomposition on sample RG** (*e*) **-** (*g*)**; grain-to-grain interfaces of MF comparisons** (*h*) **-** (*j*)**.**

In addition to classical absorption tomography, an image was obtained by Diffraction Contrast Tomography (DCT, Ludwig et al., 2009; Rolland du Roscoat et al., 2011), a recent experimental technique that combines X-ray diffraction analyses and absorption tomography to provide simultaneously, (1) the 3-D geometry of the ice-air interface, (2) the 3-D mapping of individual grains in polycrystals, and (3) their crystalline orientation. For some particular snow structures such as that of the MF sample presented in Fig. 10-(*a*), each geometric grain exhibits a particular crystalline orientation so that the DCT can actually provide a physically-based shape decomposition of the granular structure.

For the MF sample (Fig. 9-(*a*)), we chose the values $\gamma = 160$ and $\theta = -0.8$ of MADF to decompose the object. For the RG sample (Fig. 9-(*b*)), the values $\gamma = 20$ and $\theta = -0.5$ were adopted. For the watershed method, no parameter has been in-

Table 3. Timings for the proposed methods in seconds (Intel(R) Xeon(R) CPU 2.67GHz/4 Processors/RAM 7.8G).

Shapes	watershed	CDGS	MADF
MF	416.74	915.44	44 (pre-process time) 10.69 (merging time)
RG	330.732	635.41	40.16 (pre-process time) 7.4 (merging time)

troduced. For CDGS, among the 13 existing parameters, 4 are crucial to control the quality of decomposition. Interfaces are important to perform numerical simulations on snow grains and MADF produces better and smoother grain-to-grain interfaces plans, than CDGS as can be seen from Fig. 10-(h)(i)(j). From the decomposition results in Fig. 10 and Table. 1-(b), we can conclude that a more precise decomposition can be achieved with MADF than with the other two numerical methods.

In Table 2, we have performed a geometrical analysis of the grain-to-grain interfaces. The main idea was to evaluate the quality of the interface in terms of flatness. To do so, we processed all interfaces and we computed several quantities: mean and Gaussian curvatures given by a fitting with high degree polynomial surface of the interface point set (Cazals and Pouget, 2005), and *flatness* information by computing the covariance matrix of the point set and returning the smallest eigenvalues which correspond to the minimal axis length of the ellipsoid approximating the point set. Beside the watershed approach, which produces flat interfaces but with bad segmentation results, we can observe that the MADF approach provides better quality interfaces than CDGS (lower average values and lower standard deviations).

Finally, Table 3 indicates some timings of the proposed approach.

7. Conclusion

In this paper, we proposed a novel framework for shape decomposition based on digital critical points and the digital flow induced by the medial axis of shape. The core of the approach relies on an adaptation of classical flow and critical points definitions from computational geometry to digital settings. Such an adaptation allows us to construct a fast decomposition algorithm which is computationally efficient and provides high quality object decomposition on both synthetic data and real 3-D images.

8. Acknowledgements

The authors thank the scientists of the ESRF ID19 beamline and the members of the Snow-White project (ANR-06-BLAN-0396) for the image acquisition. This work has been mainly funded by the DigitalSnow ANR-11-BS02-009 research grants.

References

Amenta, N., Choi, S., Kolluri, R.K., 2001. The Power Crust, Union of Balls, and the Medial Axis Transform. Submitted to. Computational Geometry: Theory and Applications 19, 127–153.

Attali, D., Montanvert, A., 1997. Computing and simplifying 2d and 3d continuous skeletons. Computer Vision and Image Understanding 67, 261–273.

de Berg, M., Cheong, O., van Kreveld, M., Overmars, M., 2008. Computational Geometry: Algorithms and Applications. Springer-verlag.

Blum, H., 1967. A Transformation for Extracting New Descriptors of Shape, in: Wathen-Dunn, W. (Ed.), Models for the Perception of Speech and Visual Form. MIT Press, pp. 362–380.

Borgefors, G., 1986. Distance transformations in digital images. Computer Vision, Graphics, and Image Processing 34, 344–371.

Brzoska, J., Flin, F., Ogawa, N., 2007. Using gaussian curvature for the 3D segmentation of snow grains from microtomographic data. Physics and chemistry of ice , 125–132.

Cazals, F., Pouget, M., 2005. Estimating differential quantities using polynomial fitting of osculating jets. Computer Aided Geometric Design 22, 121–146.

Chazal, F., Lieutier, A., 2005. The "lambda-medial axis". Graphical Models 67, 304–331.

Coeurjolly, D., Lachaud, J.O., et.al, 2009. Dgtal: Digital geometry tools and algorithms library. URL: `http://libdgtal.org/`.

Coeurjolly, D., Montanvert, A., 2007. Optimal Separable Algorithms to Compute the Reverse Euclidean Distance Transformation and Discrete Medial Axis in Arbitrary Dimension. IEEE Transactions on Pattern Analysis and Machine Intelligence 29, 437–448. doi:10.1109/TPAMI.2007.54.

Couprie, M., Coeurjolly, D., Zrour, R., 2007. Discrete bisector function and euclidean skeleton in 2D and 3D. Image and Vision Computing 25, 1519–1698.

Dey, T., Giesen, J., Goswami, S., 2003. Shape segmentation and matching with flow discretization. Lecture Notes in Computer Science 2748, 2536.

Digabel, H., Lantuejoul, C., 1978. Iterative Algorithms. CGMM, ENSMP.

Faessel, M., Jeulin, D., 2010. Segmentation of 3D microtomographic images of granular materials with the stochastic watershed. Journal of Microscopy 239, 1731.

Fierz, C., 2009. The International Classification for Seasonal Snow on the Ground. IHP-VI Technical Documents in hydrology ; no. 83 ; IACS contribution, UNESCO/IHP.

Flin, F., Brzoska, J.B., Lesaffre, B., Coléou, C., Pieritz, R.A., 2003. Full three-dimensional modelling of curvature-dependent snow metamorphism: first results and comparison with experimental tomographic data. J. Phys. D: Appl. Phys. 36, A49–A54.

Flin, F., Brzoska, J.B., Lesaffre, B., Coléou, C., Pieritz, R.A., 2004. Three-dimensional geometric measurements of snow microstructural evolution under isothermal conditions. Ann. Glaciol. 38, 39–44. doi:10.3189/172756404781814942.

Giesen, J., Miklos, B., Pauly, M., Wormser, C., 2009. The scale axis transform., in: Hershberger, J., Fogel, E. (Eds.), Symposium on Computational Geometry, ACM. pp. 106–115.

Hesselink, W.H., 2007. A linear-time algorithm for euclidean feature transform sets. Information Processing Letters 102, 181–186.

Hesselink, W.H., Visser, M., Roerdink, J.B.T.M., 2005. Euclidean skeletons of 3D data sets in linear time by the integer medial axis transform, in: Ronse, C., Najman, L., Decencière, E. (Eds.), Mathematical Morphology: 40 Years On (Proc. 7th Intern. Symp. on Mathematical Morphology), Springer. pp. 259–268.

Ludwig, W., Reischig, P., King, A., Herbig, M., Lauridsen, E.M., Johnson, G., Marrow, T.J., Buffière, J.Y., 2009. Three-dimensional grain mapping by x-ray diffraction contrast tomography and the use of friedel pairs in diffraction data analysis. Review of Scientific Instruments 80, 033905. doi:10.1063/1.3100200.

Najman, L., Talbot, H., 2010. Mathematical Morphology: From Theory to Applications. ISTE Ltd and John Wiley & Sons Inc.

Pfaltz, J.L., Rosenfeld, A., 1967. Computer representation of planar regions by their skeletons. Commun. ACM 10, 119–122.

Ragnemalm, I., 1993. The Euclidean Distance Transform. Ph.D. thesis. Linköping University, Linköping, Sweden.

Remy, E., Thiel, E., 2002. Medial axis for chamfer distances: computing look-up tables and neighbourhoods in 2D or 3D. Pattern Recognition Letters 23, 649–661.

Remy, E., Thiel, E., 2005. Exact medial axis with euclidean distance. Image and Vision Computing 23, 167–175.

Reniers, D., Telea, A., 2008a. Part-type segmentation of articulated voxel-shapes using the junction rule. Computer Graphics Forum (Proc. Pacific Graphics08) 27, 1845–1852.

Reniers, D., Telea, A., 2008b. Patch-type segmentation of voxel shapes using simplified surface skeletons. Computer Graphics Forum (Proc. Pacific Graphics08) 27, 1837–1844.

Rolland du Roscoat, S., King, A., Philip, A., Reischig, P., Ludwig, W., Flin, F., Meyssonnier, J., 2011. Analysis of snow microstructure by means of x-ray diffraction contrast tomography. Advanced Engineering Materials 13, 128–135. doi:10.1002/adem.201000221.

Rosenfeld, A., Pfaltz, J.L., 1966. Sequential operations in digital picture processing. Journal of the ACM 13, 471–494.

Saito, T., Toriwaki, J.I., 1994. Reverse distance transformation and skeletons based upon the euclidean metric for n-dimensionnal digital pictures. IECE Trans. Inf. & Syst. E77-D, 1005–1016.

Serra, J., 1983. Image Analysis and Mathematical Morphology. Academic Press, Inc.

Shapiro, L., Stockman, G., 2001. Computer Vision. Prentice Hall.

Soille, P., 1999. Morphological Image Analysis. Springer-Verlag, Berlin, Heidelberg, New York, Etats-unis.

Svensson, S., di Baja, G.S., 2002. Using distance transforms to decompose 3D discrete objects. Image Vision Comput. 20, 529–540.

Wang, X., Gillibert, L., Flin, F., Coeurjolly, D., 2012. Curvature-Driven Volumetric Segmentation of Binary Shapes: an Application to Snow Microstructure Analysis, in: International Conference on Pattern Recognition, IEEE Computer Society. pp. 742–745.

Zhang, Y., Paik, J., Koschan, A., Abidi, M.A., Gorsich, D., 2002. A simple and efficient algorithm for part decomposition of 3D triangulated models based on curvature analysis, in: in Proceedings of the International Conference on Image Processing, III, pp. 273–276.

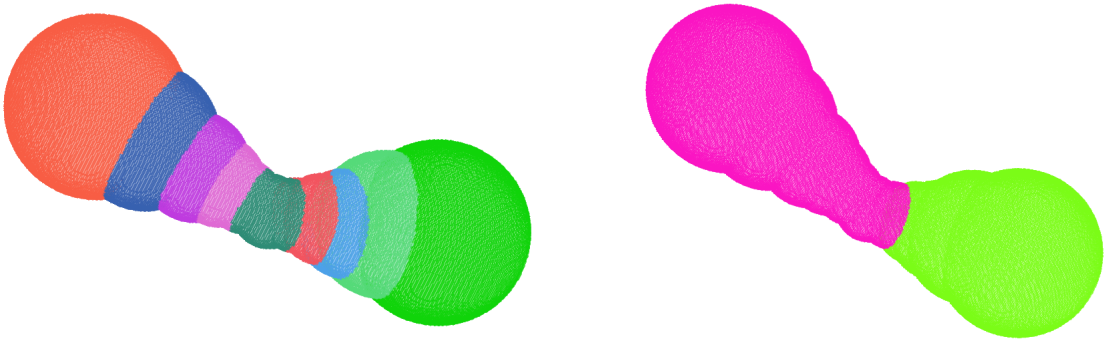

(a) (b)

Figure 4.2 – Shape decomposition on an irregular surface with method CDGS (a) and MADF (b).

4.3 Conclusion of chapter

Considering the high sensitivity to the initial shape surface with CDGS, we developped another segmentation method which uses the entire information of object's structure instead of the surface only. It is based on the digital flow from medial axis of the object. It is efficient, robust and easy to control the decomposition quality with 2 thresholds. The scheme of the main algorithm is summarized in Alg. 4.1.

```
Compute the medial axis MA(X) on object and the power diagram Π_X based
 on MA(X);
Calculate the area of each power cell;
forall power cell do
    if Area < threshold then
        Remove the associated ball from MA(X) and power cell from Π_X;
    end
end
forall medial ball do
    if the center of ball is regular then
        Re-assign the power cell of regular points into associated critical point
         and construct stable manifolds;
    end
end
forall two adjacent stable manifolds do
    if geometric angle between two > threshold then
        Merger them together;
    end
end
```

Algorithme 4.1 : MADF algorithm description.

Chapter 5

Applications of decomposition techniques to 3-D snow images

Contents

5.1 Grain segmentation on snow samples

To validate the segmentation methods which are introduced in Chapter 3 and Chapter 4, we use a series of 3-D snow samples (see Table 5.1). These samples have different types of grain shapes depending on the conditions of their enviroment. I01, I08 and I23 were produced under controlled isothermal conditions in the cold room of CEN [FBL+04]. Two neighboring volumes were obtained under a controlled Temperature Gradient (TG) of 16 K/m: E01 and E02 correspond to the same macroscopic sample as described in [FB08]. Samples P03, P04 and P10 were taken at increasing depths in the natural snowpack of the Girose glacier (Ecrins, French Alps) during a field campaign on the 17th April 2009. Finally, wet grains samples H03 and H05 were obtained by coarsening of water-saturated snow using a similar method that described in [RT79]. After 48 h and 142 h of growth respectively, the samples were drained out from their liquid water, filled with liquid 1-chloronaphtalhene around $-1°$C and frozen at $-25°$C before further machining. The 3-D tomographic images (series I and E) were obtained at ID19 beamline of the European Synchrotron Radiation Facility (ESRF) and the others were acquired with a cone beam tomograph (laboratory 3SR). The decomposition results of these samples by CDGS and MADF are illustrated in Fig. 5.5. In CDGS, we have 4 main parameters to control the quality of decomposition (see Table. 5.2). For the tested snow samples, we set MIL_PROP=30, TYPE_SEUIL=3, SEUIL_FIXE=0, and GRAIN_MIN=400. In MADF, two thresholds (γ and θ) need to be defined. For all the snow samples in Table 5.1, we chose the threshold $\theta = -0.8$, which is decided after a series of experiments under differents types of snow. Considering the sizes of grains in different snow types have large difference, we use equivalent sphere radius of snow [LA02] (also called the optical radius, optical-equivalent grain size or OGS [FAD+09]) to adjust the filter size γ of the algorithm. The equivalent sphere radius is a characteristic length of the ice grains at the microscopic scale, which corresponds to the radius of a monodisperse collection of spheres having the same specific surface area (SSA) value. It is here defined as $r_{es} = \frac{3}{SSA}$, with SSA in vox^{-1}. The threshold was chosen as $\gamma = 0.3 \times r_{es}^2$, where 0.3 was obtained by practice. In Fig. 5.5, we can notice that the methods CDGS and MADF have a good segmentation for the grains whose shapes are not so far from spherical or rounded (RG/FC/DH/MF). For

these particular snow types, MADF generaly provides a more reasonnable result (the comparison is illustraded by the article in Chapter 4). For the other snow types, like PP and DF, the segmentation is not so good because of their very complex structures. We will make our method more robust in the future.

Table 5.1 – List of the various snow samples tested. Snow type is given according to the international classification [FAD+09].

Sample	Voxel size (μm)	Snow type	Remarks	Porosity	Density (kg/m^3)
I01	4.91	PP/DF	Sampled 15 h after the snowfall	0.88	106
I08	4.91	DF	Sampled 470 h after the snowfall	0.83	150
I23	4.91	RG	Sampled 2026 h after the snowfall	0.71	259
E01	4.91	FC/DH	3 weeks with $TG = 16$ K/m downer volume	0.75	225
E02	4.91	FC/DH	3 weeks with $TG = 16$ K/m upper volume	0.71	265
P03	8.48	PP/DF	Field, Girose glacier, 0.2 m depth	0.84	141
P04	8.59	PP/DF	Field, Girose glacier, 0.4 m depth	0.82	161
P10	6.10	RG	Field, Girose glacier, 1.6 m depth	0.56	399
H03	8.61	MF	Grain coarsening of water-saturated snow and drainage after 48 h	0.45	499
H05	8.59	MF	Grain coarsening of water-saturated snow and drainage after 142 h	0.45	497

5.2 Snow geometric analysis

Specific grain contact area (SGCA) is a parameter to describe snow microstructure, e.g. to forecast the SSA that can be released by mechanical processing [VBG+75, FLD+11]. Both SGCA and SSA are important. They are defined in Chapter 2. After grain decomposing, we estimate SSA and SGCA of each snow sample (described in Sec.5.1). In order to calculate them, we have to estimate the surface area for SSA and area of interface for SGCA. For a 3-D digital image, just counting the total number of surface voxels is not accurate. See Fig. 5.6 for an example in 2-D: (a), the perimeter of the square is 20 pixels. After a rotation of 45° in (b), the perimeter is only 12 pixels. To solve this problem, we can use the information contained in the normal field of

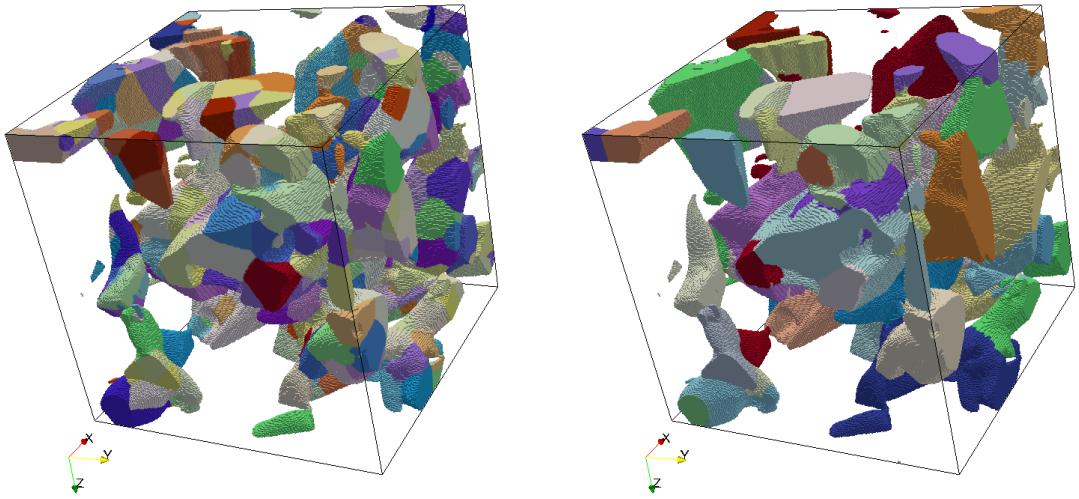

(a) Eo1 - CDGS (b) Eo1 - MADF

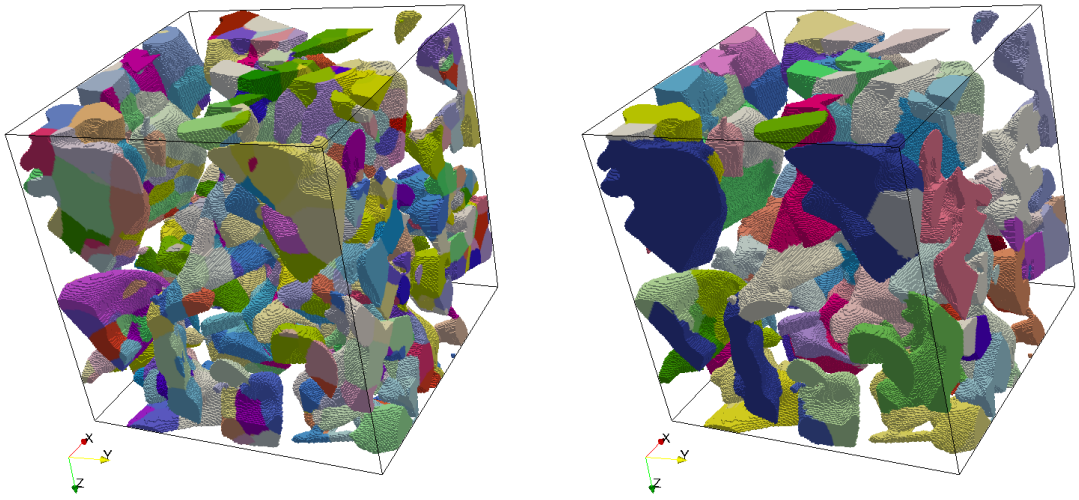

(c) Eo2 - CDGS (d) Eo2 - MADF

Figure 5.1 – Several types of snow samples (here, FC/DH) and the segmentation results using CDGS in left column, and MADF in right column.

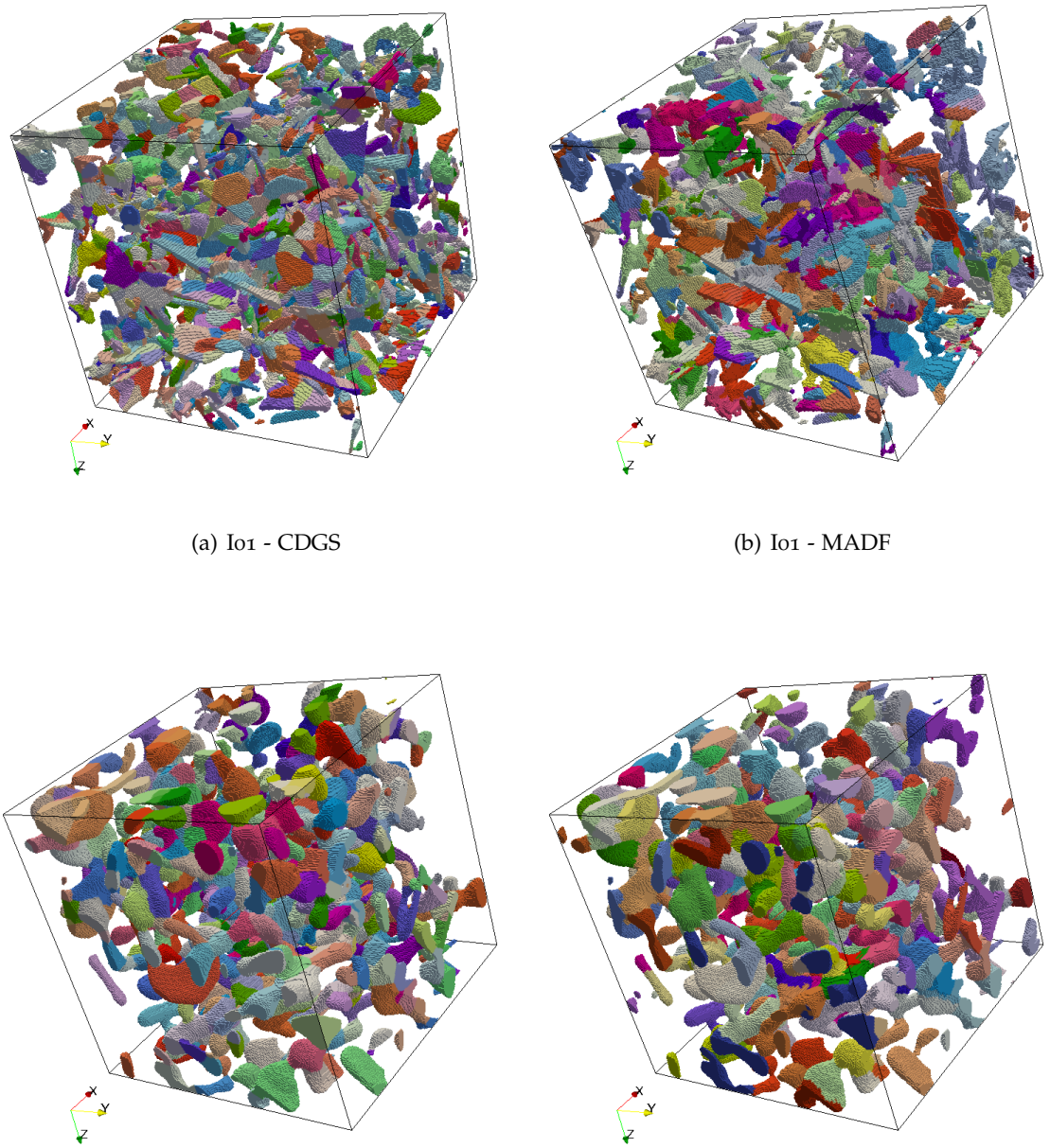

(a) Io1 - CDGS

(b) Io1 - MADF

(c) Io8 - CDGS

(d) Io8 - MADF

Figure 5.2 – Several types of snow samples (here, PP/DF & DF) and the segmentation results using CDGS in left column, and MADF in right column.

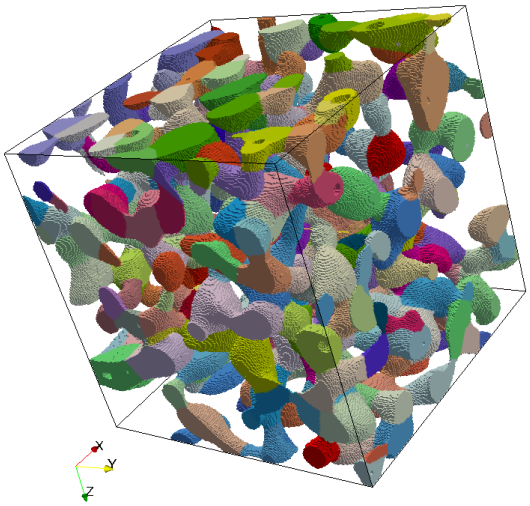

(a) I23 - CDGS

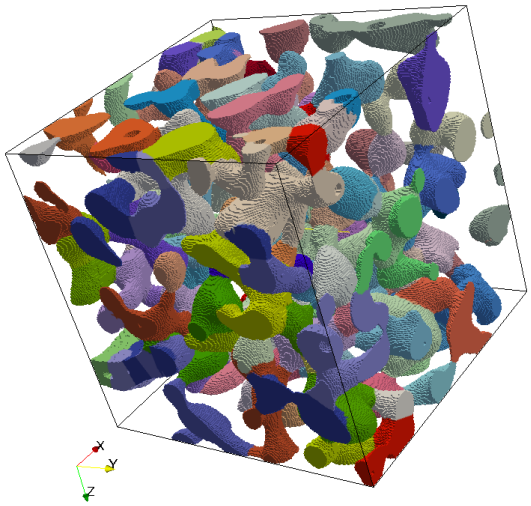

(b) I23 - MADF

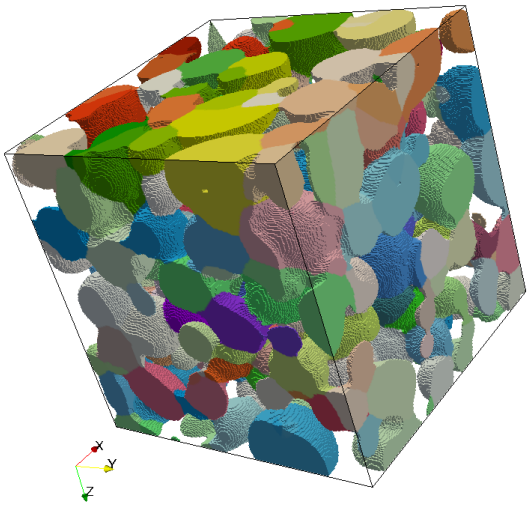

(c) Ho3 - CDGS

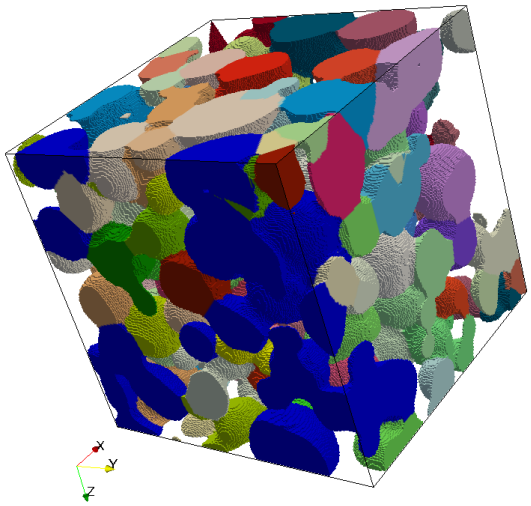

(d) Ho3 - MADF

Figure 5.3 – Several types of snow samples (here, RG & MF) and the segmentation results using CDGS in left column, and MADF in right column.

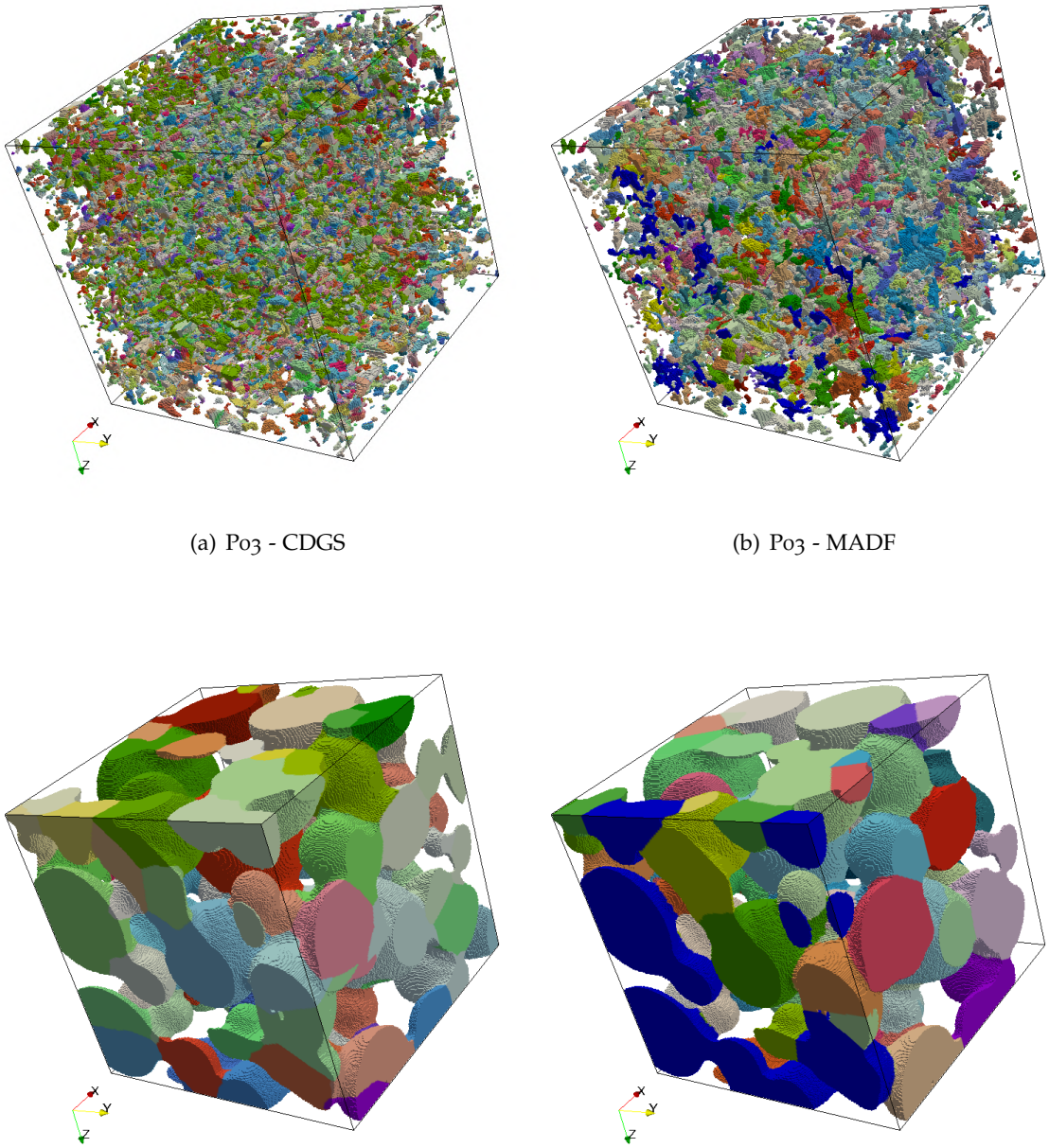

(a) Po3 - CDGS

(b) Po3 - MADF

(c) Ho5 - CDGS

(d) Ho5 - MADF

Figure 5.4 – Several types of snow (here, PP/DF & MF) and the segmentation results using CDGS in left column, and MADF in right column.

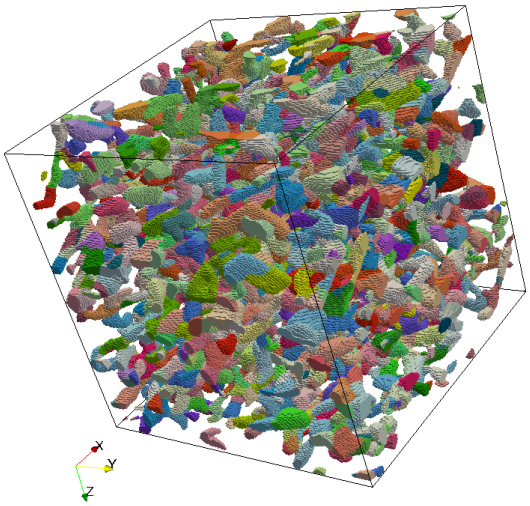

(a) P04 - CDGS

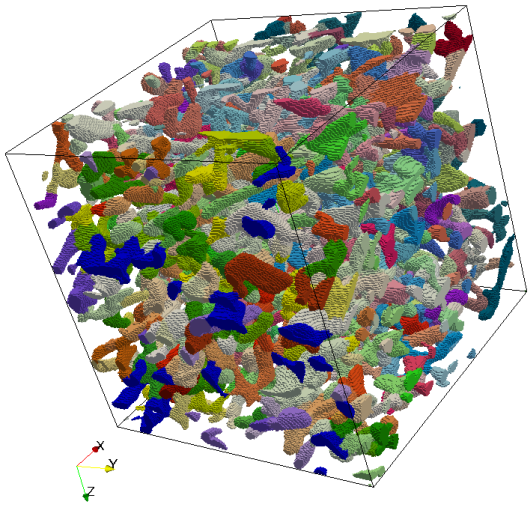

(b) P04 - MADF

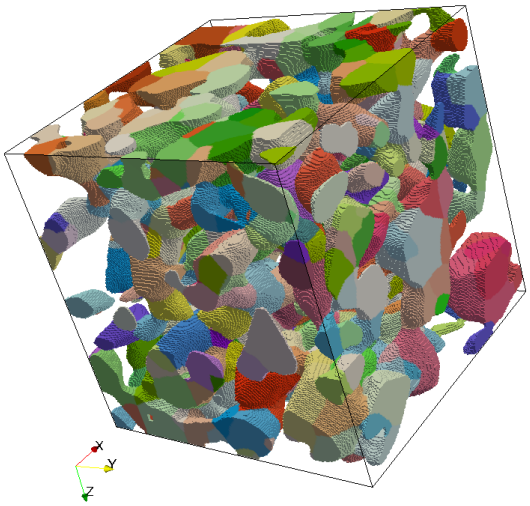

(c) P10 - CDGS

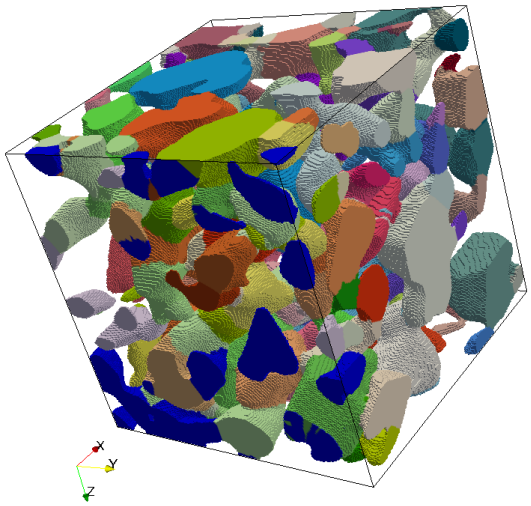

(d) P10 - MADF

Figure 5.5 – Several types of snow samples (here, PP/DF & RG) and the segmentation results using CDGS in left column, and MADF in right column.

Table 5.2 – List of main parameters in CDGS.

Parameters	Value range	Description
MIL_PROP	int, from 30 to 60	It's a percentage. It determines the radius of the spheres according to the local maximum found.
TYPE_SEUIL	0, 1, 2 or 3	Curvature map segmentation. 0 - the nth percentile of negative curvature. 1 - the nth percentile of positive curvature. 2 - the average of curvatures. 3 - based on a threshold determined by SEUIL_FIXE.
SEUIL_FIXE	int, Positive or Negative between -30 and 30	Determines the segmentation of the curvature map when TYPE_SEUL=3. An appropriate value is close to zero.
GRAIN_MIN	int, from 20 to 800 depends on the size of the image	Determines the minimum size of grains in number of voxels.

the surface of 3-D object as proposed in [FBC+05]. This voxel projection method was applied to each surface estimation (SSA, SGCA) in the following results. The time evolution of snow determine the relationship between SSA and SGCA. In Fig. 5.7, we can notice that (a) is a snow sample whose type is DF. Because of its elongated structure, the interface area between the grains is much less than the area of the snow surface. But after evolving, the structure of snow can become as sample MF in (b). With the increasing size of snow grain, the difference between SSA and SGCA is less pronounced. This is illustrated by Fig. 5.8 and 5.9.

Fig. 5.8 presents the relationship between SGCA and SSA using both CDGS and MADF. We can see that the behavior of the algorithm is slightly different for high SSA value. Both behaviors using CDGS and MADF present such dependence of SGCA with SSA on different types of snow samples. Considering the real situation, in practice, the behavior using MADF is more raisonable.

In Fig.5.9, we estimate SGCA by CDGS, MADF and another method presented in [HCL+13] (referred as Hagenmuller et al, 2013). The method of Hagenmuller et al use a geometrical algorithm based on curvature and constriction. The algorithm is parameterized with a local contiguity indicator (referred as c), which defines the

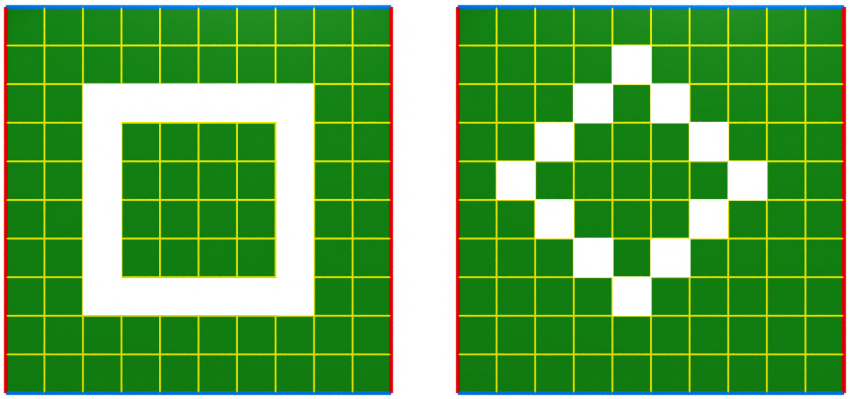

(a) (b)

Figure 5.6 – Rotation of a square in a digital space: (a) is a square of size $l = 6$ pixels, (b) is the same square after a rotation of 45°. The size obtained by voxel amounts to 4 pixels.

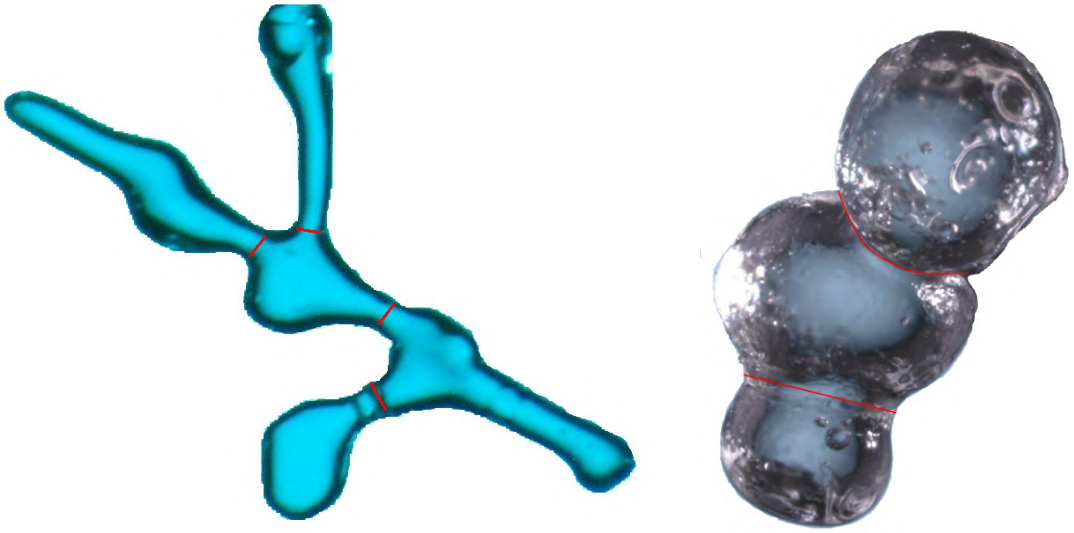

(a) (b)

Figure 5.7 – The relationship between SSA and SGCA in different types of snow samples (red lines represent the interfaces between grain pairs): (a) is a sample DF. (b) is a sample MF.

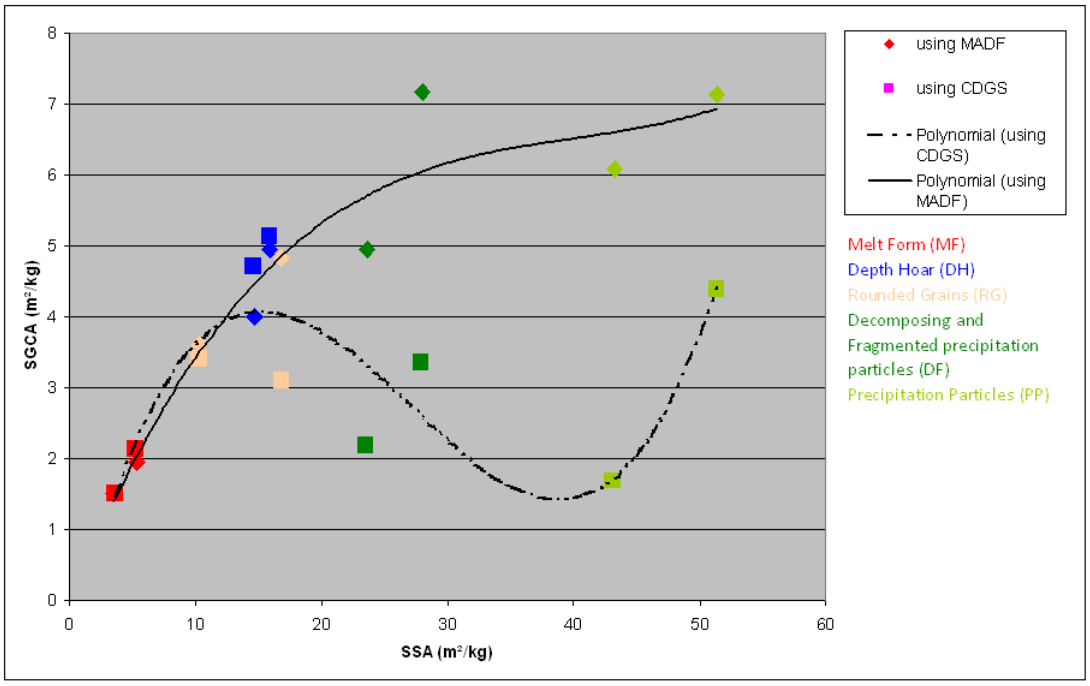

Figure 5.8 – Dependence of SGCA with SSA on several types of snow samples using MADF ♦ and CDGS ■. Black polynomial fits are plotted for a better visualization.

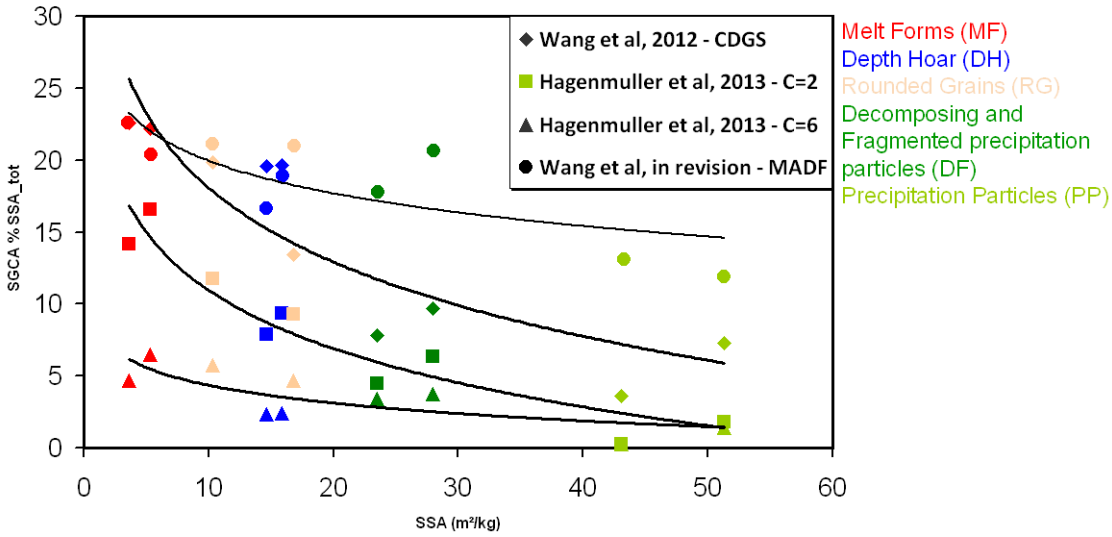

Figure 5.9 – Estimation of grain contact area on several types of snow samples using different thresholds. Black lines correspond to logarithmic fits of the SGCA results.

segmentation scale.

The representation of the microstructure with grains enables the investigation of the bonding system, which is determinant for mechanical properties. The Fig.5.9 illustrates the consistency of the different methods, i.e. it shows a similar behavior with snow type. In these algorithms, the different setting of parameters can affect the values of SGCA. This is due to the fact that the "grain concept" is difficult to define. But fixing the same parameters for all snow samples provides an objective means to quantitatively compare the sample's bonding system. It seems that SGCA could be a potential parameter to help in determining the snow type. In addition this graph shows that mechanically processing "old" snow samples could significantly increase SSA.

5.3 Conclusion

Shape segmentation methods were used to decompose the original shape into meaningful components. In our work, it consisted in decomposing the 3-D snow sample into grains. Because of the complexity of snow microstructure, some snow samples

are hard to segment. Our methods provide reasonable results for different types of snow without changing the algorithm parameters. This helps in defining objective criteria to recongnize grains. The estimations of SGCA and SSA based on the result of grain segmentation can help to model the physical and mechanical parameters of snow microstructure.

Chapter 6

Conclusion and future work

Contents

In this manuscript, we focused on the snow grains which are necessary to better understand the metamorphism and the physical or mechanical properties of snow. According to the presentation in chapter 2, various types of snow grains exist in nature (from nearly spherical to facetted ones). Although many methods can solve shape segmentation problem, they do not meet all the requirments for this application to snow. Improving the quality of segmentation was the objective of our thesis.

We present two methods for this problem:

— A curvature based method which detects the difference between convex and concave surfaces to propagate a volumetric segmentation into the whole object;

— Another approach, which uses the internal information from digital flow to decompose the objects and improves some drawbacks of the first method.

These segmentation results on the snow sample help to analyse the geometric properties of snow microstructure and give interesting outlooks to simulate snow methamophism, and the associated evolution of properties.

The methods of segmentation could be improved in a future work: we are considering the combination of the two approaches into one, which would be more precise and efficient. More physical or mechanical analysis of snow could be advanced based on grain segmentation. Beside the snow application, the algorithms could benefit to numerous other materials like ceramics, metallic alloys and so on.

6.1 Contributions

Our contributions of this work can be summarized as follows:

1. The first contribution is the proposal of a method CDGS of segmentation for presenting the snow image into grains. The segmentation comes from the curvature map on the surface. The map constructure process is efficent, because we only consider the absolute value of the mean curvature with the sign of the lowest principle curvature. A thresholded sign of lowest principle curvature map (SLPCM for short) well divided the surface into convexes and concaves. This method provide a volumetric segmentation which is an improvement of the method described in [ZPKA02].

2. The second contribution is the proposal of an algorithm which handles the noise sensitivity problem of shape segmentation. The idea comes from a global view. A geometric concept "digital flow" is applied in this suject. In [DGG03], they introduce the "flow" to solve the segmentation problem. We propose a fast computation of critical points using tools on digital domain. A simple geometric parameter is used to merge some unnecessary decomposition cases. This method is easy to implement with a digital library. In the process, only two thresholds control the quality of segmentation. It is more adaptive than CDGS.

3. The third contribution is the application to snow microstructure. The segmentation helps to describe snow microstructure. Specific grain contact area (SGCA), is a parameter that is strongly correlated with snow mechanical properties [FLD+11, VBG+75]. From a more conceptual point of view, SGCA provides scalar information on the bonding area between grains that are not available from the sole classical specific surface area (SSA). With our methods, we can compute SGCA from 3-D images to help in characterizing snow quantitatively.

6.2 Future work

For further work, we could improve some steps in methods and have more applications:

1. From the comparison results in article and chapter 5, MADF has a better segmentation than CDGS. However, the running time of CDGS is less, because only surface information is taken into account in CDGS. In the next step, we are considering an algorithm that combines the advantages of the two methods. A novel framework would be: use curvature information on surface for a preliminary segmentation, in order to separate the points on medial axis into "interesting" and "less interesting". In other words, in addition to remove the regular points from the point set on medial axis, we need a second selection considering the curvature information. If the corresponding curvatures are less interesting, the medial balls will be removed too. In such a point of view, we

would keep less critical points which would be more efficient than before.

2. Observing from the experiment results with MADF, the threshold γ in pre-processing is closely relative to the grain size. In next step, we want to find out an equation to describe this relationship in general cases. Some statistics theories can be used to analyze the range of the grain size. In this way, the threshold γ could be very finely estimated. This update can improve the self-adaptation of the method.

3. The third perspective is to apply our grain segmentation results into an analysis of the thermal conductivity of snow, in order to model the mechanical properties in temperature gradient metamorphism. The interface between two grains with its orientation could help to evaluate the heat transfer inside grains. With a littler extension of our method, the orientations of interfaces could be obtained. It will provide a new opportunity to model the different types of snow metamorphism.

Conclusion

Contributions

Dans ce manuscrit, nous nous sommes intéressés aux propriétés géométriques des grains de neige qui jouent un rôle fondamental pour une meilleure compréhension des propriétés mécaniques ou physiques ainsi que des métamorphoses de la neige. Dans ce contexte, nous avons proposé plusieurs techniques permettant d'isoler ces grains dans des images micro-tomographiques 3-D d'échantillons de neige.

Comme nous l'avons vu dans le chapitre 2, la difficulté réside dans le fait que ces grains peuvent avoir des géométries variées (quasi-sphérique, très facettisées...) et être fortement connectés entre eux. Sur ce type de données, les approches usuelles de la littérature ne produisent pas de décompositions satisfaisantes dans le sens où soit la décomposition est sur/sous-segmentée, soit les interfaces entre grains ne sont pas physiquement plausibles.

Nous avons donc cherché à améliorer ces techniques en proposant deux approches différentes. La première (CDGS) utilise des informations différentielles sur la surface (courbure) afin de localiser les convexités/concavités locales et les ponts entre grains. Dans un second temps, ces informations surfaciques sont répercutées dans le volume pour construire un partitionnement 3-D cohérent. Cette approche, publiée dans ICPR 2012, donne des résultats intéressants mais est assez sensible aux imperfections sur la surface. De nombreux paramètres ont dû être introduits pour filtrer, lisser et segmenter les informations différentielles de surface.

La seconde approche exploite uniquement des informations volumiques (axe médian, diagramme de puissance, notion de flot...) pour effectuer la décomposition (MADF). Bien que les imperfections de surface puissent induire des perturbations significatives sur l'axe médian notamment, exploiter la structure volumique dans son ensemble permet d'avoir des résultats de segmentation beaucoup plus stables. D'un point de vue théorique, nous avons proposé un mécanisme de segmentation basé sur la notion de flot dans le modèle discret. Notre formulation discrète de cet objet, proposé initialement dans le continu, nous a permis de construire des algorithmes de segmentation très efficaces et parfaitement adaptés aux structures discrètes. Cette approche fait l'objet d'une publication en cours de révision.

Au delà de ces outils de décomposition volumique, une contribution importante

porte sur l'exploitation de ces résultats de décomposition dans le cadre de l'analyse de microstructures de neige. En effet, nos algorithmes nous ont permis d'évaluer quantitativement une mesure physique très importante lorsqu'il s'agit d'analyser ce type de matériaux : la surface spécifique des contacts entre grains (specific grain contact area, SGCA), qui à l'avantage de décrire par une grandeur scalaire la taille moyenne des ponts reliant les grains. Nous avons pu notamment conclure que nos résultats de segmentation sont cohérents avec ce que l'on peut observer dans l'état de l'art.

Perspectives

Ce travail peut donner lieu à de nombreuses perspectives, que ce soit spécifiquement sur les algorithmes de segmentation, ou encore sur son application à l'analyse des microstructures de neige.

Sur le premier point, nous souhaitons développer une approche hybride pour la segmentation permettant de combiner les avantages respectifs des deux approches développées. Plus précisément, il nous semblerait intéressant d'intégrer les informations différentielles de surface extraites par CDGS dans le modèle volumique par flot de MADF. En effet, l'approche MADF nécessite deux paramètres fondamentaux. Le premier est utilisé dans le cadre d'un filtrage des boules de l'axe médian pour augmenter la robustesse au bruit, et le second dans le processus de segmentation par flot. Il pourrait donc être intéressant d'utiliser les informations différentielles de surface pour guider le filtrage de l'axe médian notamment.

Dans le cadre spécifique des microstructures de neige, une analyse statistique plus fine des dimensions caractéristiques des structures de glace constituant la neige devrait permettre de mieux ajuster les paramètres de segmentation en fonction du type de données et ainsi de rendre la méthode encore plus adaptative.

Enfin, des perspectives particulièrement intéressantes consisteraient à appliquer nos résultats de segmentation en grains individuels à des simulations physiques (par exemple, avec la prise en compte des effets de joints de grains et d'orientation cristallines dans les métamorphoses), des calculs thermiques (modèles de type Batchelor) ou mécaniques (modélisation par éléments discrets - DEM). L'interface entre deux grains ainsi que l'orientation de ces contacts pouvant être facilement extraites de nos résul-

tats, les algorithmes développés ouvrent ainsi de nouvelles perspectives pour l'étude de la microstructure de la neige, de ses métamorphoses ainsi que de ses propriétés. Ces algorithmes pourraient également s'appliquer à de nombreux autres matériaux poreux ou granulaires tels les céramiques ou les poudres métalliques.

Bibliography

[AG75] G. Abele and A.J. Gow. *Compressibility Characteristics of Undisturbed Snow*. Research report. U.S. Army Cold Regions Research and Engineering Laboratory, 1975. 17

[AGBD98] L. Arnaud, M. Gay, J.-M. Barnola, and P. Duval. Imaging of firn and bubbly ice in coaxial reflected light: a new technique for the characterization of these porous media. *Journal of Glaciology*, 44(147):326–332, 1998. 20

[APC+11] L. Arnaud, G. Picard, N. Champollion, F. Domine, J.-C. Gallet, E. Lefebvre, M. Fily, and J.-M. Barnola. Measurement of vertical profiles of snow specific surface area with a 1 cm resolution using infrared reflectance: instrument description and validation. *Journal of Glaciology*, 57(201):17–29, 2011. 21

[AR68] F. H. R. Attix and W. C. Roesch. *Radiation dosimetry*. Academic Press, New York, 1968. 24, 25

[Aur87] F Aurenhammer. Power diagrams: properties, algorithms and applications. *SIAM J. Comput.*, 16(1):78–96, February 1987. 43

[Bak03] I. Baker. Imaging dislocations in ice. *Microscopy research and technique*, 62:70–82, 2003. 22

[BBM+00] J. Baruchel, J.-Y. Buffière, E. Maire, P. Merle, and G. Peix. *X-ray tomography in material science*. Hermès Science Publications, Paris, 2000. 26

[BCKO08] Mark de Berg, Otfried Cheong, Marc van Kreveld, and Mark Overmars. *Computational Geometry: Algorithms and Applications*. Springer-Verlag TELOS, Santa Clara, CA, USA, 3rd ed. edition, 2008. 41

[BES94] R. L. Brown, M. Q. Edens, and A. Sato. Metamorphism of fine-grained snow due to surface curvature differences. *Ann. Glaciol.*, 19:69–76, 1994. 47

[BF93] S. Beucher and Meyer. F. The morphological approach to segmentation: The watershed transform. In *Mathematical Morphology in Image Processing*, pages 433–481. Marcel Dekker, Inc., 1993. 49

[BFO07] J.-B. Brzoska, F. Flin, and N. Ogawa. Using Gaussian curvature for the 3D segmentation of snow grains from microtomographic data. In W. Kuhs, editor, *Physics and Chemistry of Ice*, Special Publication Nr 311, pages 125–132, Cambridge, UK, 2007. RSC Publishing. Proceedings of the 11th International Conference on the Physics and Chemistry of Ice held at Bremerhaven, Germany on 23-28 July 2006. 45

[BFSS01] T. Baunach, C. Fierz, P. K. Satyawali, and M. Schneebeli. A model for kinetic grain growth. *Annals of Glaciology*, 32(1):1–6, 2001. 21

[BGCF95] J. W. Bullard, E. J. Garboczi, W. C. Carter, and E. R. Fuller. Numerical methods for computing interfacial mean curvature. *Computational Materials Science*, 4:103–116, 1995. 45

[BGKW95] Heinz Breu, Joseph Gil, David Kirkpatrick, and Michael Werman. Linear time euclidean distance transform algorithms. *IEEE Transactions on Pattern Analysis and Machine Intelligence*, 17:529–533, 1995. 40

[BGN12] John W. Barrett, Harald Garcke, and Robert Nuernberg. Numerical computations of facetted pattern formation in snow crystal growth. *arXiv:1202.1272v1*, 2012. 2, 6

[Bla97] D. Blanc. *Les rayonnements ionisants*. Dunod, Paris, 1997. 24

[Boi95] E. Boix. *Approximation linéaire des surfaces de R^3 et applications*. PhD thesis, École Polytechnique, 1995. 45

[Bra13] W.L. Bragg. The diffraction of short electromagnetic waves by a crystal. In *Proceedings of the Cambridge Philosophical Society*, volume 17, pages 43–57, 1913. 38

[CFG+14] Neige Calonne, Frédéric Flin, Christian Geindreau, Bernard Lesaffre, and Sabine Rolland du Roscoat. Study of a temperature gradient metamorphism of snow from 3-D images: time evolution of microstructures, physical properties and their associated anisotropy. *The Cryosphere*, 8:2255–2274, 2014. xiii, 32

[CFM+11] Neige Calonne, Frédéric Flin, Samuel Morin, Bernard Lesaffre, Sabine Rolland du Roscoat, and Christian Geindreau. Numerical and experimental investigations of the effective thermal conductivity of snow. *Geophysical Research Letters*, 38(23):L23501, 2011. xiv, 55

[CFTT03] D. Coeurjolly, F. Flin, O. Teytaud, and L. Tougne. Multigrid convergence and surface area estimation. In T. Asano, R. Klette, and C. Ronse, editors, *11th International Workshop on Theoretical Foundations of Computer Vision: Geometry, Morphology, and Computational Imaging*, volume 2616 of *Lecture Notes in Computer Science*, pages 101–119. Springer-Verlag, 2003. 48

[CM99] O Cuisenaire and B Macq. Fast euclidean distance transformation by propagation using multiple neighborhoods. *Computer Vision and Image Understanding*, 76(2):163 – 172, 1999. 40

[CM07] David Coeurjolly and Annick Montanvert. Optimal Separable Algorithms to Compute the Reverse Euclidean Distance Transformation and Discrete Medial Axis in Arbitrary Dimension. *IEEE Transactions on Pattern Analysis and Machine Intelligence*, 29(3):437–448, March 2007. 43

[CMC07] David Coeurjolly, Annick Montanvert, and Jean-Marc Chassery. Géométrie discrète et images numériques, September 2007. Ouvrage collectif, Traité IC2, Hermès, pp-416. 39

[Coe02] D. Coeurjolly. *Algorithmique et géométrie discrète pour la caractérisation des courbes et des surfaces*. PhD thesis, Université Lumière, Lyon 2, 2002. xiv, 46

[Dan80] Per-Erik Danielsson. Euclidean Distance Mapping. *Computer Graphics And image Processing*, 14:227–248, 1980. 40

[DGG03] T.K. Dey, J. Giesen, and S. Goswami. Shape segmentation and matching with flow discretization. *Lecture Notes in Computer Science*, 2748:2536, 2003. 95

[Dig] 31

[Duk00] P. J. Duke. *Synchrotron radiation - production and properties*. Oxford Science Publications. Oxford University Press, New York, 2000. 28

[EB91] M. Q. Edens and R. L. Brown. Changes in microstructure of snow under large deformations. *J. Glaciol.*, 37(126):193–202, 1991. 47

[EB95] M. Edens and R.L. Brown. Measurement of microstructure of snow from surface section. *Defence Science Journal*, 45(2):107–116, 1995. 21

[Eva55] R. D. Evans. *The atomic nucleus*. McGraw-Hill, New York, 1955. xiii, 25

[FAD+09] C. Fierz, R. L. Armstrong, Y. Durand, P. Etchevers, E. Greene, D. M. McClung, K. Nishimura, P. K. Satyawali, and S. A. Sokratov. *The international classification for seasonal snow on the ground*. IHP-VII Technical Documents in Hydrology n 83, IACS Contribution n 1, 2009. xvii, 21, 54, 80, 81

[FB08] F. Flin and J.-B. Brzoska. The temperature gradient metamorphism of snow: vapour diffusion model and application to tomographic images. *Ann. Glaciol.*, 49:17–21, 2008. 80

[FBC+05] F. Flin, J.-B. Brzoska, D. Coeurjolly, R. A. Pieritz, B. Lesaffre, C. Coléou, P. Lamboley, O. Teytaud, G. L. Vignoles, and J.-F. Delesse. Adaptive estimation of normals and surface area for discrete 3-D objects: application to snow binary data from X-ray tomography. *IEEE Trans. Image Process.*, 14(5):585–596, May 2005. 87

[FBL+01] F. Flin, J.-B. Brzoska, B. Lesaffre, C. Coléou, and P. Lamboley. Computation of normal vectors of discrete 3D objects: application to natural snow images from X-ray tomography. *Image Anal. Stereol.*, 20:187–191, Nov 2001. 45, 48

[FBL+03] F. Flin, J.-B. Brzoska, B. Lesaffre, C. Coléou, and R. A. Pieritz. Full three-dimensional modelling of curvature-dependent snow metamorphism: first results and comparison with experimental tomographic data. *J. Phys. D. Appl. Phys.*, 36(10A):A49–A54, May 2003. (10.1088/0022-3727/36/10A/310). xiii, 8

[FBL+04] F. Flin, J.-B. Brzoska, B. Lesaffre, C. Coléou, and R. A. Pieritz. Three-dimensional geometric measurements of snow microstructural evolution under isothermal conditions. *Ann. Glaciol.*, 38:39–44, 2004. 21, 80

[FLD+11] F. Flin, B. Lesaffre, A. Dufour, L. Gillibert, A. Hasan, S. Rolland du Roscoat, S. Cabanes, and P. Pugliese. On the Computations of Specific Surface Area and Specific Grain Contact Area from Snow 3D Images. In Y. Furukawa, editor, *P. C. I.*, pages 321–328, Sapporo, JP, 2011. Hokkaido University Press. Proceedings of the 12th International

Conference on the Physics and Chemistry of Ice held at Sapporo, Japan on 5-10 September 2010. 81, 95

[Fli04] F. Flin. *Snow metamorphism description from 3D images obtained by X-ray microtomography*. PhD thesis, Université Grenoble 1, 2004. partially in French. xiii, 26

[FM05] Céline Fouard and Grégoire Malandain. 3-d chamfer distances and norms in anisotropic grids. *Image and Vision Computing*, 23(2):143–158, February 2005. 40

[Fri13] G. Friedel. Sur les symétries cristallines que peut révéler la diffraction des rayons X, 1913. 38

[GDZP09] J.-C. Gallet, F. Domine, C. S. Zender, and G. Picard. Measurement of the specific surface area of snow using infrared reflectance in an integrating sphere at 1310 and 1550 nm. *The Cryosphere*, 3:167 – 182, 2009. 21

[GM98] Weiguang Guan and Songde Ma. A list-processing approach to compute voronoi diagrams and the euclidean distance transform. *IEEE Trans. Pattern Anal. Mach. Intell.*, 20(7):757–761, 1998. 40

[Goo87] W. Good. Thin sections, serial cuts and 3-D analysis of snow. In *International Association of Hydrological Sciences Publication*, volume 162, pages 35–48, 1987. (Symposium at Davos 1986 – *Avalanche Formation, Movement and Effects*). 47

[HCL+13] P. Hagenmuller, G. Chambon, B. Lesaffre, F. Flin, and M Naaim. Energy-based binary segmentation of snow microtomographic images. *International Glaciological Society*, 59:859–873, 2013. 87

[JG73] S. Jonesa and N. Gilra. X-ray topographical study of dislocations in pure and hf-doped ice. *Philosophical Magazine*, 27:457–472, 1973. 22

[Klu11] R. T. Kluender. *Mésures de distortions en trois dimensions par imagerie en diffraction Bragg : application aux cristaux de glace*. Phd thesis, University of Grenoble, 2011. 38

[KP09] Thomas U. Kaempfer and Mathis Plapp. Phase-field modeling of dry snow metamorphism. *Phys. Rev. E*, 79(3):031502, Mar 2009. 2, 6

[KR04] Reinhard Klette and Azriel Rosenfeld. *Digital geometry - geometric methods for digital picture analysis*. Morgan Kaufmann, 2004. 39

[Kry75] P. Kry. The relationship between the visco-elastic and structural properties of fine-grained snow. *Journal of Glaciology*, 14(72):479–500, 1975. 21

[KS01] A. C. Kak and M. Slaney. *Principles of computerized tomographic imaging*. Society of Industrial and Applied Mathematics, Philadelphia, 2001. http://www.slaney.org/pct/pct-toc.html. 26, 27

[LA02] Gina L. Luciano and Mary R. Albert. Bidirectional permeability measurements of polar firn. *Ann. Glaciol.*, 35(1):63–66, 2002. 80

[LBC+03] B. Lesaffre, J.-B. Brzoska, C. Coléou, F. Flin, and R. Pieritz. Images tridimensionnelles de neige : des prélèvements in situ aux fichiers de données volumiques. Technical Report 22, Centre d'Etudes de la Neige, Centre National de Recherches Météorologiques, Météo-France, october 2003. 34

[LBD95] F. Liu, I. Baker, and M. Dudley. Thermally induced dislocation loops in polycrystalline ice. *Philosophical Magazine A*, 71:1–14, 1995. 22

[Len99] A. Lenoir. *Des outils pour les surfaces discrètes : estimation d'inuarisants géométriques, préservation de la topologie, tracé de géidésiques et visualisation*. PhD thesis, Université de Caen, 1999. 45

[LPM98] B. Lesaffre, E. Pougatch, and E. Martin. Objective determination of snow-grain characteristics from images. *Ann. Glaciol.*, 26:112–118, 1998. 21, 47

[LRK+09] W. Ludwig, P. Reischig, A. King, M. Herbig, E. M. Lauridsen, G. Johnson, T. J. Marrow, and J. Y. Buffière. Three-dimensional grain mapping by x-ray diffraction contrast tomography and the use of friedel pairs in diffraction data analysis. *Review of Scientific Instruments*, 80(3):033905, 2009. 20, 37

[MQR03] Calvin R. Maurer, Jr., Rensheng Qi, and Vijay Raghavan. A linear time algorithm for computing exact euclidean distance transforms of binary images in arbitrary dimensions. *IEEE Trans. Pattern Anal. Mach. Intell.*, 25(2):265–270, February 2003. 40

[MRU74] M. Mellor, Cold Regions Research, and Engineering Laboratory (U.S.). *A Review of Basic Snow Mechanics*. U.S. Army Cold Regions Research and Engineering Laboratory, 1974. 17, 18

[Nel01] J. Nelson. Growth mechanism to explain the primary and secondary habits of snow crystals. *Philosophical magazine. A. Physics of condensed matter. Structure, defects and mechanical properties*, 81(10):2337–2373, 2001. 20

[OM00] J. Ohser and F. Mücklich. *Statistical analysis of microstructures in materials science*. Statistics in practice. John Wiley, 2000. 15

[PGM96] F. Peyrin, L. Garnero, and I. Magnin. Reconstruction tomographique d'images 2D et 3D. *Traitement du signal*, 13(4):379–440, 1996. 22

[RBRS+12] F. Riche, T. Bartels-Rausch, S. Schreiber, M. Ammann, and M. Schneebeli. temporal evolution of surface and grain boundary area in artificial ice beads and implications for snow chemistry. *Journal of Glaciology*, 58(210):815–817, 2012. 20

[RKP+11] S. Rolland du Roscoat, A. King, A. Philip, P. Reischig, W. Ludwig, F. Flin, and J. Meyssonnier. Analysis of snow microstructure by means of X-ray diffraction contrast tomography. *Adv. Eng. Mater.*, 13(3):128–135, 2011. xiii, 20, 37

[RP68] Azriel Rosenfeld and John L. Pfaltz. Distance functions on digital pictures. *Pattern Recognition*, 1(1):33–61, 1968. 40

[RT79] C. Raymond and K. Tusima. Grain coarsening of water-saturated snow. *J. Glaciol.*, 22(86):83–105, 1979. 80

[RXs] 29

[Sin78] N. K. Sinha. Observation of basal dislocations in ice by etching and replicating. *Journal of Glaciology*, 21:385–395, 1978. 22

[SRUotCoE97] L.H. Shapiro, Cold Regions Research, Engineering Laboratory (U.S.), and United States. Army. Office of the Chief of Engineers. *Snow Mechanics: Review of the State of Knowledge and Applications*. CRREL report. U.S. Army Cold Regions Research and Engineering Laboratory, 1997. 17

[VBG+75] K. F. Voitkovsky, A. N. Bozhinsky, V. N. Golubev, M. N. Laptev, Zhigulsky A. A., and Yu. Ye. Slesarenko. 114:171–179, 1975. International symposium on snow mechanics. 81, 95

[War82] S.G. Warren. Optical properties of snow. *Rev. Geophys.*, 20(1):67–89, 1982. 21

[WGFC12] Xi Wang, Luc Gillibert, F. Flin, and David Coeurjolly. Curvature-Driven Volumetric Segmentation of Binary Shapes: an Application to Snow Microstructure Analysis. In *International Conference on Pattern Recognition*. IEEE Computer Society, November 2012. 45

[WRHS03] C.J.L. Wilson, D.S. Russell-Head, and H.M. Sim. The application of an automated fabric analyzer system to the textural evolution of folded ice layers in shear zones. *Annals of Glaciology*, 37(1):7–17, 2003. 20

[ZPKA02] Y. Zhang, J. Paik, A. Koschan, and M.A. Abidi. A simple and efficient algorithm for part decomposition of 3-D triangulated models based on curvature analysis. In K. M. Morton and M. J. Baines, editors, *Proc. Int. Conf. Im. Processing, vol III*, pages 273–276, 2002. Rochester, NY, September 2002. 94

Publications and Communications

Peer-reviewed international journals

— **Wang X.**, Coeurjolly D., Flin F.: Digital Flow for Shape Decomposition: Application to 3-D Microtomographic Images of Snow. In *Pattern Recogniton Letters* , 2013 (in revision).

Peer-reviewed international conference proceedings

— **Wang X.**, Gillibert L., Flin F., Coeurjolly D.: Curvature-Driven Volumetric Segmentation of Binary Shape: an Application to Snow Microstructure Analysis. In *International Conference on Pattern Recognition (ICPR)*, pp. 742-745, 2012.

Non peer-reveiwed international conference proceedings

— Hagenmuller P., Guillaume C., Flin F., **Wang X.**, Lesaffre B., Naaim M.: Description of the snow microstructure as a 3D assembly of snow grains. In *International Snow Science Workshop*, 2013.

Communications

— **Wang X.**: Grain Segmentation with Medial Axis based Voronoi Flow. In *Journée du Groupe de Travail de Géométrie Discrète*, 2012. Oral presentation.

— **Wang X.**, Gillibert L., Flin F., Coeurjolly D.: Curvature-Driven Volumetric Segmentation of Binary Shape: an Application to Snow Microstructure Analysis. In *International Conference on Pattern Recognition (ICPR)*, 2012. Poster.

— **Wang X.**, Flin F., Coeurjolly D., Lesaffre B.: Digital Flow for Grain Segmentation from 3D Microtomographic Images of Snow. In *International Snow Science Workshop*, 2013. Poster.

— Flin F., Calonne N., Lesaffre, B., **Wang X.**, Carmagnola C., Rolland du Roscoat S., Charrier P., Morin S., Coeurjolly D., Geindreau C.: 3D imaging of snow microstructure for a better knowledge of snow properties and of their time evolution : 2 examples. In *IGS Symposium on Seasonal Snow and Ice*, 2012. Oral presentation.

— Hagenmuller P., **Wang X.**, Flin F., Chambon G., Naaim M.: Segmentation of snow grains from microtomographic data to derive the specific grain contact area as a mechanical indicator. In *Davos Atmosphere and Cryosphere Assembly* , 2013. Oral presentation.

— Flin F., **Wang X.**, Hagenmuller P., Calonne N., Lesaffre B., Dufour A., Coeurjolly D., Guillaume C., Christian G., Rolland du Roscoat S.: Computation of grain sizes from microtomographic images of snow. In *International Snow Science Workshop*, 2013. Oral presentation.

— Hagenmuller P., Guillaume C., Flin F., **Wang X.**, Lesaffre B., Naaim M.: Description of the snow microstructure as a 3D assembly of snow grains. In *International Snow Science Workshop*, 2013. Poster.

Résumé

Les avalanches de neige sont des phénomènes naturels complexes dont l'occurrence s'explique principalement par la structure et les propriétés du manteau neigeux. Afin de mieux comprendre les évolutions de ces propriétés au cours du temps, il est important de pouvoir caractériser la microstructure de la neige, notamment en termes de grains et de ponts de glace les reliant. Dans ce contexte, l'objectif de cette thèse est la décomposition d'échantillons de neige en grains individuels à partir d'images 3-D de neige obtenues par microtomographie X. Nous présentons ici deux méthodes de décomposition utilisant des algorithmes de géométrie discrète. Sur la base des résultats de ces segmentations, certains paramètres, comme la surface spécifique et la surface spécifique de contact entre grains sont ensuite estimés sur des échantillons de neiges variées. Ces méthodes de segmentation ouvrent de nouvelles perspectives pour la caractérisation de la microstructure de la neige, de ses propriétés, ainsi que de leur évolution au cours du temps.

Mots-clefs: Neige, Métamorphose, Microstructure, Décomposition de formes, Géométrie discrète

Abstract

Snow avalanches are complex natural phenomena whose occurrence is mainly due to the structure and properties of the snowpack. To better understand the evolution of these properties over time, it is important to characterize the microstructure of snow, especially in terms of grains and ice necks that connect them. In this context, the objective of this thesis is the decomposition of snow samples into individual grains from 3-D images of snow obtained by X-ray microtomography. We present two decomposition methods using algorithms of discrete geometry. Based on the results of these segmentations, some parameters such as the specific surface area and the specific contact area between grains are then estimated from samples of several snow types. These segmentation methods offer new outlooks for the characterization of the microstructure of snow, its properties, and its time evolution.

Keywords: Snow, Metamorphism, Microstructure, Shape decomposition, Digital geometry